

Numerical Analysis of Soil Behavior and Stone Columns Effects on the Railway Track

Dissertation

Zur Erlangung des akademischen Grades
Doktor-Ingenieur

an der Fakultät Bauingenieurwesen
der
Bauhaus-Universität Weimar

vorgelegt von
M.Sc. Mojtaba Shahraki
aus dem Iran

Mentor:
Prof. Dr.-Ing. Karl Josef Witt

Numerical Analysis of Soil Behavior and Stone Columns Effects on the Railway Track

Dissertation
Zur Erlangung des akademischen Grades
Doktor-Ingenieur

an der Fakultät Bauingenieurwesen
der
Bauhaus-Universität Weimar

vorgelegt von
M.Sc. Mojtaba Shahraki
aus dem Iran

Gutachter:

1. Univ. Prof. Dr.-Ing. K. J. Witt
2. Univ. Prof. Dr.-Ing. habil. T. Wichtmann
3. Univ. Prof. Dr.-Ing. F. Rackwitz

Tag der Disputation: 13. February 2019

Acknowledgment

I would like to thank all institutions and people who made this thesis possible, namely:

Prof. K. J. Witt for supervising this thesis and for all the suggestions made to improve my work. I would also like to acknowledge his continuous support and care.

The Bauhaus Research School (BRS) for the financial support given through the individual doctoral grant.

Special thanks go to my parents, who relinquished a more comfortable life to support our studies – and many other things.

Ehrenwörtliche Erklärung

Ich erkläre hiermit ehrenwörtlich, dass ich die vorliegende Arbeit ohne unzulässige Hilfe Dritter und ohne Benutzung anderer als der angegebenen Hilfsmittel angefertigt habe. Die aus anderen Quellen direkt oder indirekt übernommenen Daten und Konzepte sind unter Angabe der Quellen gekennzeichnet.

Weitere Personen waren an der inhaltlich-materiellen Erstellung der vorliegenden Arbeit nicht beteiligt. Insbesondere habe ich hierfür nicht die entgeltliche Hilfe von Vermittlungs- bzw. Beratungsdiensten (Promotionsberater oder andere Personen) in Anspruch genommen.

Niemand hat von mir unmittelbar oder mittelbar geldwerte Leistungen für Arbeiten erhalten, die im Zusammenhang mit dem Inhalt der vorgelegten Arbeit stehen.

Die Arbeit wurde bisher weder im In- noch im Ausland in gleicher oder ähnlicher Form einer anderen Prüfungsbehörde vorgelegt.

Ich versichere ehrenwörtlich, dass ich nach bestem Wissen die reine Wahrheit gesagt und nichts verschwiegen habe.

Mojtaba Shahraki

Abstract

Railway systems are highly competitive compared with other means of transportation because of their distinct advantages in speed, convenience and safety. Therefore, the demand for railway transportation is increasing around the world. Constructing railway tracks and related engineering structures in areas with loose or soft cohesive subgrade usually leads to problems, such as excessive settlement, deformation and instability. Several remedies have been proposed to avoid or reduce such problems, including the replacement of soft soil and the construction of piles or stone columns.

This thesis aims to expand the geotechnical knowledge of how to improve subgrade ballasted railway tracks, using stone columns and numerical modeling for the railway infrastructure. Three aspects are considered: i) railway track dynamics modeling and validation by field measurements, ii) modeling and parametric studies on stone columns, and iii) studies on the linear and non-linear behavior of stone columns under the dynamic load of trains.

The first step of this research was to develop a reliable numerical model of a railway track. The finite element method in a time domain was used for either a 2D plane strain or 3D analysis. Individual methods for modeling a train load in 2D and 3D were implemented and are discussed in this thesis. The developed loading method was validated with three different railway tracks using obtained vibration measurements. Later, these numerical models were used to analyze the influence of stone column length and train speed in the stress field.

The performance of the treated ground depends on various parameters, such as the strength of stone columns, spacing, length and diameter of the columns. Therefore, the second step was devoted to a parameter study of stone columns as a unit cell with an axisymmetric condition. The results showed that even short stone columns were effective for settlement reduction, and area of replacement was the main influential parameter in their performance.

The third part of this thesis focuses on a hypothetical railway-track response to the passage of various train speeds and the influence of stone-column length. The stress-strain response of subgrade is analyzed under either an elastic–perfectly plastic or advanced constitutive model. The non-linear soil response in the finite element method and the impact of train speed and stone column length on railway tracks are also evaluated. Moreover, the reductions of induced vibration – in both a horizontal and a vertical direction – after improvement are investigated.

Kurzfassung

Problemstellung und Zielsetzung der Arbeit

Bahnsysteme sind aufgrund ihrer Vorteile in Bezug auf Geschwindigkeit, Komfort, Sicherheit und Klimaschutz im Vergleich zu anderen Transportmitteln der Infrastruktur äußerst zukunftsorientiert. Der Neu- und Ausbau des Schienenverkehrs steigt daher weltweit.

Der Bau von Bahntrassen auf gering tragfähigem Baugrund stößt auf Probleme der Tragfähigkeit und Gebrauchstauglichkeit wie z.B. unverträglich große Verformungen oder gar Instabilitäten. Abhilfe schafft eine Baugrundverbesserung durch Austausch des Bodens oder eine partielle Verbesserung mit säulenartigen Tragelementen aus Beton, Sand oder Schotter. Eine geeignete und häufig angewendete Maßnahme zur Verbesserung von weichem Baugrund sind sogenannte Schottersäulen, die rasterartig in erforderlicher Länge in den Baugrund eingerüttelt werden.

Ziel dieser Arbeit ist es, die Effekte zyklischer und dynamischer Verkehrslasten auf unterschiedlich lange Schottersäulen unter Neu- oder Ausbaustrecken bei verschiedenen Zuggeschwindigkeiten zu analysieren. Drei Aspekte sollen hierbei berücksichtigt werden:

- Eine Modellierung der Gleisdynamik und Validierung durch Feldmessungen
- Eine Modellierung und parametrische Untersuchungen an Schottersäulen
- Eine Untersuchungen zum linearen und nichtlinearen Verhalten von Schottersäulen unter dynamischen Zuglasten.

Stand der Wissenschaft

Das mechanische Verhalten von Schienen und Oberbau unter verschiedenen Szenarien von Zuglasten wurde bereits intensiv erforscht. Vier Methoden wurden dabei teils kombiniert angewendet: empirische Modelle, Feldmessungen, analytische und numerische Modelle.

Der Baugrund von Bahnsystemen erfährt statische, zyklische und dynamische Einwirkungen. Aufgabe der geotechnischen Planung und Bemessung ist es, die Verformungen im Baugrund unter den applizierten Belastungen auf ein verträgliches Maß zu beschränken. Hierzu wurden sowohl Technologien, als auch Prognosemodelle entwickelt, die es zu erklären und verfeinern gilt.

Finite-Elemente (FE) -Modelle des Tragsystems bieten den Vorteil, dass die Interaktion der Gleisgeometrie mit einem angemessen feinen Baugrundmodell dargestellt werden kann. Eine Gleisanlage kann dabei eben (2D) oder aber räumlich (3D) modelliert werden. Für ein 2D-Modell muss angenommen werden, dass sich das transversale Spurprofil entlang der Längsachse nicht verändert, wohingegen 3D-FE-Modelle nahezu alle geometrischen Bedingungen und Beschränkungen berücksichtigen können. Das 3D-Modell ist jedoch komplexer und erfordert wesentlich längere Rechenzeiten. Ein Ziel dieser Arbeit war, die Grenzen der 2D und 3D FE-Modellierung für ein konkretes

Schienensystem und einen mit Schottersäulen verbesserten geringtragfähigen Baugrund bei dynamischer Einwirkung zu ergründen.

Eingesetzte Methoden

Ein selbst entwickeltes 3D FE-Modell umfasst Schiene, Kontaktstelle, Schwelle und alle dazugehörigen Elemente eines Oberbaus. Hierzu musste eine absorbierende Grenzbedingung verwendet werden, um beliebige andere Grenzbedingungen in allen Modellen zu simulieren. Alle Simulationen wurden im Zeitbereich unter direkter Integration mit impliziten Schemata analysiert.

Im 2D-Modell wurde die Schiene als ein System aus verschiedenen Schichten mit elastischen Eigenschaften betrachtet. Es enthielt ein Modul »Gleisdynamik« zur Bestimmung der stationären Erregung und ein Modul »Baugrund« zur Simulation der Belastung der tieferen Bodenschichten. Der Oberbau wurde als modifizierter elastischer Balken betrachtet, die Substruktur und der Boden wurden basierend auf der Kegeltheorie als Feder und Dämpfer modelliert.

Die numerische Modellierung der Schottersäulen war zweigeteilt. Für den Konsolidierungsprozess und zur Ermittlung der Belastung wurden die Säulen als Elementarzelle unter axialsymmetrischen Bedingungen betrachtet. Dieser Ansatz impliziert ein gleichmäßiges, konstantes Säulenraster. Die Belastung der Elementarzelle ist repräsentativ für alle Einzelsäulen im Raster.

Zur Analyse des Verhaltens des mit Säulen verbesserten Baugrunds und der Säulen selbst wurden diese bei der ebenen Betrachtung als quer zum Gleis angeordnete Streifen (Wände) modelliert. Dabei wurden im geringtragfähigen Baugrund schwimmende (kurze) Säulen und stehende (lange) Säulen betrachtet, die in tragfähigen Baugrund einbinden.

Wesentliche Ergebnisse

Die mit dem 2D FE-Modell bei vertretbaren Rechenzeiten ermittelten Ergebnisse zeigen eine gute Übereinstimmung mit den Felddaten und der 3D-FE Analyse. Die Grenze dieser vereinfachten Modellierung wird bei einer kritischen Geschwindigkeit der Zugüberfahrt erreicht, der Rayleigh Geschwindigkeit. Bis dahin kann die 2D-Analyse in allen Aussagen als Alternative zum 3D Modell mit hinreichender Genauigkeit verwendet werden.

Die Ergebnisse der numerischen Simulation werden bezüglich der einzelnen Schottersäulen als Tragelement wie folgt zusammengefasst:

- Schottersäulen reduzieren in weichem Baugrund grundsätzlich die Gesamtsetzungen der Geländeoberfläche und den Porenwasserüberdruck. Die Effektivität nimmt mit der Einbindetiefe zu.
- Das Flächenverhältnis (Säulenfläche /Gesamtfläche) hat vor allem einen starken Einfluss auf die Gesamtsetzung. Dies gilt sowohl für die stehenden als auch für die schwimmenden Säulen.
- Mit zunehmender Belastung entwickelten sich im Boden und in den Säulen plastische Verformungen, die unabhängig von der Länge der Säulen zu einer höheren Setzungsrate führen.

- Der Reibungswinkel der Schottersäule hat einen vernachlässigbaren Effekt bei schwimmenden und einen geringen bei stehenden Säulen. Das Steifigkeitsverhältnis Boden/Säule beeinflusst die Setzungen kaum.
- Änderungen des Säulenrasters hatten bei konstantem Flächenverhältnis nur einen untergeordneten Einfluss auf die Setzungen. Dies gilt sowohl für schwimmende als auch für stehende Säulen.

Bezüglich des Gesamtsystems Trasse, Schiene, Oberbau und Baugrund werden die Ergebnisse der numerischen Simulation wie folgt zusammengefasst:

- Obwohl eine Zunahme des Erddruckbeiwerts immer in Verbindung mit einem Anstieg der lateralen Spannungen im Boden steht, war dieser Effekt bei der Modellierung der Säulen vernachlässigbar.
- Eine Anordnung des Rasters der Steinsäulen in Bezug auf die Gleisachse hatte keine Auswirkung auf die vertikale Verformung. Jedoch zeigten die Variationen der Anordnung einen Einfluss auf die horizontale Verschiebung.
- Sowohl die horizontalen, als auch die vertikalen Verschiebungen des Systems werden stark von den geometrischen Kenngrößen der Säulen beeinflusst. Selbst kurze Säulen haben jedoch bereits eine hohe Effektivität hinsichtlich der Setzungsreduktion.
- Die Schottersäulen bewirken keine Verringerung der vertikalen Schwingungsamplitude bei hohen Frequenzen. Sie mindern jedoch die Spitzenamplitude ab, die sich aus der Überfahrt von Fahrgestellen zweier benachbarter Wagen ergeben.
- Eine Geschwindigkeitszunahme der Überfahrt beeinflusst die Scherspannung stärker als die Vertikalspannung. Dies führt bei einer Zugüberfahrt zu einer zyklischen Drehung der Hauptspannungen unter dem Gleis.
- Die vergleichende Berechnung der mechanischen Größen mit dem Mohr-Coulomb- und dem Hardening Soil-Stoffgesetz für kleine Belastungen belegen, dass das einfache idealelastische-idealplastische Stoffgesetz für Boden und Säule ein angemessenes Modell zur Ermittlung der Verteilung von Spannungen und Dehnungen im Baugrund ist. Diese Feststellung gilt für eine Tiefe von mehr als 2 m unter der Schiene. In der Nähe der Schiene und im Oberbau konnten mit beiden Stoffmodellen die Dehnung und vor allem die Schubspannung nicht befriedigend genau ermittelt werden.

Kurze, schwimmende Schottersäulen haben im weichen, geringtragfähigen Boden wegen der schwachen lateralen Stützung nur eine geringe Stabilität. Dennoch haben sie einen starken setzungsmindernden Effekt.

Das Versagen von Schottersäulen, ein Scherbruch oder Ausbeulen, wird von der axialen Belastung in Relation zur Steifigkeit des umgebenden Bodens bestimmt. Die Geschwindigkeit einer Zugüberfahrt hat dagegen nur einen unerwartet geringen Einfluss.

Table of Contents

1	Introduction	1
2	State of the Art	3
2.1	Railway track systems	3
2.2	Railway track superstructure	3
2.2.1	Rails.....	3
2.2.2	Pads	4
2.2.3	Sleepers	4
2.3	Railway track substructure	5
2.3.1	Ballast.....	5
2.3.2	Sub-ballast	5
2.3.3	Subgrade	6
2.4	Railway track loading.....	6
2.4.1	Loading types	6
2.4.2	Static loading.....	6
2.4.3	Cyclic loading.....	7
2.4.4	Dynamic loading	8
2.5	Analytical calculation of the railway track.....	10
2.5.1	Beam on elastic foundation (BOEF)	10
2.6	Numerical railway track modeling	12
2.6.1	General	12
2.6.2	Finite-element (FE) method	12
2.6.3	Boundary-element (BE) method.....	13
2.6.4	Scaled boundary finite element (SBFE) models.....	14
2.6.5	Hybrid models	14
2.7	Linear and non-linear modeling of railway tracks.....	14
2.8	Ground improvement methods	15
2.9	Soil improvement under railway tracks.....	17
2.10	Stone column analysis	18
2.10.1	Analysis of embankment founded on stone columns	18
2.10.2	Circular sliding surface method.....	19
2.10.3	Average strength parameter method.....	20

2.10.4 Profile method	21
2.10.5 Comparison of analysis methods	22
3 Field Measurements	24
3.1 Introduction	24
3.2 The first test site: Belgium	24
3.2.1 Track and soil characteristics	24
3.2.2 Trains.....	26
3.2.3 Measurements.....	27
3.3 The second test site: Germany.....	28
3.3.1 Track and soil characteristics	28
3.3.2 Railjet train.....	29
3.3.3 Measurements.....	30
4 Railway Track Numerical Simulation	32
4.1 Introduction	32
4.2 Three-dimensional modeling.....	32
4.2.1 FEM specification	32
4.2.2 Material properties.....	34
4.2.3 Loading procedure.....	35
4.2.4 Results	36
4.3 Two-dimensional modeling.....	39
4.3.1 Background	39
4.3.2 Superstructure.....	40
4.3.3 Substructure.....	43
4.3.4 Sample calculation for the second site	46
4.3.5 Results	48
5 Stone Column Numerical Simulation.....	51
5.1 Introduction	51
5.2 Unit cell approach	51
5.2.1 General study.....	51
5.2.2 Parametric study	54
5.3 Plane strain modeling	59
5.3.1 Geometry and material properties	59
5.3.2 Effect of lateral earth pressure.....	60

5.4	Arrangement of stone columns beneath a railway track.....	61
6	Stone Columns under Railway Tracks	65
6.1	Introduction	65
6.2	Numerical simulation	66
6.2.1	Properties of the track and train.....	66
6.2.2	Verification of developed 2D model	68
6.3	Effect of stone columns	69
6.3.1	Horizontal and vertical displacement	69
6.3.2	Reduction of induced vibrations.....	71
6.3.3	Change in pore water pressure	73
6.4	Elastic response of the railway track	75
6.5	Effects of train speed and stone-column length on track response.....	82
6.6	Non-linear response of the railway track.....	86
6.7	Application of geosynthetics	92
6.8	Failure mechanism of stone columns	93
7	Summary and Conclusions	95
8	Further Research Topics.....	98

List of Figures

Figure 2.1 Rail cross-section and properties (UIC60).....	4
Figure 2.2 (a) Monoblock and (b) twin-block concrete sleepers.....	5
Figure 2.3 Definition of axle distance ‘a’ and bogie distance ‘X’ was constant.	8
Figure 2.4 Comparison of response to moving load for two trains with different bogie distance	8
Figure 2.5 Beam on elastic foundation.....	11
Figure 2.6 Example of a 2D (left) and 3D (right) symmetrical FE model of a railway track (Shahraki et al., 2014a, Shahraki et al., 2014b).	13
Figure 2.7 Schematic view of construction of stone columns (Raju et al., 2004).....	16
Figure 2.8 Ideal stress distribution pattern. Left, stone column; right, deep foundation (pile).	17
Figure 2.9 Orientation of stone columns: (a) square pattern (b) triangular pattern and (c) hexagonal pattern.....	19
Figure 2.10 Circular Sliding Surface Method (after Filz and Navin, 2006).....	20
Figure 2.11 Conversion of the discrete cylindrical stone columns (left) to equivalent strips(right) (Castro, 2017).....	21
Figure 2.12 Stone column equivalent strip for triangular pattern (after Filz and Navin, 2006).....	22
Figure 3.1 Geometry of track in the first site (m).....	25
Figure 3.2 TGV train (Connolly, 2013).....	26
Figure 3.3 Thalys train (Connolly, 2013).....	26
Figure 3.4 Location of the geophones (9, 11, and 15 m from nearest track) at the site.	27
Figure 3.5 Recorded signals from the passage of two trains (TGV and Thalys) at different speeds (280 km/h and 300 km/h) at different distances from the nearest track (9, 11, 15, and 19 m). Data provided by Connolly (2013).	28
Figure 3.6 Superstructure geometry of the second site (m).....	29
Figure 3.7 Railjet train (m).....	30
Figure 3.8 Soil stratifications and location of geophones (m).....	30
Figure 3.9 Results of the second site, re-plotted (after Wegener, 2012)	31
Figure 4.1 Cross-sectional detail of the actual rail and the rail modified to rectangular (mm), after Witt (2008)	33
Figure 4.2. Mesh of the 3D model (Midas GTS NX).....	33
Figure 4.3 Modeling of the moving load (Araújo, 2011, Jiang et al., 2014).....	36
Figure 4.4 Results of 3D FE simulations for the first site under passage of TGV train at 280 km/h compare to field measurements, at various distances (9, 11, 15, and 19 m) from the nearest track.	37
Figure 4.5 Results of 3D FE simulations for the first site under passage of Thalys train at 299 km/h compare to the field measurements, at various distances (9, 11, 15, and 19 m) from the nearest track.....	37
Figure 4.6 Vertical velocity from 3D FE model compared with field data from the second site (depths of 0, 0.3, 2, and 4 m beneath the sleeper).....	38
Figure 4.7 Displacement of 3D FE model compared with field data from the second site (depths of 0, 0.3, 2, and 4 m beneath the sleeper).	39
Figure 4.8 Simplified effective length of sleeper	41

Figure 4.9 Conversion of discrete supports to continuous support	41
Figure 4.10 Cone model (after Adam and Kopf, 2003).....	44
Figure 4.11 Pressure under sleeper on ballast	48
Figure 4.12 Numerical results of 2D FEM for 1 st site under passage of TGV train at 280 km/h, at various distances (9, 11, 15, and 19 m) from the nearest track.	49
Figure 4.13 Numerical results of 2D FEM for 1st site under passage of Thalys train at 299 km/h, at various distances (9, 11, 15, and 19 m) from the nearest track.	49
Figure 4.14 Vertical velocity obtained from 2D FE model in four checkpoints at the second site, at various depths (0, 0.3, 2, and 4 m) beneath the sleepers.	50
Figure 5.1 Axisymmetric unit cell model (after Tan et al., 2008).....	52
Figure 5.2 Effect of stone column length on excess pore water pressure and settlement	53
Figure 5.3 Change in excess pore water pressure after 1 and 3 weeks for different lengths of stone columns at a depth of 5 m, in an x-direction (from the outer boundary of the columns to outer boundary of the soil).....	53
Figure 5.4 Effect of the area ratio ($a_s = 11, 15, 20, 25$, and 30%) on settlement and consolidation time in case of different stone columns length ($L = 3, 5, 7$, and 10 m) compared to no-improved soil model.	54
Figure 5.5 Effect of the friction angle ($\varphi_c = 30, 35, 40, 45$, and 50 degrees) on different stone column lengths ($L = 3, 5, 7$, and 10 m).	55
Figure 5.6 Effect of the applied load (50, 100, 150, 200, and 250 kPa) on settlement and consolidation time in case of different stone column lengths ($L = 3, 5, 7$, and 10 m).....	56
Figure 5.7 Effect of the modulus ratio ($m = 5, 10, 15$, and 20) on different stone column lengths ($L = 3, 5, 7$, and 10 m).....	57
Figure 5.8 Effect of column spacing ($S = 1, 1.5, 2, 2.5$, and 3 m) on settlement for different stone columns lengths ($L = 3, 5, 7$, and 10 m) while the area of replacement is constant ($a_s = 20\%$).	58
Figure 5.9 Schematic view of the plane strain numerical analysis model (Stone column length $L = 10$ m).	59
Figure 5.10 Stress-settlement behavior of stone columns with different lengths ($L = 3, 5, 7$, and 10 m) when increasing lateral earth pressure and keeping the area of replacement constant ($a_s = 20\%$).....	61
Figure 5.11 Half-symmetric model of the railway track	62
Figure 5.12 Arrangement of stone columns with regard to the track axis. Left, columns with offset from the axis (Arrangement 1); right, center of columns are aligned to the axis (Arrangement 2).	63
Figure 5.13 Vertical displacement at middle of subgrade for two types of arrangements, columns with and without offset from the axis (Arr.1 and Arr.2) as a function of the spacing of the stone columns (1.0, 1.5, 2.0, and 2.5 m) for different column lengths (3, 5, 7, 10 m)	63
Figure 5.14 Horizontal displacement at middle of subgrade for two arrangements: columns with (Arr. 1) and without (Arr. 2) offset from the axis as a function of the spacing of the stone columns (1, 1.5, 2, and 2.5 m) for different column lengths (3, 5, 7, 10 m).	64
Figure 6.1 Seismic wave distribution (after Connolly et al., 2013).....	65
Figure 6.2 Active (f_A) and natural (f_N) frequencies in relation to wheel distance and depth of soil layer, respectively (after Katzenbach and Ittershagen, 2004).	66
Figure 6.3 Geometry of the hypothetical railway track, with different stone column lengths (3, 5, 7 and 10 m) and a center-to-center distance of 2 m. The locations of the stress and deformation checkpoints are shown.....	67

Figure 6.4 Vertical velocity in 2D model and 3D model with no stone columns determined in points D and E (train speed 130 km/h).....	68
Figure 6.5 Vertical velocity in 2D model and 3D model with stone columns with a depth of 3 m (train speed 130 km/h).	68
Figure 6.6 Horizontal displacement along a stone column (column length/depth was 2–12 m).....	70
Figure 6.7 Vertical displacement of the cross-section in the middle height of the subgrade.	71
Figure 6.8 Vertical vibration amplitude in the middle of soft soil (point E). The graphs show the effect of stone column length (0, 3, 5, 7, and 10 m) under the passage of trains at various speeds (50, 80, 100, 130, 180, 220, 250, and 270 km/h).	72
Figure 6.9 Horizontal vibration amplitude at 12 m from the center of loaded track (point G). The graphs show the effect of stone column length (0, 3, 5, 7, and 10 m) under the passage of trains at various speeds (50, 80, 100, 130, 180, 220, 250, and 270 km/h).	73
Figure 6.10 Effective pore water pressure in middle of the soft soil layer for various train speeds (50, 80, 100, 130, 180, 220, 250, and 270 km/h) and stone column lengths (0, 3, 5, 7, and 10 m).....	74
Figure 6.11 Spatial distribution of principal stress under axle loads. Left, cross-section of an embankment. Right, in plane parallel to embankment (after Hendry et al., 2013)	75
Figure 6.12 Stress tensor and sign convention for stresses (Plaxis bv, 2014).	75
Figure 6.13 Vertical velocity at deformation points C, D, E and F (at depths of 0.7, 2.3, 5.3, and 10 meters respectively). Train speed: 50 km/h; on a track with no improvement.....	76
Figure 6.14 Vertical stress at the stress points for L, M and N (at depths of 1.4, 6, and 10 m). Train passage at 50 km/h on a track with no improvement.	77
Figure 6.15 Horizontal stress at the stress points for L, M, and N (at depths of 1.4, 6, and 10 m). Train passage at 50 km/h on a track with no improvement.	78
Figure 6.16 Cartesian shear stress at the stress points in depth of 1.4, 6.0, and 10 m for L, M, and N, due to the train passage with speed of 50 km/h on a track with no improvement.....	78
Figure 6.17 Principal stress directions: clockwise rotation is positive and counter-clockwise rotation is negative (Plaxis bv, 2014).	79
Figure 6.18 Principal stress rotational angle at the points L, M, and N (at depths of 1.4, 6, and 10 m). Train passage at 50 km/h on a track with no improvement.....	80
Figure 6.19 Time response of mean stress (p) at the points L, M, and N (at depths of 1.4, 6, and 10 m). Train passage at 50 km/h on a track with no improvement.....	81
Figure 6.20 Time response of deviatoric stress (q) at the points L, M, and N (at depths of 1.4, 6, and 10 m). Train passage at 50 km/h on a track with no improvement.	81
Figure 6.21 Deviatoric and volumetric strain at the points L, M, and N (at depths of 1.4, 6, and 10 m). Train passage at 50 km/h on a track with no improvement.....	82
Figure 6.22 Normalized vertical and horizontal stresses (σ_{yy} and σ_{xx}) of the track as a function of train speed, for various lengths of stone columns in the middle of soft soil layer (point M)	83
Figure 6.23 Normalized mean and deviatoric stress of the track under increasing train speed, for various lengths of stone columns in the middle of the soft soil layer (point M).....	84
Figure 6.24 Change in stress path for different train speeds (50, 80, 100, 130, 180, 220, 250, and 270 km/h), after implementing stone columns of various lengths (0, 3, 5, 7, and 10 m).	85
Figure 6.25 Deviatoric and volumetric responses for stone columns of differing lengths (0, 3, 5, 7, and 10 m).	86

Figure 6.26 Changes in lateral strain along the stone column beneath the loading area, for three train speeds (50, 130, and 250 km/h).....	87
Figure 6.27 Changes in vertical strain along the stone column beneath the loading area, for three train speeds (50, 130, and 250 km/h).....	88
Figure 6.28 Effect of the length of stone columns (0, 3, 5, 7, and 10 m) on the stress path, for three train speeds (50, 130, and 250 km/h).....	89
Figure 6.29 Effect of length of stone columns (0, 3, 5, 7, and 10 m) on volumetric strain, corresponding to mean stress for three train speeds (50, 130, and 250 km/h).	90
Figure 6.30 Effect of the length of stone columns (0, 3, 5, 7, and 10 m) on deviatoric response, for three train speeds (50, 130, and 250 km/h).	91
Figure 6.31 Effect of the length of stone columns (0, 3, 5, 7, and 10 m) on shear response, for three train speeds (50, 130, and 250 km/h).....	92
Figure 6.32 Effect of basal reinforcement on horizontal displacement along the stone column at depth.	93
Figure 6.33 Failure mechanism of different lengths of stone columns (3, 5, 7 and 10 m), under passage of a train travelling at 250 km/h. The ellipse shows column failure through bulging or shear plane (extended to the outer columns), where the other stone columns failed due to lateral spreading, or became bent. Scale: 1/50.	94

List of Tables

Table 2.1 Heavy axle load trains around the world (Mundrey, 2009).....	6
Table 2.2 Axle load of high-speed trains around the world	7
Table 2.3 The velocity factor (γ). Source: Skoglund (2002)	9
Table 3.1 Properties of the first site (Connolly, 2013)	25
Table 3.2 TGV specifications (Connolly, 2013)	26
Table 3.3 Thalys specification (Connolly, 2013)	26
Table 3.4 Material properties of the second site.....	29
Table 4.1 Contact pressure distribution patterns (after Sadeghi and Barati, 2010).....	40
Table 4.2 Effective length (area) of sleeper support at rail seat (Sadeghi and Barati, 2010)	41
Table 4.3 Available input data based on the data from second site.....	46
Table 4.4 Basic calculations for Cone	47
Table 4.5 Obtained results for the substructure calculations.....	47
Table 4.6 Dynamic magnification factors	47
Table 5.1 Material properties for unit cell models	51
Table 5.2 Model dimensions for equal areas of replacement but different spacing between columns .	58
Table 5.3 Material properties for the plane strain calculation	60
Table 5.4 Material properties of model used to study stone column patterns beneath a railway track .	62
Table 6.1 Material properties of the hypothetical geometry to study the effect of the length of the stone columns	67

Notations

Latin Alphabet

A_e	Effective area of sleeper
a_s	Area replacement ratio
a	Sleepers distance
b_L	Ideal strip width
b_s	Sleeper width
C_n	Courant number
c	Cohesion
D	Damping ratio
D	Wheel diameter
d	Diameter of the stone column
d_e	Diameter of the influence area
e	Void ratio
e_{max}	Maximum void ratio
e_{min}	Minimum void ratio
E	Young's Modulus
E_{sec}	Secant Young's Modulus
E_{ref}	Young's Modulus under the reference pressure
f	Frequency
f_A	Active frequency
f_N	Natural frequency
G	Shear modulus
HS-small	Hardening Soil small-strain
I	Inertia of the beam
l_a	Effective length of sleeper
l_s	Sleeper length
k	Track global stiffness
K_0	Earth pressure coefficient
k_s	Stiffness of foundation
L	Characteristic length
m	Modulus ratio
m	Mass per unit length
MC	Mohr-Coulomb model
n	Settlement improvement factor
n_s	Stress concentration ratio
p	Total mean stress
p'	Effective mean stress
P_s	Static wheel load

P_d	Dynamic wheel load
q	Deviatoric stress
R	Radius of the unit cell
t	Time
v_s	Shear wave velocity
s	Spacing of columns
$V_{(train)}$	Trains speed
V_{cr}	Critical velocity
$V_{Rayleigh}$	Rayleigh wave speed
x	Longitudinal distance from the wheel load

Greek Alphabet and other symbols

α	Mass proportional damping coefficients
β	Stiffness proportional damping coefficients
α	Dynamic effect of the adjacent axle loads
β	Damping factor
γ	Soil unit weight
ν	Poisson's ratio
ϕ	Friction angle
$\sigma_{xx/yy}$	Horizontal and vertical shear stress
σ_{xy}	Shear stress
α_{xy}	Principal axis rotation angle
ε_d	Deviatoric strains
ε_v	Volumetric strain
α	Impact load factor
ξ	Damping ratio

Abbreviations

AREMA	American Railway Engineering and Maintenance-of-Way Association
BE	Boundary-Element
BEM	Boundary-Element Method
BOEF	Beam On Elastic Foundation
CSL	Critical state line
DEM	Discrete-Element Method
EBA	Eisenbahn-Bundesamt, The German Federal Railway Authority
FE	Finite-Element
FEM	Finite-Element Method
HS	Hardening soil
HS-small	Hardening soil small strain
HST	High-Speed Train
RMS	Root Mean Square
SBFEM	Scaled Boundary Finite Element Method
TGV	Train à Grande Vitesse, French high-speed train
UIC	Union Internationale des Chemins de Fer, International Union of Railways

1 Introduction

Railway transportation is one of the oldest types of transport and has been used for many decades to transfer freight and passengers to long-distance destinations. Through continuous improvement, it has become a highly popular transportation service. Particularly in Europe and East Asia, railway tracks are considered an effective solution for long-distance transportation due to their economic advantage and environment-friendly aspects.

Ballasted tracks are the most common type of railway tracks around the world and are designed to provide a stable, safe, and efficient support for rail and train. A ballasted track consists of a superstructure (sleepers, fasteners, and rails) and a substructure (ballast, sub-ballast, and subgrade layers). The main function of the track system is to distribute the wheel loads evenly to the next element, to decrease stresses transmitted to the deeper layers and prevent excessive deformation or failure in weak soil layers. Constructing a railway track, especially a high-speed railway track, demands a better quality of ground, due to more restrictive criteria related to deformation. However, locations having soft ground are inevitable when tracks are laid, and are associated with large displacements. This leads to a higher risk of derailment, discomfort for passengers, and increased induced vibrations in trains and gradual destruction of the neighboring structures. Ground improvement methods, such as stone columns, are a reliable approach to overcome the problem. Currently, many techniques are used to construct stone columns through natural soil, and each method has its own advantages and disadvantages. Using any of them in appropriate soil conditions will result in similar products. The stiffness and unit weight of the granular material used for construction is different from the usually weak non-improved natural soil. Soil in improved sites is expected to reduce the displacement amplitude and softening due to pore water pressure accumulation and to increase the accelerations at the surface, and it shows the importance of investigation on the impact of induced vibration by passing train on surrounding area.

Prediction of railway-track behavior under train loads in different scenarios has been the focus of many studies. Four solutions have been proposed: field measurements, empirical models, analytical models and numerical models. Field measurement is the basis for developing other methods and is necessarily for calibration of analytical and numerical models. From the dawn of the railway track, empirical models have played an important role in design and planning the tracks. However, due to limited understanding of the mechanical processes of a railway track response, miscalculations should be expected. Analytical calculations simplify the theoretical models to render them suitable for modeling a railway track component. In recent decades numerical modeling has grown exponentially and it provides a valuable tool to study and predict the behavior of complex problems. Among others it gives detailed information related to changes in stresses between the vehicle and the substructure.

This thesis contributes to the advancement of methods by developing a simple and fast numerical method to study a railway track built on poor subgrade improved by stone columns with different depths. To achieve this aim, several research topics were studied using the finite element method (FEM) with verification by field measurements. Topics studied included: railway-track loading, ballasted track

responses to the passage of trains, effects of stone columns in geotechnical problems (particularly under a railway track), and characterization of the stress field induced by passage of a train on a railway track supported by stone columns.

The thesis is organized into six chapters; chapter 2 is devoted to state-of-the-art components of a typical ballasted railway track, railway track loading, and different analytical and numerical modeling methods. This discussion is followed by a brief introduction to ground improvement approaches and stone column analyses.

Chapter 3 focuses on available field measurements for two railway tracks in Europe. The sites, soil characteristics, train types, speeds and their specifications are described. Information from this chapter is used for validation of numerical simulation in later chapters.

Chapter 4 presents the numerical models developed in this thesis, and their validation based on the mentioned railway tracks using the 2D and 3D FEM. This chapter provides further insight on the 3D simulation of a moving train and presents a simplified analytical model to convert a 3D phenomenon to the 2D plane strain condition.

In Chapter 5, numerical simulation of a stone column as a unit cell, as well as plane strain for two scenarios – either plastic or consolidation calculation – are described. The effects of the length of stone columns are studied and comprehensive parametric studies on the most influential parameters in the behavior of stone columns are summarized. The applicability of various stone column arrangements beneath the existing railway track is investigated

Chapter 6 explores the elastic response of non-improved railway tracks constructed on soft soil. This is followed by a thorough examination of track responses on improved ground, using different stone column lengths, for various train speeds from low velocity to high-speed trains. The model employed is the elastic-perfectly plastic constitutive model. Due to the non-linear behavior of soil, an advanced constitutive model (Hardening Soil small-strain) is used to precisely capture the behavior of the ground under passage of trains with various speeds after improvement with stone columns.

Finally, Chapter 7 discusses the main conclusions and contributions of the study, and provides suggestions for future research topics.

2 State of the Art

2.1 Railway track systems

Railway systems are one of the most advanced and growing transportation systems; they are still being developed. The 21st century has begun, and the idea of designing a new form of high-speed railway tracks to provide safe and comfortable travel for passengers is popular. High-speed trains compete with air travel (Heelis et al., 1999). In addition, trains emit low pollution for their speed, compared with road vehicles (Krylov et al., 2000).

A railway track brings all elements – such as the rail, rail pads, sleepers, ballast and sub-ballast – together to resist the combined effects of various types of loading and climate. It also provides subgrade protection and low operational costs as well as safety and comfort for passengers (Burrow et al., 2004, McElvaney et al., 2002). In the early era of railway-track systems, they were built with limited experience and engineering knowledge. Trains have become faster and heavier, and there is a need to minimize costs. Therefore, it is important to understand railway track behavior and its influence on the subgrade. A successful design of a modern railway track involves a multidisciplinary study using geotechnical knowledge and economic principles. Application of geotechnics ensures that induced stresses, strains and deflections in the system are limited to the acceptable design range (Burrow et al., 2004).

All the elements of a railway track should be individually studied based on their functional ability and required properties to achieve the best design. Elements are usually grouped as superstructure (rail, pads, fastening system and sleeper) and substructure (ballast, sub-ballast, and subgrade). A high-speed railway track is a multi-layered structure that should provide gradual increases in stiffness from bottom to top. The stiffness of each layer depends on material properties, thickness, and compaction degree as well as the stiffness of the underlying layer. The negative effect of a soft foundation cannot be compensated for by a higher compaction of the next layer. All layers of a railway track system should work together to provide an overall stiffness that allows proper load distribution to the sleepers and minimizes the rail displacement. Ballast, sub-ballast and capping layers should be uniformly compacted, and random checking of the compaction degree is necessary to avoid local over-compaction and to plan maintenance work. Even these practices are insufficient for modern high-speed tracks, and roller integrated continuous compaction control should be performed (Brandl, 2004).

2.2 Railway track superstructure

2.2.1 Rails

The rail is one of the most important and the most expensive part of the track; it is a steel beam and provides a continuous path for the wheels of the trains. The modern rail profile has developed from

wood to steel, derived by a simple I-shaped profile with a flat bottom and a curved head for better contact between rail and wheel, to provide a smooth running surface. Rail needs to have high inertia for transferring the load to adjacent sleepers without undesirable deformation. The International Union of Railways introduced the most common rail section (UIC60), which has a mass of 60 kg per meter and a standard length of 25 m, as shown in Figure 2.1 (Dahlberg, 2003, Miura et al., 1998).

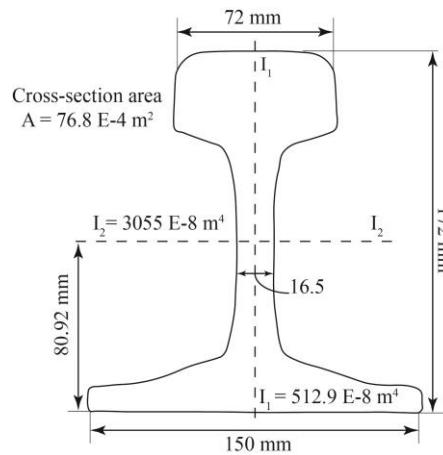


Figure 2.1 Rail cross-section and properties (UIC60)

2.2.2 Pads

To filter vibrations, protect sleepers from wear through load impact, and allow acceptable rail deformation, rubber elements are placed between the concrete sleepers and rails (Dahlberg, 2003). The pads should remain in place and should not easily degrade through normal use. The stiffness of the pad is lower than that of the rail and the sleeper and allows the rail to deform; as a result, loads can be distributed over several sleepers to reduce the local stress on the sleepers and ballast. The use of soft elastic pads provides the greatest attenuation of impact loads. Utilizing rubber pads with concrete sleepers has many benefits for the whole track system, such as damping wheel-induced vibrations, reducing the friction between rail and sleeper, and isolating electrical signals (Selig and Waters, 1994).

2.2.3 Sleepers

Sleepers can be divided into four types based on their materials: wood, steel, concrete, or synthetic. The synthetic type has the longest lifespan, but concrete sleepers are the heaviest and provide greater track stability and a better fastening system than wooden and steel sleepers. However, wooden sleepers perform the best in reduction of noise and vibration, whereas steel sleepers provide better lateral stiffness for the track. Owing to a low initial cost and maintenance cost as well as other advantages, concrete sleepers are the most widely used type for construction of a railway track. These sleepers can be monoblock or twin-block type (Figure 2.2). In general, sleepers should preserve the correct level and alignment of the rail, distribute the load in the ballast layer, and prevent lateral, longitudinal and vertical movement of the track (Dahlberg, 2003).

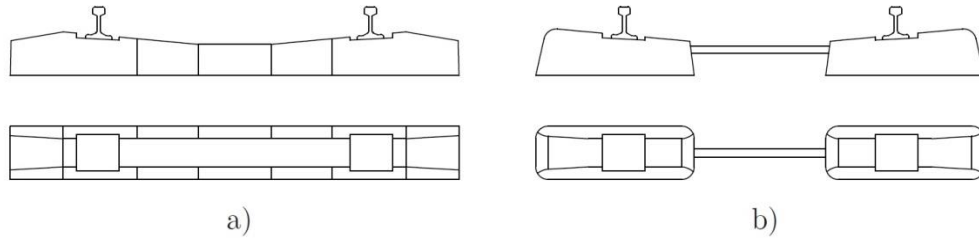


Figure 2.2 (a) Monoblock and (b) twin-block concrete sleepers

2.3 Railway track substructure

2.3.1 Ballast

Ballast is the layer of granular material, evenly graded with an angular shape that plays an important role in the quality of the track and provides a reliable support for sleepers. Ballast should uniformly transfer the load from the sleeper to underlying layers, and it is the first soil layer to absorb shocks from the dynamics. The irregular shaped ballast results in interlocking particles, which leads to high support of the superstructure against lateral, vertical and longitudinal movements (Selig and Waters, 1994, Dahlberg, 2003). Ballast also assists drainage for the track by easily draining any moisture introduced into the system away from the rails and sleepers. In general, crushed rocks are the best material for ballast. It is recommended to create small changes in angularity or surface roughness to achieve a better effect on the stress-strain behavior of ballast materials, because the sharp corners of ballast lead to undesirable stress concentrations and heterogeneous stress distributions (Lu and McDowell, 2007).

Selig and Boucher (1990) explained that typical laboratory tests for examining the quality of ballast, such as the Los Angeles abrasion test, can only be used to estimate the ballast quality. The behavior of the ballast under the passage of a train, particularly a high-speed train, cannot be investigated with the same laboratory tests.

2.3.2 Sub-ballast

Sub-ballast is a layer of granular material between the ballast and underlying subgrade to prevent mixing of the large and small particles. It is composed of broadly graded slag or crushed aggregate (Kaewunruen and Remennikov, 2008, Dahlberg, 2004). According to Selig and Waters (1994), some areas require improvements that can be fixed by stabilization with lime, cement, asphalt concrete layers, or geosynthetics.

Sub-ballast reduces stress at the bottom of the ballast layer to a reasonable level for the top of the subgrade, and prevents the upward migration of fine particles from subgrade to the ballast. Moreover, it keeps water away from the subgrade and protects it from freezing and thawing problems. However, the freeze-thaw cycles have a negative effect on the bearing capacity and stiffness of sub-ballast (Kaewunruen and Remennikov, 2008, Dahlberg, 2004).

2.3.3 Subgrade

The subgrade is the last support of the railway track before natural ground. According to Selig and Waters (1994), subgrade affects ballast and sub-ballast deterioration as well as the rail's differential settlement. Subgrade therefore has a crucial influence in rail deflection and the track response. Subgrade provides drainage and smooth settlement to ensure track serviceability, along with an increase in bearing capacity. Recently, certain synthetic materials (e.g., geotextile) have been applied to improve the subgrade performance (Kaewunruen and Remennikov, 2008). It is essential to improve subgrade properties if the track is constructed on soft soil (Heelis et al., 1999).

2.4 Railway track loading

2.4.1 Loading types

A railway track experiences three types of loading at almost the same time, namely static, cyclic, and dynamic loading. Essentially, train load should be transferred to the track system and it induces stresses and strains in the track. Understanding of generated loads in the system and their transmission from train to rail and other track elements is necessary for the design of reliable railway tracks. There are vast differences between freight and high-speed trains in term of load characteristics. Moreover, how the train load is distributed from top to bottom has a great effect on the stiffness and damping properties of underlying soil materials (Li et al., 2002).

2.4.2 Static loading

A track foundation should withstand the static loads, which are live load (train weight) and the dead load (weight of the track and subgrade). Axle load, wheel spacing, and the length of the train are the main factors when designing a railway track foundation. Heavy axle-load freight trains induce great stresses on the track, and such data become crucial. Table 2.1 and

Table 2.2 provide examples of axle load in heavy-axle freight trains and high-speed passenger trains in different countries (Mundrey, 2009).

Table 2.1 Heavy axle load trains around the world (Mundrey, 2009)

Country	Axle load (tons)	Number of cars
USA and Canada	33	130 - 140
Australia	35 - 40	200 - 240
South Africa	26 - 30	200 - 216
Sweden	30	68
China	25 - 27	210

Table 2.2 Axle load of high-speed trains around the world

Country	Vehicle type	Axle load (tons)
Germany	InterCity-Express (ICE)	19.0
France	TGV-R	17.0
England	Eurostar	17.3
China	Passenger high-speed car	17.0
Japan	100 series	16.1
USA	Acela passenger car	16.4

Stress level at depth is different for live and dead loads. The live load (train load) causes the maximum stress at top, where the wheel and rail are in contact; an increase in depth leads to a reduction of live-load stress and an increase of dead-load stress. In other words, at shallow depth the stress induced by the train load is much greater than the stress that results from the weight of the track's upper layers. However, by going deeper this stress distribution changes and the effect of the dead load becomes dominant.

In case of the train load, a stiffer track superstructure (rail and sleeper) leads to lower stress in the ballast and subgrade. Similarly, increased stiffness of the ballast and sub-ballast decreases the stress transferred to the subgrade and foundation. In general, ballast and sub-ballast are shallow, and stress due to their weight is insignificant compared with the stress induced by the train load. However, if their thickness exceeds 1.5 m then their dead load becomes important in design. It is recommended to prevent such a condition (Mundrey, 2009, Li et al., 2002).

2.4.3 Cyclic loading

The passage of a train creates a series of rapid loading pulses that induces different responses in a track compared with the stationary static loads. The properties of the soil are affected by changes in the loading rate and number of pulses. Repeated load intensity, duration, and numbers have an extended effect on the ballast, sub-ballast, and underlying soil layers. Deformation analysis of the track components, including the breakage of ballast particles, as well as maintenance planning, require the analyst to determine the number of load applications equivalent to the traffic.

In determining the number of cycles the number of axle loads and the depth are considered. For example, for a ballast layer, two axles under the same bogie (an undercarriage with four wheels pivoted beneath the end of a railway car) are considered to produce one load cycle. For the subgrade, it is assumed to be four axles under two adjacent bogies. Hence, the number of loading cycles for 10^6 tons of traffic can be determined as follows (Li et al., 2002):

$$N_a = \frac{10^6}{2P_s} \quad (2.1)$$

$$N_b = \frac{N_a}{2} \quad (2.2)$$

$$N_s = \frac{N_a}{4} \quad (2.3)$$

Here, P_s refers to static wheel-load (ton) and N_a is the number of axle-load per 10^6 tons of traffic-load, while N_b and N_s represent the corresponding numbers of axle load applications on the ballast and subgrade, respectively. Adjustment of the loads, including wheel-load distances (a in Figure 2.3) and the spacing of bogies (X in Figure 2.3), affects the interaction of adjacent loads and the whole track response. Figure 2.4 shows load distribution results at locations of interest for two different spaces between bogies ($X=2.5$ or 4.5 m in Figure 2.3). The static axle loads were 17 tons for both trains.

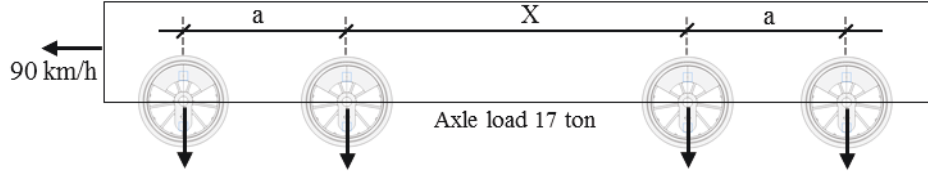


Figure 2.3 Definition of axle distance 'a' and bogie distance 'X' was constant.

Figure 2.4 shows that bogies with long distances lead to nearly complete unloading between the adjacent bogies, whereas for short distances between bogies the unloading is small. It can be concluded that for distant bogie configuration, a load cycle should be considered as consisting of two axles (i.e. one bogie generates one cycle), whereas for a short bogie distance configuration, four axles should be viewed as one load cycle (i.e. two bogies generate one cycle).

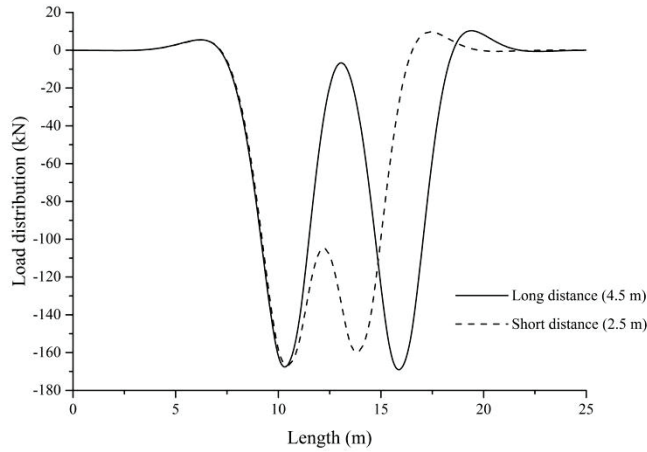


Figure 2.4 Comparison of response to moving load for two trains with different bogie distance

2.4.4 Dynamic loading

AREMA and PRC impact factor

The magnitude of a load applied on the track during the passage of a train differs from the static wheel load. This dynamic wheel load can be higher or lower than the static wheel load. Commonly, design

dynamic wheel load (P_d) is calculated by the multiplication of static wheel load (P_s) by the impact load factor (α):

$$P_d = \alpha \cdot P_s \quad (2.4)$$

For example, Chinese standards for designing high-speed railways (PRC) limit the impact load factor to 3 for tracks with speeds over 300 km/h. By contrast, the American Railway Engineering and Maintenance-of-way Association (AREMA) recommends the following equation for calculating dynamic load factors (Arema, 2013):

$$\alpha = \left(1 + \frac{0.0052 V}{D}\right) \quad (2.5)$$

where V is the train speed (km/h), and D is the wheel diameter (in meters). This approach has some limitations; mainly that it is reliable only for trains with a low speed, and the need to consider the wheel diameter in addition to the train velocity.

German and Austrian approach

This method is based on extensive measurements at tracks and is therefore an empirical method, and it is commonly used by The German Federal Railway Authority (Eisenbahn-Bundesamt, EBA) (Adam et al., 2010). The basic formula for assessing the design axle load is presented in Equation 2.6.

$$P_d = P_s \cdot k_{\text{quasi}} \cdot (1 + t \cdot s) \quad (2.6)$$

Here, P_d and P_s are design and static axle load, respectively. The k_{quasi} term refers to additional load due to cant deficiency, with a typical value of 1.1 or 1.2. The number of standard deviations (t) is assumed to be 3 for the rail, 2 for sleepers, and 1 for the substructure (Skoglund, 2002). Finally, the value of the standard deviation (s) can be determined by the following calculation:

$$s = k \cdot \gamma \quad (2.7)$$

where k is a track quality factor assumed to be related to the importance or traffic of the track. This value is 0.15 for high-speed tracks or a track with high traffic, and 0.20 for a track with low traffic (Skoglund, 2002). The types of trains define the velocity factor (γ) as listed in Table 2.3. An advantage of this method is it that differentiates between passenger and freight trains and considers the track quality.

Table 2.3 The velocity factor (γ). Source: Skoglund (2002)

Train type	Velocity (km/h)	Velocity factor (γ)
Passenger and freight trains	$V \leq 60$	1
Passenger trains	$60 < V \leq 300$	0.20
Freight trains	$60 < V \leq 140$	0.25

Dynamic concepts of the moving load

One of the main differences between the railway track and other structures is the fact that a train's moving load can induce complex dynamic effects on the track structure. In situ and laboratory testing

are essential to increase the knowledge in this area. The propagation of energy waves, energy dissipation, and particular moving-load speeds all require consideration in numerical models.

Two types of wave velocity should be considered for modeling, namely the Rayleigh surface wave velocity and the critical speed velocity (Krylov et al., 2000). Madshus and Kaynia (2000) conducted extensive research on the behavior of high-speed railway tracks on soft soil at critical train speeds in Sweden. They noticed that the displacements increased rapidly for train speeds above a certain value, with the displacements being upwards and downwards. They observed that for train speeds below the critical value, the downward displacement occurred directly below the bogies. However, vertical displacement under bogies moved toward the end of the train with 180 degree out of phase (Madshus and Kaynia, 2000). The same results were observed in many analyses by Sayeed and Shahin (2016) and Bian et al. (2014). According to Madshus and Kaynia (2000), critical velocity can be calculated using Equation 2.8.

$$V_{cr} = \sqrt[4]{\frac{4k_s \cdot E \cdot I}{m^2}}, \text{unit } \left[\frac{m}{s}\right] \quad (2.8)$$

where E is the Young's modulus of the beam, I represents the inertia of the beam, m refers to the mass per unit length of the beam, and k_s is the stiffness of the foundation.

In a homogeneous linear elastic material, stress waves travel indefinitely without changing amplitude. However, this type of behavior cannot occur in real conditions, and the amplitudes of stress waves in soil attenuate with distance. This attenuation can be attributed to two sources of energy dissipation; one involves the material through which the waves travel, and the other relates to the geometry of the wave propagation problem (Kramer, 1996). Material damping can be defined as conversion of the energy of a traveling wave to heat through friction between the particles. The conversion is accompanied by a decrease in the amplitude of the wave. The most common mechanism for energy dissipation is viscous damping. For most soils and structures, energy is dissipated hysteretically, which means by yielding or plastic straining of the material. Another type of damping occurs when the energy of a wave is spread over a large area, such as the infinite dimension of the foundation surface; this is called radiation damping.

2.5 Analytical calculation of the railway track

2.5.1 Beam on elastic foundation (BOEF)

With the ongoing operation of high-speed and heavy-haul railways, analysis of track structures has become a crucial topic in railway engineering research. The first step is application of an analytical solution to solve railway problems using theoretical models for each component of a track system. The first person known to have analytically solved a railway-track problem by considering the vibration source and transmission path of waves in soil was Horace Lamb. Many later works have continued to seek solutions for the problem of the elastic response to harmonic loads. However, for a railway track, the response to a moving load rather than a harmonic load should be considered. Fryba (1999) published

a valuable book for such problems. He explained three situations that could arise regarding the calculation of displacement under a moving point load in relation to S-waves and P-waves. The first occurs when the speed of the moving load is less than S-waves. The second occurs when the speed is higher than S-waves but smaller than P-waves. The third is when the speed is higher than P-waves.

A well-known analytical model to calculate the response of a railway track is the beam on elastic foundation (BOEF) model. This model was formulated and solved by Winkler in 1867. The model consists of a beam supported by springs and dashpots with a moving load on it. In 1888, Zimmermann developed a basic model for many other cases, including a double axle's load on the beam. This model can be used to calculate shear force, moment, and deflection in the rail through providing basic input, such as wheel loads and track parameters. Thereafter it is possible to calculate the rail seat forces and the average vertical stress between the sleeper and the ballast.

The main assumption in the model is that the rail is an infinite Euler-Bernoulli beam supported continuously by vertical elastic springs and dashpots. The basic concept of the model is shown in Figure 2.5. For more detailed concepts and mathematical formulations, readers are referred to the widely available literature on this topic. The foundation is characterized by the following equation:

$$p(x) = -k \cdot y(x) \quad (2.9)$$

where $p(x)$ refers to compressive stress applied on the rail at position x , which is the longitudinal coordinate. The track modulus is k , which according to Esvelde (2001) is the foundation resisting force per mm when the rail is deflected by 1 mm. The $y(x)$ term represents vertical deflection at position x .

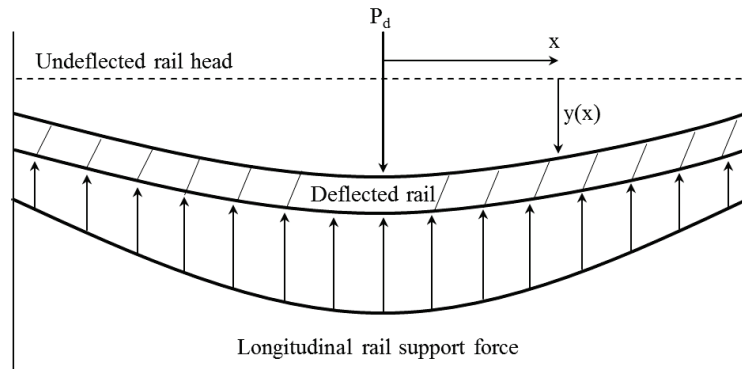


Figure 2.5 Beam on elastic foundation

To have a stable structure, static equilibrium between the foundation resisting force and the force that bends the rail must exist. Therefore, Equation 2.10 should be satisfied.

$$E \cdot I \frac{d^4 y}{dx^4} + ky = 0 \quad (2.10)$$

where E and I are Young's modulus and moment of inertia of the rail, respectively. The solution to this differential equation is presented as follows:

Here, L is the characteristic length or elastic length, which can be calculated from $L = \left(\frac{4EI}{k} \right)^{0.25}$.

$$y(x) = \frac{P_d}{2k \cdot L} e^{-\frac{|x|}{L}} \left(\cos\left(\frac{x}{L}\right) + \sin\left(\frac{|x|}{L}\right) \right) \quad (2.11)$$

The rail moment can be obtained by two times differentiation of the deflection and multiplying the result by EI, which gives rise to Equation 2.12.

$$M(x) = \frac{P_d \cdot L}{4} e^{-\frac{|x|}{L}} \left(\cos\left(\frac{x}{L}\right) - \sin\left(\frac{|x|}{L}\right) \right) \quad (2.12)$$

If the bending moment is known, Equation 2.13 can be used to calculate the tensile or compressive stresses along the cross-sectional symmetry line, where h_n is the distance from the neutral axis.

$$\sigma(x) = \frac{M(x)}{I} \cdot h_n \quad (2.13)$$

The BOEF model is linear; therefore, more complex loading conditions can be solved by superposition of solutions for single load case. Simply, deformations and reactions for each individual load should be summed to provide a result for the whole system. For example, deflection at $x = 0$ is given by Equation 2.14, where y is the whole system deflection, and x_i is the coordinate of the i^{th} axle.

$$y = y(x_1) + y(x_2) + \dots + y(x_i) \quad (2.14)$$

2.6 Numerical railway track modeling

2.6.1 General

The improved capacity of computers and the speed of processing complex algorithms, coupled with the need to overcome the limitations of analytical models, has ushered in a new era in engineering. Since introducing the numerical models, many researchers used different approaches to predict the behavior of railway tracks. These include the finite-element method (FEM) and the boundary element method (BEM). All the numerical methods are based on assumptions that are implemented in the basic calculations. However, those assumptions should not lead to unrealistic results or altering the basic engineering knowledge. As is the case with any computer-based work, each numerical approach has its advantages and disadvantages, depending on the nature of the problem and the computational time required. The cost of the specific engineering problem must also be considered. This section of the thesis describes the most common numerical approaches that have been used for simulation of different problems regarding the railway track, and summarizes their advantages and disadvantages.

2.6.2 Finite-element (FE) method

Goodman (1976) introduced the FEM in Geotechnical engineering, which provides a valuable tool to determine the dynamic response of complex geotechnical models. It yields detailed simultaneous predictions of stress distribution and displacements in the system, without assuming any failure modes. The use of FE analysis has become widespread and the method is popular in the geotechnical field, for controlling and optimizing engineering tasks.

The FEM offers the advantage of modelling the details of a railway track's geometry, and applying a more advanced soil constitutive model (e.g. non-linear behavior of material). In a dynamic FE analysis, reflection of the wave generated by the train load from the boundaries has an undesirable effect on the results of the simulation. Researchers have long attempted to overcome this problem and many methods have been introduced, including moving the boundaries far away from the loading area, which leads to higher computation costs. Another approach is the application of non-reflecting viscous boundaries which absorb the waves and prevent their reflection (White et al., 1977, Lysmer and Kuhlemeyer, 1969).

In FEM, a railway track can be modeled as a 2D plane strain model or as a 3D model. In a conventional ballasted railway track, the rail is discretely supported by the sleepers, whereas a 2D plane strain model requires an assumption that the transversal profile of the track does not vary longitudinally. Moreover, the load distribution of a train in a longitudinal direction cannot be modeled. The 3D FEM models can solve nearly all shortcomings and simplifications that limit a 2D model. The 3D version can model the discrete support for rails as well as the load distribution of a train in a longitudinal direction. Araújo (2011) conducted a complete 3D FEM simulation of a railway track, and Hall (2000) studied train-induced ground vibration using 2D and 3D FE models. Despite the benefits of a 3D model over the 2D model, the 3D model is more expensive and demands much longer computation times. Hall (2002) stated that in a 3D model, unlike in a real situation, load does not come from infinity and it leads to disturbances in the model, particularly at the boundaries and where the load enters and exits the model.

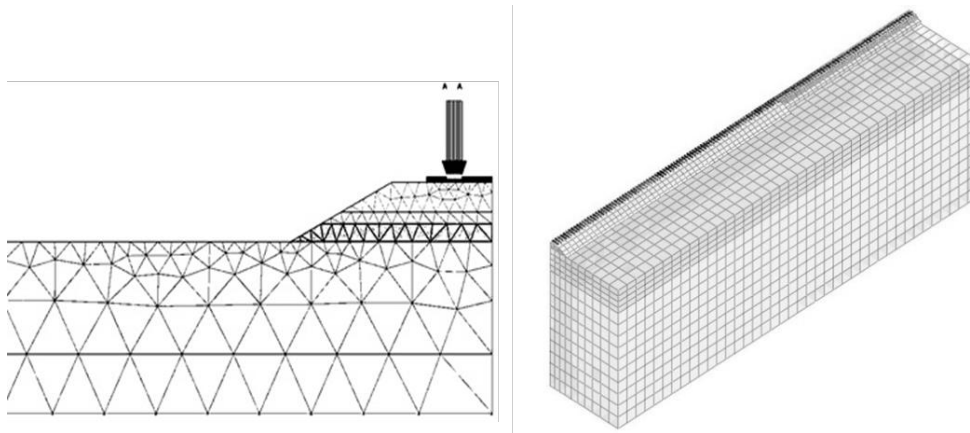


Figure 2.6 Example of a 2D (left) and 3D (right) symmetrical FE model of a railway track (Shahraki et al., 2014a, Shahraki et al., 2014b).

2.6.3 Boundary-element (BE) method

The BEM approach includes any method that uses the integration of partial differential equations to solve the boundaries of the model for a numerical solution. The BEM has some advantages over other numerical methods, such as FEM or finite differences. For example, BEM reduces space discretization by 1 so that only the boundary needs to be discretized; as a result, the computational time is less than that required by FEM. Moreover, BEM can simulate the half-space and wave propagation properly; hence, it is widely used to study problems related to wave propagation and ground vibration isolation (Tsai and Chang, 2009, Leung et al., 1990). However, it has difficulty with complex geometries and material non-linearity (Costabel, 1987). The most common way of using BEM for the track-soil model

is by defining the model in 2.5D, which is assuming the material and geometric properties to be constant along the load-moving direction, and it requires only the cross-section discretization, since the spatial coordinate along the track development is subjected to a domain transformation by a Fourier transformed.

2.6.4 Scaled boundary finite element (SBFE) models

The scaled boundary finite element method (SBFEM) is a novel semi-analytical approach to continuum analysis. It was developed by Song and Wolf (2000) and it combines the main advantages of FEM and BEM into one model. In this technique, as in the BEM, the dimension of spatial discretization is reduced by 1 and only the boundary of domain is discretized. Compared with BEM, the SBFEM does not require any fundamental solutions; it is a displacement-based method and can easily be coupled with the ordinary FE formulation (Ekevid and Wiberg, 2002). This new method is based on a transformation of the geometry using the scaled-boundary coordinate system, and it can easily handle unbounded problems.

2.6.5 Hybrid models

One of the main shortcomings of 2D railway modeling is the neglect of one dimension of the model. Therefore, new models should consider the effect of the third dimension, which can lead to a better simulation. Yang and Hung (2001) suggested a series of steps to study the ground vibration induced by moving load, which is a 3D problem, by a model that basically is 2D. To study the ground vibration in layered soil due to the passage of a train with different speeds, Yang et al. (2003) used the FE method with infinite boundary elements to prevent wave reflection.

Coupling of BEM and FEM provides a good method to save computation time when modeling tracks in the time domain. In addition, it allows for detailed geometric and material properties, and can be used particularly to solve problems related to ground vibration and wave propagation. The coupled FEM–BEM procedure was implemented by Estorff and Prabucki (1990) to analyze dynamic soil-structure interaction, including a trench problem. Alves Costa et al. (2012) introduced a 2.5D FEM–BEM model to investigate the ground vibrations induced by railway traffic. Sheng et al. (2006) modeled the train-track interaction while considering the track as an infinite layered beam and the soil as a layered half-space, by coupling 2.5D FEM and 2.5D BEM formulations. Galvín et al. (2010) presented a 3D FE–BE model to analyze the interaction between high-speed trains, soil and the track.

2.7 Linear and non-linear modeling of railway tracks

Many researchers have studied the track–soil response by assuming linear behavior of the track and soil layers. Their results have been reliable, which suggests it might be possible to neglect the non-linear behavior of material to achieve a faster simulation. Valuable work was done by Lombaert et al. (2006), who presented a linear 2.5D model for studying the dynamic interaction between the vehicle and the track. They modeled the passage of the Thalys trains to study induced vibrations; the results agreed well with measurements taken at the site. Jiang et al. (2014) used a linear 3D FE model based on a full-scale

test of a ballasted railway track to study the dynamic effect of different train speeds on the railway-track infrastructure. Hall (2002) implemented a linear 3D FE model to obtain the responses near the track, and used the dashpots in the boundaries of the mesh to consider the outgoing waves. The results of the model agreed well with the measured data. To achieve such agreement, Hall considered a reduction in the soil stiffness directly below the track, which was compatible with the induced shear strain. Duley et al. (2015) performed a linear numerical simulation based on a case study of a railway track, to propose a proper remedy for reduction of ground movement when the train's speed approaches the critical velocity of a track. They concluded that increasing Young's modulus reduced the displacement but also increased the critical speed, whereas increasing the density reduced both the critical velocity and displacement.

Many other studies have investigated the effect of the passage of high-speed train on a railway track by considering only the linear behavior of materials. The researchers have used different approaches, such as 3D or 2.5D FEM, BEM, or a combined FE–BE model (Galvín and Domínguez, 2009, O'Brien and Rigos, 2005). Generally, when modeling a railway track, it is best not to consider non-linear behavior. The reason is the limited applicability of non-linearity in real engineering works. Moreover, non-linear data can dramatically increase the computational time and physical memory required by the computers.

However, non-linearity is a real phenomenon, and non-linear behavior is studied for track components such as ballast and sub-ballast or the foundation soil. To achieve more accurate results from a numerical simulation, the choice of a proper material model is essential. Many material models have been developed to simulate cohesive or cohesionless materials. Nonetheless, as already explained, a non-linear response of the railway track under the passage of a high-speed train is rarely taken into account in simulations.

Shih et al. (2016) used a non-linear material model based on shear modulus reduction curves in a commercial FE program, to study the ground vibration when the train speed approached the critical speed. They observed that the critical speed obtained from the linear model was higher than that obtained from the non-linear model, and the linear model underestimated the displacement in speeds close to critical velocity. Nevertheless, the results of linear and non-linear models were in close agreement for speeds lower than critical velocity. Alves Costa et al. (2010) modeled a railway track and its subgrade by considering the non-linear behavior of materials for track components and subgrade. They stated that the difference in displacement between the linear and non-linear model for trains travelling at low speed was negligible, but with increasing speeds the differences became more obvious. Banimahd and Woodward (2007) applied a 3D non-linear elastic FE model to study the response of a track to different train speeds. The results showed that taking the non-linearity of subgrade into account had minimal effect for low speeds, but this effect increased as the train speeds increased.

2.8 Ground improvement methods

Many ground improvement methods are based on constructing strong vertical column elements, made from various materials – such as stone, sand, grout, or soil-cement columns. Many methods for improving the ground enhance the strength parameters of the soil and decrease the future settlement at

the site. Around the world, various structures have been built using vibro-concrete columns, deep soil mixing, soil jetting, compaction grouting, and stone columns. One of the main benefits of ground improvement is that the vertical elements can be shorter compared with deep foundations. In other words, during installation of the column elements, the surrounding weaker soil is compacted (e.g. due to the vibration and compaction). Hence, these methods can be more economical than deep foundations with a shorter construction time.

Among all ground improvement methods, the stone-column technique is one of the most economical and environmentally friendly treatments for weak ground. The method was first developed in 1956. In this method, the weak ground is drilled at designated distances and diameters, using special vertical drill cars. The holes are then filled with coarse aggregate such as stones, while being densified using a deep vibrator (Figure 2.7).

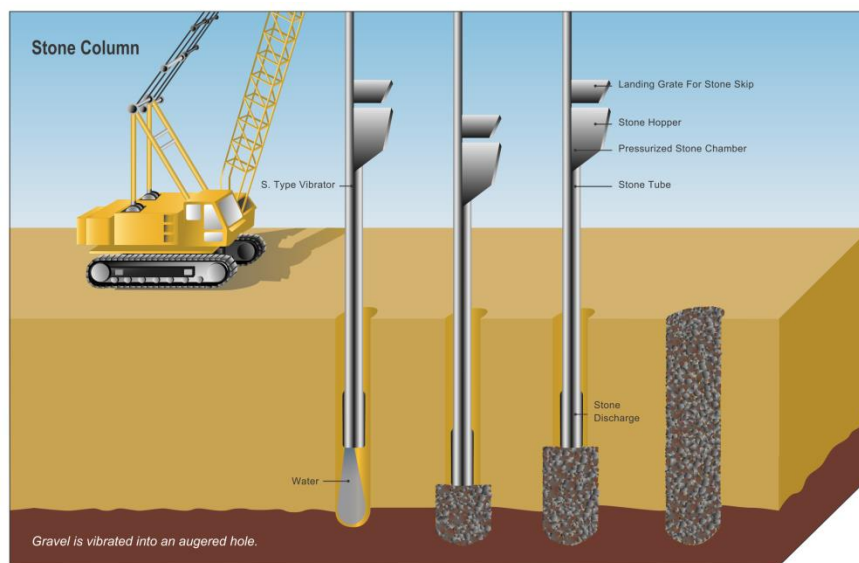


Figure 2.7 Schematic view of construction of stone columns (Raju et al., 2004)

As mentioned earlier, deep foundation elements transfer the load from the upper structure to the stiff layer (e.g. bedrock) so that the weak soil is neglected in transferring loads. The stone columns and weak soil together carry the load, but the amount of the load carried by each depends on its relative stiffness. Ground improved by stone columns shows smaller stress differentials than deep foundations. Ideal stress distribution patterns for deep foundation systems and for stone column systems are depicted in Figure 2.8.

Stone columns can be used to control the settlement, dissipate excessive pore water pressure, accelerate consolidation, and enhance the load-bearing condition of the surrounding soil. The columns achieve these effects by improving the density, strength, and deformation properties of the soil. A wide range of soils, from loose silty sands and soft silts to marine clays and peaty clays, can be treated by constructing stone columns. In addition, many engineering structures – including simple earth embankments, bridge approaches, high-speed railway embankments, offshore structures, airport facilities, power plant structures, and large storage tanks – can be supported by stone columns. Moreover, the technique can mitigate the hazard of soil liquefaction in seismic regions.

Many parameters control the effectiveness of stone column applications, such as diameter and spacing between the columns, length of the stone column, and the strength ratio between the soil and stone column. A typical diameter of a column is 0.8 m to 1.1 m, and spacing ranges from 1.5 m to 2.5 m. In practical works the design of the stone column is carried out based on the Priebe (1995) approach, which includes the loading conditions, soil parameters, and properties of the granular column material.

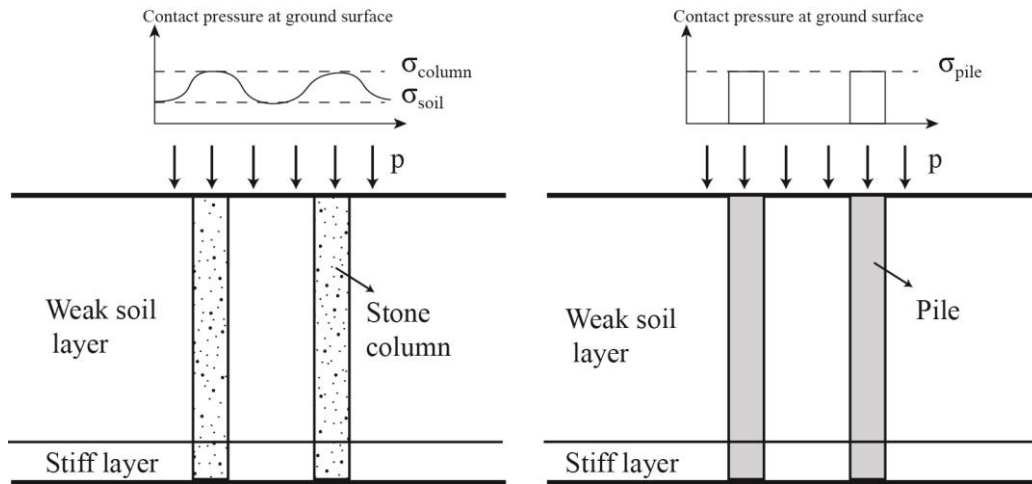


Figure 2.8 Ideal stress distribution pattern. Left, stone column; right, deep foundation (pile).

Poorooshasb and Meyerhof (1997) introduced elastic analyses to study the settlement reduction of a raft foundation resting on reinforced soft soil with end-bearing stone columns. They showed that the spacing and degree of compaction of the material in the columns controls the stiffness of the whole system composed of the columns and the weak soil. Important factors in the design of stone columns are the grain size of the column's material, and the stiffness of the column. Many researchers have studied stone column materials; for example, Isaac and Girish (2009) studied stones, gravel, river-sand, sea-sand, and quarry dust in laboratory experiments on these materials installed in clay. They found that stones were the most effective material and gravel was the second most effective material. Installation of stone columns can be classified into four groups: the wet top-feed method, the dry bottom-feed method with a purpose-built base machine, the dry bottom-feed crane-hung method, and the offshore bottom-feed method.

2.9 Soil improvement under railway tracks

Railway infrastructure demands a high level of performance in terms of settlement and the stability of the track. Constructing railways on ground that contains soft soil deposits leads to engineering problems such as excessive settlement and stability problems. Several remedies have been proposed to avoid or reduce those problems; for instance, replacement of soft soil or constructing piles or stone columns.

Stresses on the railway subgrade should be minimal to prevent irreversible deformation and to provide a stable support for the track. Increasing the level of stress and deformation causes progressive degradation of the track geometry and decreases the safety and ride quality. Improvement of the

subgrade depends on enhancing the underlying weak natural ground formation. This improvement reduces the rate of track geometry degradation and lowers maintenance costs. Ground improvement is needed when the natural subsoils are unable to provide the required design criteria for a railway track. The use of stone columns as a method of soft soil improvement has been successfully implemented around the world and they may be provided in areas where subsoil consists of more than about 5 m of thick soft cohesive soil. The dry or wet method of installation can be used depending on the existing railway track and water sources. The dry bottom-feed method causes minimal changes in the consistency of cohesive soils, and for the railway track has less risk of unacceptable settlement compared with the wet method. Nevertheless, additional ballast and sub-ballast material should be available in case leveling of the track is required.

Katzenbach and Ittershagen (2004) studied the deformation and bearing behavior of soil which was improved using Lime-cement columns. Large-scale tests were conducted under dynamic loading conditions, as not much research has been done on soils subjected to these conditions, particularly with respect to railway tracks. For soil improvement under railway tracks, not much information is available regarding the impact of train speed and train weight on the depth of improvement and arrangement of columns for the improvement of soil. The results of investigating and observing the dynamic responses, using various measuring devices for different lime-cement column placement configurations with different depths of the columns, showed that ground improvement in which the columns were extended to the stiff layer achieved the best results.

Guetif et al. (2007) evaluated the improvement of the characteristics of soft clay in which stone columns were installed. The primary aim of that study was to assess the increase in Young's modulus in a soft clay soil which develops after the installation of stone columns. Although several studies have examined soil improvement, they have mainly used field test data or laboratory tests. Guetif et al. (2007) proposed a method involving numerical simulation to study the vibro-compaction technique. The results showed an evident improvement in the soft soil characteristics after stone column installations by vibro-compaction. In the first phase, after the column installation, a significant increase in the pore water pressure was noted, whereas the effective mean stress remained unchanged. A 4-fold increase in effective mean stress in the column material was also noted, compared with that of the soft clay. In the second phase, after the primary consolidation (11 months), there was a noticeable increase in the effective mean stress due to the increase in the radial stress, and the excess pore water was dissipated. A new Young's modulus was adopted for this reinforced soil within the zone of influence. As the radius of the influence zone is known, improved column spacing can be adopted. As there is an improvement in Young's modulus, this change should be considered in the design procedure.

2.10 Stone column analysis

2.10.1 Analysis of embankment founded on stone columns

The typical assumed failure mechanism for an embankment constructed on stone columns is a sliding failure surface, which mobilizes the shear strength of the columns and the soil. There are three common

approaches to the analyses. Circular sliding surface and average strength method have been developed to determine average shear strength for the combination of the stone columns and the surrounding soil. In the profile method, stone columns are considered to be vertical strips running through the soil.

In slope stability analyses, the first failure mode is assumed to be shearing. However, for an embankment founded on stone columns, Bachus and Barksdale (1989) suggested that composite strengths cannot be used for an area of replacement less than 20% due to the free movement of the soil between adjacent stone columns. The most critical stability condition occurs for a short-term and undrained condition of soft soil surrounding the columns. However, embankment stability improves when the consolidation is finalized.

The main factors that control the shear strength of composite systems are the shear strength of the soil, the shear strength of the columns, and the area replacement ratio. Over time, after construction, the frictional shear resistance of the columns rises because of the increased stress concentration ratio. The stress concentration ratio is the ratio of the total stress in the column to the total stress in the soil. Immediately after loading, the stresses in soil and column are equal; as consolidation occurs, the stress concentration ratio increases because the load is transferred to the stiffer elements, namely the stone columns.

Stone columns can be constructed either to be short (floating columns) or to extend to the bedrock (hard layer), in different patterns. Figure 2.9 shows three geometrical patterns and the influence area of a unit cell of stone columns. The selection of column pattern is most often based on workability, load capacity, and cost. Each column acts within a cylindrical cell with a unit cell diameter denoted by d_e . Balaam and Booker (1981) denoted the relationship between the influenced radius and the column spacing as $d_e = c \cdot s$, where s is the spacing (from center to center of the columns) and c is a constant having values of 1.13, 1.05 and 1.29 for square, triangular and hexagonal patterns, respectively.

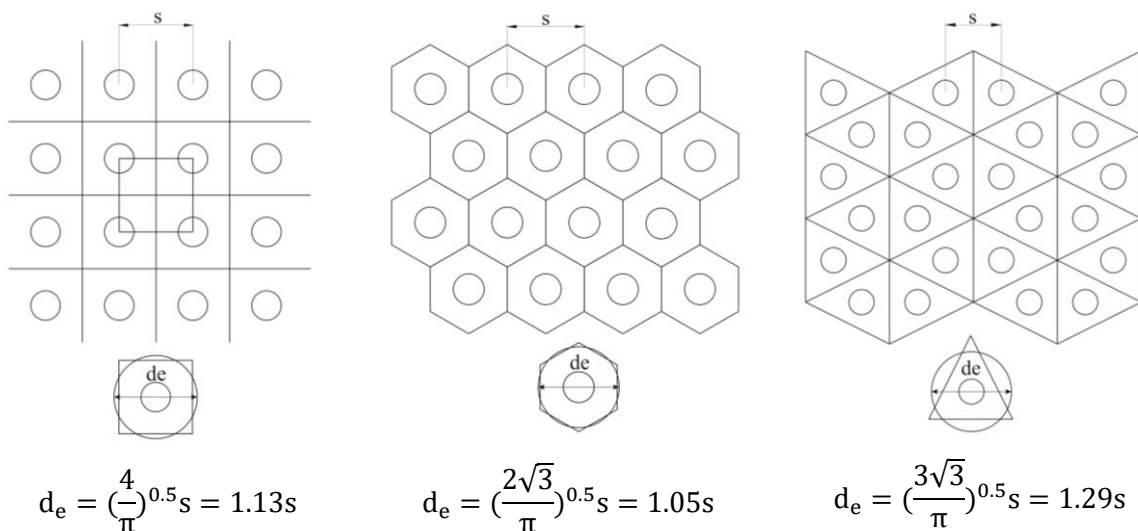


Figure 2.9 Orientation of stone columns: (a) square pattern (b) triangular pattern and (c) hexagonal pattern.

2.10.2 Circular sliding surface method

The Japanese method is also called the circular sliding surface method. It was developed for analyzing sand compaction piles but can also be used for stone columns. This method considers the composite shear strength for a circular failure surface, as shown in Figure 2.10.

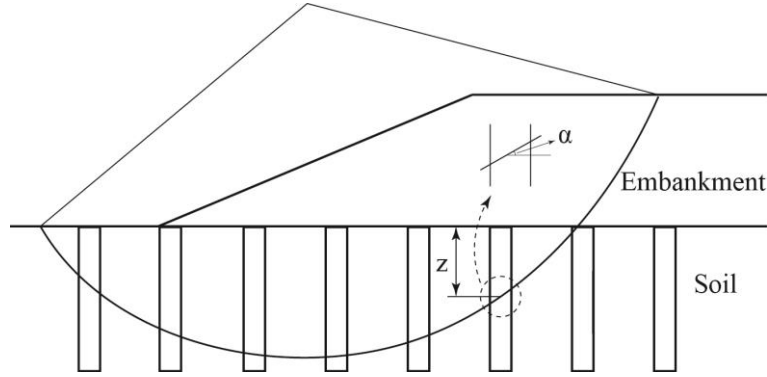


Figure 2.10 Circular Sliding Surface Method (after Filz and Navin, 2006)

Based on the area replacement ratio and the strength of the soil and stones, composite shear strength along the failure surface can be calculated from Equation 2.15. This equation considers the shear strength of stone columns under drained, and that of soil under undrained conditions.

$$\tau = (1 - a_s)[c_u + (z \cdot \gamma_{\text{soil}} + \sigma \cdot \mu_{\text{soil}})\tan\phi_{\text{soil}} \cdot \cos^2\alpha] + a_s(z \cdot \gamma'_{\text{col}} + \sigma \cdot \mu_{\text{col}})\tan\alpha'_{\text{col}} \cdot \cos^2\alpha \quad (2.15)$$

where τ is the composite shear strength along the sliding surface, a_s is the area replacement ratio, c_u is the undrained cohesion of the soil, and the unit weight of the soil and column are γ'_{soil} and γ'_{col} respectively. The area replacement ratio a_s can be calculated by Equation 2.16.

$$a_s = \frac{d^2}{(d_e^2)} \cdot 100 \quad (2.16)$$

The distance from ground surface to failure surface is z . The average vertical stress from a constructed embankment is σ and inclination of the failure surface is α . The ratio of stress change in the soil and stone column from the embankment load to the average applied vertical stress from the embankment are μ_{soil} and μ_{col} . The undrained and drained friction angle of the soil and column are ϕ_{soil} and ϕ'_{col} , such that for saturated clay in the undrained loading condition, $\phi_{\text{soil}} = 0$. After calculating the composite shear strength to determine the stability of the ground, the ordinary method of slices should be applied.

2.10.3 Average strength parameter method

This method is also based on determining the composite shear strength parameters of the ground. However, in this method, the average cohesion, density, and average friction angle should be calculated. Average cohesion is obtained based on the cohesion of the soil and the area replacement ratio, as shown in Equation 2.17.

$$c_{\text{ave}} = c_u(1 - a_s) \quad (2.17)$$

where c_u denotes the undrained cohesion of the soil, and a_s is the area replacement ratio.

Average unit weight can be computed by Equation 2.18.

$$\gamma_{ave} = (1 - a_s)\gamma_{soil} + a_s \cdot \gamma_{col} \quad (2.18)$$

where γ_{soil} , and γ_{col} are the unit weights of the soil and the column, respectively.

To find the average friction angle, the orientation of the assumed failure surface should be considered along with the friction angle of the soil and the stone columns. This is represented in Equation 2.19.

$$\tan\phi_{ave} = \frac{(1 - a_s)\tan\phi_{soil} + S_r \cdot a_s \cdot \tan\phi_{col}}{1 + a_s(S_r - 1)} \quad (2.19)$$

where, ϕ_{soil} and ϕ_{col} are the friction angle for the soil and the column. The S_r term is the stress ratio appropriate to the orientation of the failure surface at that location, as determined by Equation 2.20:

$$S_r = 1 + (n - 1)\cos\alpha \quad (2.20)$$

where n is the stress concentration ratio, and α is inclination of the assumed failure surface.

All these average parameters should be used in slope stability analysis approaches such as Bishop's or Spencer's methods.

2.10.4 Profile method

In the profile method, stone columns are simplified to the equivalent “strips” in profile. The width of the strip depends on the area of replacement ratio, the column distance in cross-section, and the arrangement of stone columns in square, triangular, or hexagonal patterns. Figure 2.11 shows the general idea behind conversion of the cylindrical stone columns to strips.

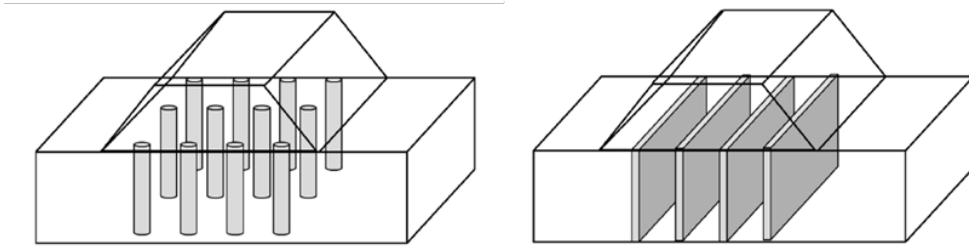


Figure 2.11 Conversion of the discrete cylindrical stone columns (left) to equivalent strips(right) (Castro, 2017).

An example of strip calculation for a triangular arrangement of stone columns is shown in Figure 2.12. The distance between two adjacent columns in a plane section is represented by s , and the width of the strips in a 2D plane strain condition can be calculated from Equation 2.21:

$$w = a_s \cdot s \quad (2.21)$$

where w is the width of strips, and a_s is the area of replacement ratio. The area replacement for a triangle pattern of stone columns that have a diameter d is equal to:

$$a_s = \frac{d^2}{(1.05^2)(s^2)} \quad (2.22)$$

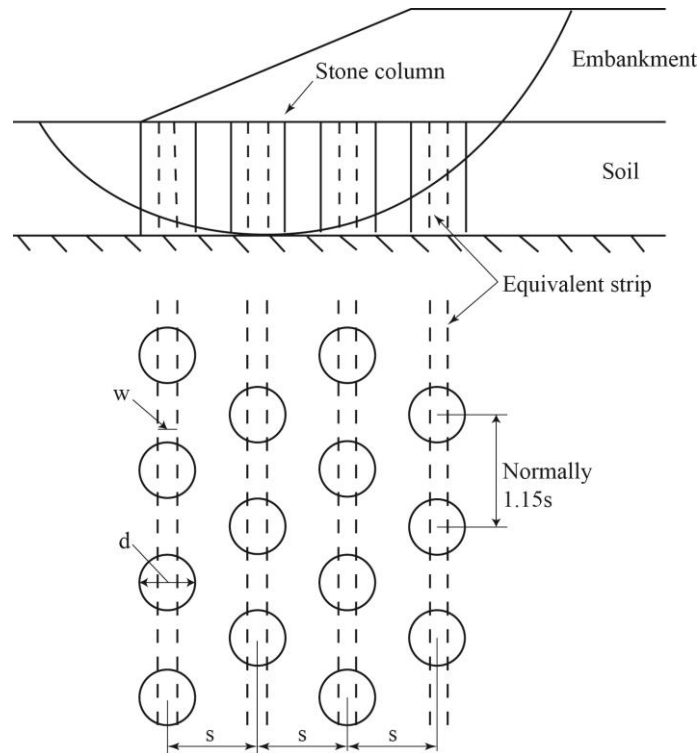


Figure 2.12 Stone column equivalent strip for triangular pattern (after Filz and Navin, 2006)

Equivalent strips should be calculated due to the assumption that cross-sections are uniform over the length. By contrast, along the length, stone columns are located at specific distances and the spaces between them are filled with soil. Therefore, by considering the area of replacement and distance between the columns, the width of strips can be calculated and is assumed to remain constant over the length.

2.10.5 Comparison of analysis methods

Among the above-mentioned approaches, the average strength parameter method is inappropriate for use by a computer program. This is because of changes in the inclination of the failure surface, which lead to varying average friction angles. Moreover, in this method the stress concentration in columns is the summation of the embankment load with the soil weight above the failure surface. By contrast, in the circular sliding surface method, only the weight of the embankment is considered in calculating the stress concentration. Hence, different results can be obtained for the same embankment through using these two approaches.

Goughnour and Barksdale (1984) recommended the use of the profile method together with FEM to analyze the stability of an embankment on stone columns. They supported their recommendation with

settlement observations of an embankment constructed on stone columns, for a period of two years. The results of four different methods, including Priebe (1995) method, which are used to estimate the settlement were compared with the field measurements. Goughnour and Barksdale concluded that the profile method together with FEM yielded a much better prediction than other methods.

3 Field Measurements

3.1 Introduction

Field measurement refers to either the collection of train passage data on existing tracks for use with statistical analysis, or the use of direct field measurements at proposed sites. With regard to numerical simulation, it is necessary to obtain experimental data or field measurements to assess the ability of a model to solve a physical problem. Additionally, experiments are needed to provide any physical characteristics that cannot be easily modeled in numerical simulations.

For high-speed railway tracks, few data are available regarding field measurements, which makes it difficult for researchers to validate their numerical models. Strict safety restrictions by railway companies regarding field measurements taken close to railway tracks is one reason; these restrictions are intended to prevent accidents which might lead to changes in train schedules or delays. Degrande and Schillemans (2001) freely published their measurements from the far- and near-field regions of the Brussels–Paris high-speed railway track in December 1997. They used accelerometers to measure the passage of nine Thalys trains. Thereafter, by numerical integration, those measurements were converted to velocity time histories. Many studies have subsequently been conducted using those field measurements (Shih et al., 2016, Paolucci et al., 2003, Sheng et al., 2003, Degrande and Schillemans, 2001, Madshus and Kaynia, 2000).

More recently, Connolly (2013) performed a series of field measurements on a high-speed railway track in Belgium, near to the French border. These data were obtained for the passage of two types of high-speed trains, Thalys and TGV, at various speeds. The data are used in this work for validation of the proposed simplified train passage model. However, the measurements covered only the near- and far-field regions around a railway track, and no instrument was used during construction or in deeper soil layers (including subgrade and subsoil). Therefore, to check the validity of the simplified model for different conditions, a second set of measured data for different soil layers under a railway track is also used in this study. These data were obtained from Wegener (2012), who presented measurements on a conventional railway track in South Germany under the passage of a typical Austrian train, Railjet, at a speed of 130 km/h.

This chapter gives an overview of the field measurements of the railway tracks in Europe that are described above. The measurements included three types of train sets as well as different train speeds. All these valuable measurements were used for validation of the numerical simulations, which are explained in the next chapter.

3.2 The first test site: Belgium

3.2.1 Track and soil characteristics

The first site was an at-grade double-track railway section at Mons in the south of Leuze-en-Hainaut in Belgium. The superstructure of the track consists of continuously welded UIC60 rails that are fixed to the B70 pre-stressed concrete sleepers by means of fasteners; a railpad 0.01 m thick is located between the rail and sleepers. All these elements are supported with 0.3 m ballast, 0.2 m sub-ballast, and 0.5 m subgrade, which are constructed on three distinct natural soil layers. A top silty layer has been supported by a layer of sand, with a clay layer at the bottom. The geometry of the track is shown in Figure 3.1.

According to Connolly (2013), material properties of soils at the site have been determined through a multi-channel analysis of surface wave methods, in conjunction with a survey of existing soil data. Soil properties as reported by Connolly (2013) are congruent with the data from a study by Kouroussis et al. (2011), who conducted spectral analysis of surface wave tests on nearby soils. Type of soil in various conditions show different damping characteristics, but in the FE model, each layer was assumed to be equally damped. The track elements and soil properties appear in Table 3.1.

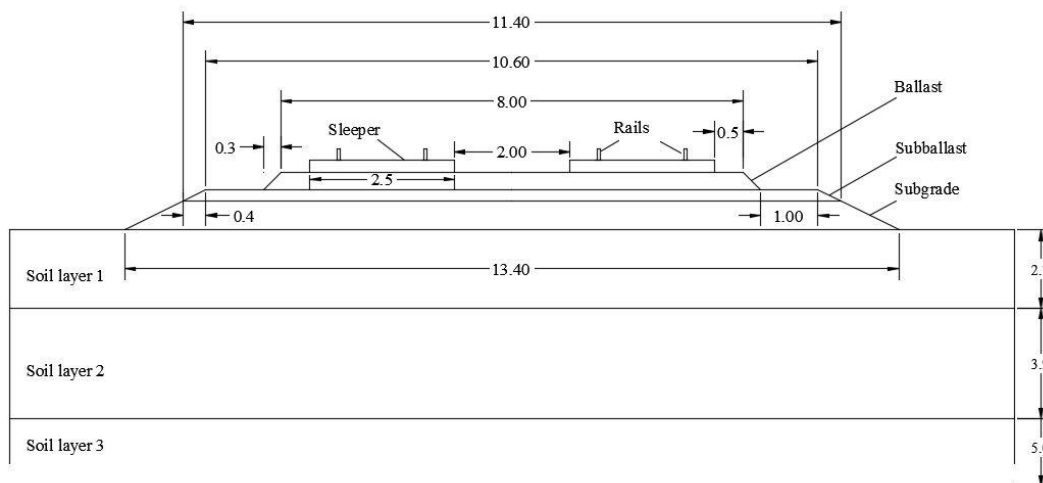


Figure 3.1 Geometry of track in the first site (m).

Table 3.1 Properties of the first site (Connolly, 2013)

	Young's modulus (MPa)	Poisson's ratio (-)	Density (kg/m ³)	Thickness (m)
Rail	210000	0.25	7900	
Sleeper	30000	0.3	2400	0.2
Ballast	100	0.35	1800	0.3
Sub-ballast	300	0.35	2200	0.2
Subgrade	127	0.35	2100	0.5
Soil layer 1	129	0.3	1600	2.7
Soil layer 2	227	0.3	2000	3.9
Soil layer 3	659	0.3	2000	5.0

3.2.2 Trains

TGV train (Train à Grande Vitesse)

The TGV trainsets are manufactured by Alstom and began operating commercially in 1993. Trains consist of two power cars at each end, six passenger cars in the center, and two lateral cars connecting the power and passenger cars (Figure 3.2). Field data have been measured under passage of the train at a speed of 280 km/h. Details of the specifications of TGV trainsets are shown in Table 3.2.

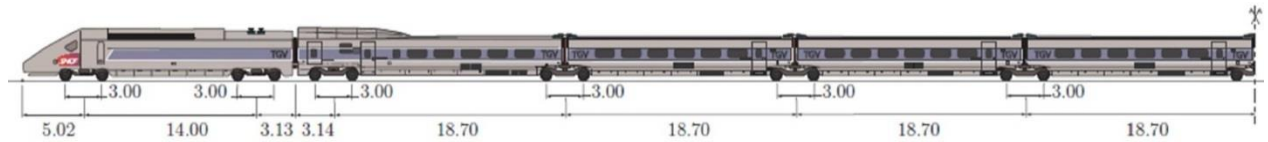


Figure 3.2 TGV train (Connolly, 2013)

Table 3.2 TGV specifications (Connolly, 2013)

	Driving & central cars	Passenger cars
Half-car body mass [kg]	25000	17500
Bogie mass [kg]	5800	3300
Wheelset mass [kg]	1600	1750

Thalys train

Thalys is an international high-speed train that began service in 1996. It has evolved from the TGV and is manufactured by Alstom. The maximum speed of the Thalys train is 300 km/h, and its total length is 200 m (Figure 3.3). Field measurements used in this study were recorded under passage of a train at a speed of 299 km/h. Table 3.3 shows the specification of the Thalys train.

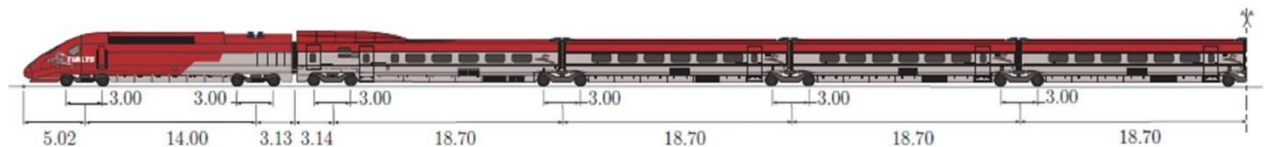


Figure 3.3 Thalys train (Connolly, 2013)

Table 3.3 Thalys specification (Connolly, 2013)

	Driving cars	Lateral cars	Passenger cars
Half-car body mass [kg]	26721	14250	20426
Bogie mass [kg]	3261	1400	8156
Wheelset mass [kg]	2009	2050	2009

In this study, as is standard practice (see Table 2.2), in all simulations an axle load of 170 kN for driving and passenger cars, for both TGV and Thalys trains, is assumed.

3.2.3 Measurements

Over a period of three days, Connolly (2013) recorded the passage of 50 trains at the site: 23 Thalys trains, 15 TGV trains, and 12 Eurostar trains. Only 29 of these were travelling on the track closest to the measurement devices and 21 were on a further track. Geophones were implemented at the site as measuring equipment. They were mounted on 150-mm spikes, perpendicular to the track, and each three-component sensor was aligned to the desired orientation using a spirit level. According to several researchers (Kouroussis et al., 2014, Kouroussis et al., 2013, Connolly et al., 2014), all signals were processed using a 24-channel Geode exploration seismograph and recorded using a Panasonic Toughbook CF-19. At this site, eight low-frequency, three-component SM-6 geophones, with a sensitivity of 28.8 V/m/s were located at distances of 9 m, 11 m, 15 m, and 19 m from the rail of the nearest track. The arrangement is shown in Figure 3.4.

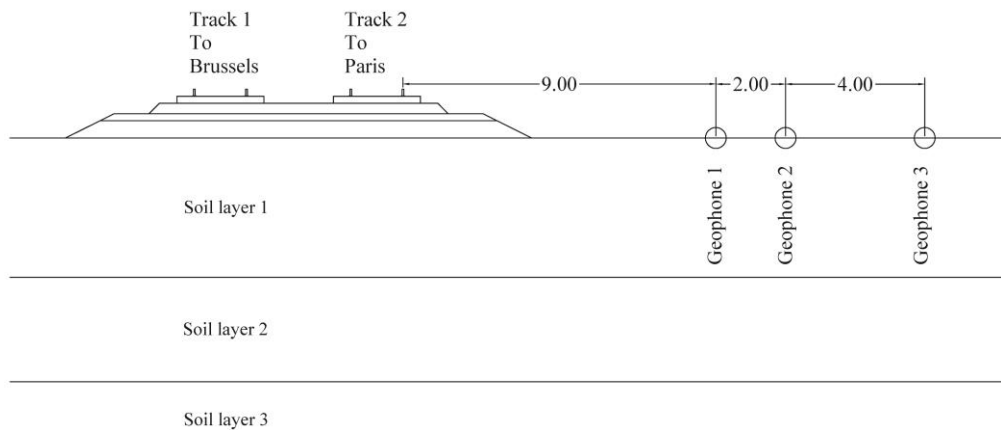


Figure 3.4 Location of the geophones (9, 11, and 15 m from nearest track) at the site.

The natural frequency of the SM-6 geophones is 4.5 Hz. This means that vibrations propagating at frequencies less than 4.5 Hz are not dampened, because of the geophones' characteristics. To overcome this limitation, the signals should be post-processed and a filter must be applied to the frequency content between 0 Hz and 4.5 Hz. All post-process procedures and filtering are performed by the provider of the measured data. However, accelerometers are a better instrument to measure vibrations at low frequencies – for example, below 4.5 Hz. They help to avoid the post-processing steps that are needed with geophones. Nevertheless, they are sensitive to adverse weather conditions, whereas geophones are more durable and wind or rain do not interfere with the recorded signal.

Recorded signals from the passage of TGV and Thalys high-speed trains at speeds of 280 km/h and 299 km/h, respectively, are shown in Figure 3.5. It is common knowledge that vibration decreases dramatically as one moves farther from the track. When the train speed is lower than the Rayleigh wave speed, vibration intensity depends more on the distance from the track than on train speed. The results

show that recorded vertical velocity decreased exponentially from near to far distances relative to the track. These results are used for validation of the simple model that is presented in this thesis.

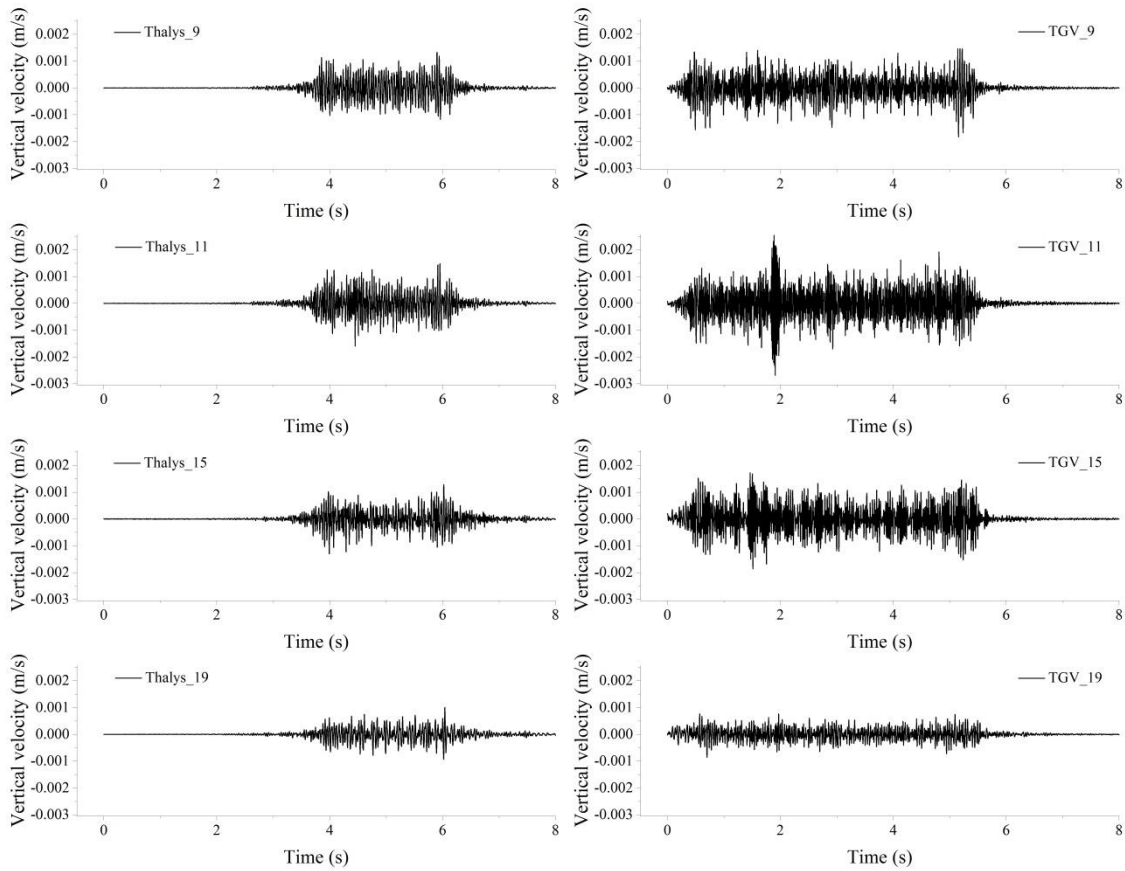


Figure 3.5 Recorded signals from the passage of two trains (TGV and Thalys) at different speeds (280 km/h and 300 km/h) at different distances from the nearest track (9, 11, 15, and 19 m). Data provided by Connolly (2013).

3.3 The second test site: Germany

3.3.1 Track and soil characteristics

A busy railway track in southern Germany was chosen for the second site investigation. The track is constructed of ballast (0.3 m thick), sub-ballast (0.5 m thick), and a capping layer (0.5 m thick). It contains continuously welded UIC60 rails with a mass of 60 kg/m^3 , which are supported by railpads (0.01 m thick) and monoblock concrete sleepers, B70. The track was laid on a low embankment of granular soil layers with a sleepers center-to-center measurement of 0.6 m. All layers are supported by soft soil sediments such as clay and peat. The geometry of the track is illustrated in Figure 3.6.

This track has needed routine tamping every six months, which increases the maintenance costs sharply. When the track was renewed to reduce the cost of tamping, a 50-cm layer of coarse material from a drained granular mixture was constructed in the superstructure. The track has been subjected to different types of measurements and many laboratory tests to assess the dynamic stresses and vibration. All the

measurements have been funded by DB Netz AG, because similar problems occur on other tracks throughout Germany. The main goal of the investment was to assess the usefulness of renewing and retrofitting the track (Wegener, 2012, Vogel et al., 2011).

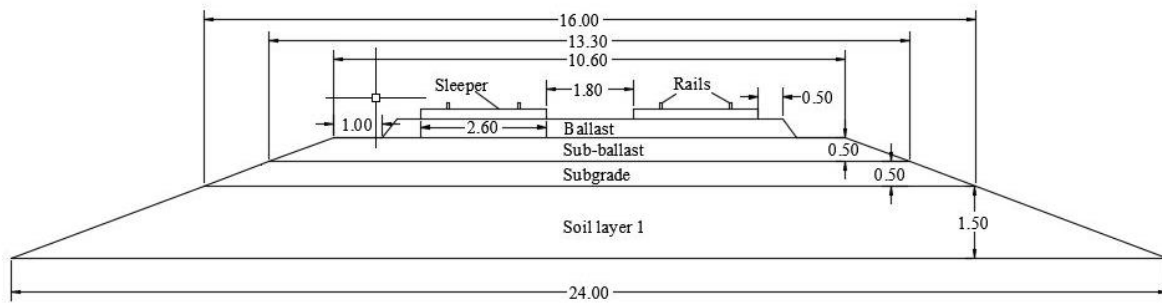


Figure 3.6 Superstructure geometry of the second site (m).

A series of geotechnical laboratory and field tests were conducted to identify suitable material properties for modification and improvement of the track. The boreholes were later used for locating the geophones and other measurement devices. With the help of field tests, the compression and shear wave velocities were determined. Thereafter, several other soil material properties – for example the Poisson's ratio – were calculated by simple mathematical relationships. The wave velocities in the first two soil layer were higher than those in the subgrade and it increased with depth. The material properties of different soil layers reported in the literature (Vogel et al., 2011) are summarized in Table 3.4. It should be noted that the material damping ratio for all soil layers was considered to be 2%.

Table 3.4 Material properties of the second site

	S-wave (m/s)	P-wave (m/s)	Poisson's ratio (-)	Density (kg/m ³)	Thickness (m)
Ballast	230	430	0.30	1750	0.3
Sub-ballast	260	490	0.30	2200	0.5
Subgrade	130	320	0.40	2000	0.5
Backfill	110	370	0.45	1730	1.5
Soil layer 1	85	370	0.47	1030	3.0
Soil layer 2	180	1050	0.485	2080	10

3.3.2 Railjet train

This railway track operates under passage of different types of trains at various speeds, bogie arrangements, and axle loads. It is used by high-speed passenger trains travelling at 130 km/h, regional trains with a speed of 120 km/h, and freight trains with speeds of up to 90 km/h.

The Railjet is a high-speed train of the Austrian Federal Railways (ÖBB) and is one of the most modern and luxurious trains in Europe. It operates mainly in Austria, with international connections to Germany, Switzerland, Hungary, and Czech Republic. Railjet trains can travel at a maximum commercial speed of 230 km/h and are manufactured by Siemens. Trains include the locomotive with an axle load of

215 kN, and passenger cars with an axle load of 130 kN. Each car of the train has its own bogies and cars do not share bogies (Figure 3.7). In this study, vibrations recorded for the speed of 130 km/h are analyzed.

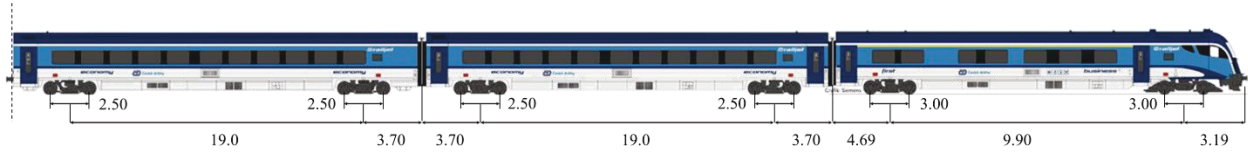


Figure 3.7 Railjet train (m)

3.3.3 Measurements

At the second site the vibration measurements were again recorded by geophones. Geophones (with a sensitivity of 30 V/m/s) were used to measure the induced voltage of a vibration velocity. Two types of geophones (with either one or three components) were installed in the shoulder of the embankment and at various depths of the substructure. The locations of the geophones and the soil stratifications are shown in Figure 3.8. To evaluate the numerical simulation, only the results of geophones in the axis of the track were used in this study. For the three-component geophones, only the vertical component of vibration was considered as the other components are negligible compared with the vertical one.

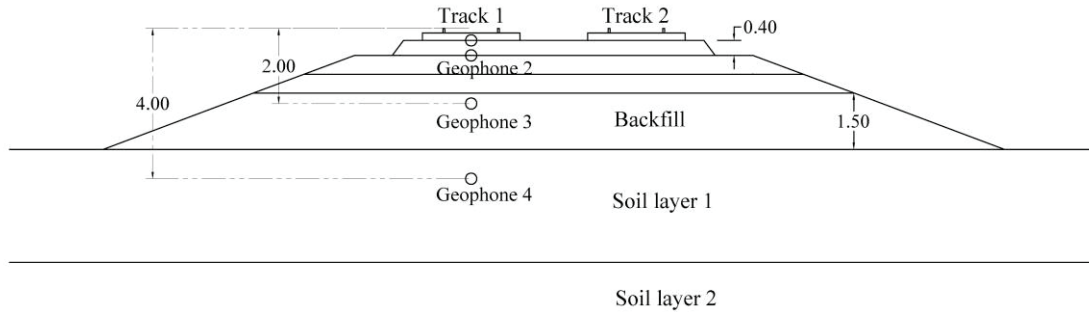


Figure 3.8 Soil stratifications and location of geophones (m).

The geophones recorded the whole passage of the trains. However, for the sake of simplification and considering the symmetric loading of trains, limited data were considered, namely one locomotive, the first passenger car, and one bogie from the adjacent car. The time history of the vertical vibration velocity was re-plotted for the four geophones located at different depths of the axis of the track (Figure 3.9). As expected, the velocities recorded by deeper geophones were smaller than those at the upper ones; this finding agreed with the expectations based on the material and geometrical damping.

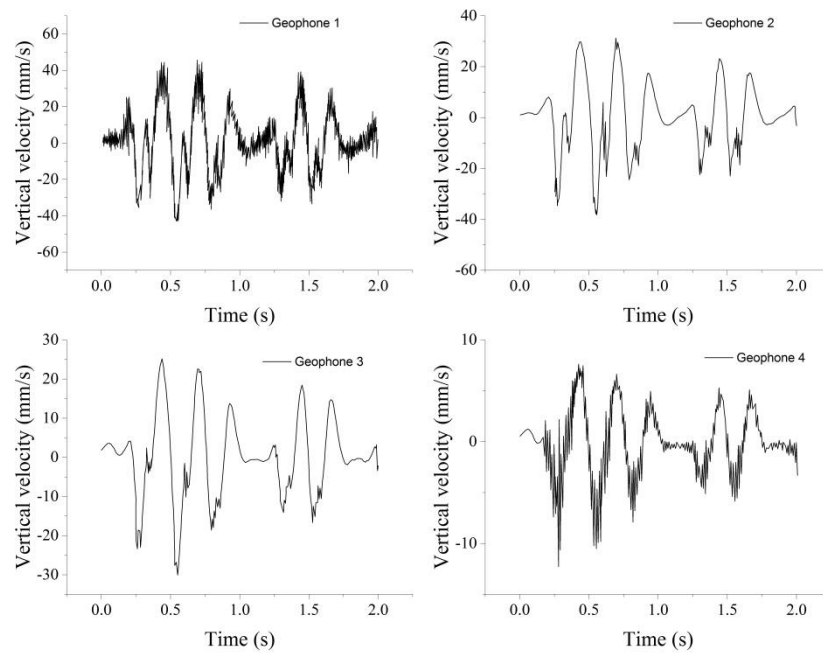


Figure 3.9 Results of the second site, re-plotted (after Wegener, 2012)

4 Railway Track Numerical Simulation

4.1 Introduction

In recent decades, numerical methods have developed rapidly. Current numerical methods, especially the finite element (FE) method, play an important role in the design of more complex engineering problems. However, without validation it is difficult to assess whether a model can predict results that are accurate for the real physical problem. Field measurements are required to validate numerical prediction models.

Field measurements and geometry at two sites were explained in the previous chapter. Those sites are used as a basis for validation of numerical simulation studies in this chapter. First, the results of 3D simulations are compared with the field measurements. Then a 2D model is introduced, validated, and compared with the field data and 3D results. The developed and validated 2D model is used to identify the effect of stone columns in a simplified 2D plain strain model by considering the dynamic effect of the passage of high-speed trains.

The results of both simulations showed nearly an exact match with the field measurements. However, as expected, the 3D model needed more time and computer capacity to finish the calculation, whereas the 2D model required less effort to create the geometry and less calculation time. Due to the nature of a railway track – which is a 3D, the results of the 3D model showed better accuracy than those from the 2D model.

4.2 Three-dimensional modeling

4.2.1 FEM specification

Two models based on the geometry of the sites were created. The models were composed of rails, which were connected to the sleepers by a fastener system, with an elastic rail pad between them. Ballast surrounded the sleepers to help maintain the sleepers in their lateral and longitudinal positions. Sub-ballast and subgrade formed two other track layers, which were followed by the backfill and natural ground soil layers. However, simplification of complex geometries such as rails and sleepers was necessary to reduce the computation time and to minimize any errors due to the meshing of complex geometries. Therefore, the UIC60 rail was modified to a rectangular section (Figure 4.1) and dimensions were selected to maintain the properties of the original rail satisfactorily (Witt, 2008). The trapezium cross-section of the sleepers was also simplified to be rectangular.

All elements in the model (rail, railpad, ballast, etc.) were discretized using 3D solid elements. Contact areas were modeled as homogeneous and their properties did not change over time. Constitutive modeling of all components was considered as isotropic linear elastic material. The longitudinal length

of the model was 100 m and the cross-section length was 30 m. A total of 166 sleepers with a center-to-center distance of 0.6 m were placed along the rail, and the nodes at the bottom boundary were set to be fixed in every direction to simulate bedrock.

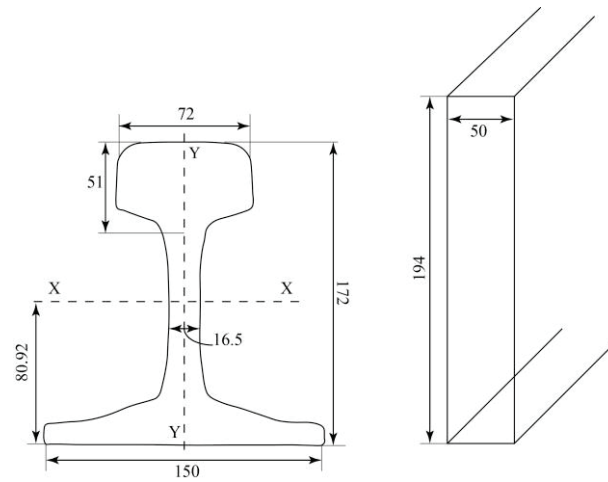


Figure 4.1 Cross-sectional detail of the actual rail and the rail modified to rectangular (mm), after Witt (2008)

The FEM uses volume discretization to solve the partial differential equations associated with wave propagation. For problems related to geotechnics, especially the subsoil, a discretized domain cannot extend to infinity due to computational constraints. Therefore, the model's geometry should be truncated. A shortcoming of this truncation is that it acts to reflect waves back into the modeling space, thus falsifying the solution. One approach is to place this boundary at a great distance from the solution space; however, this results in excessive computation requirements. Another solution is to use an absorbing boundary condition which simulates a condition in which the mesh boundary is located at infinity, by extrapolating from interior grid-points to the boundary grid-points.

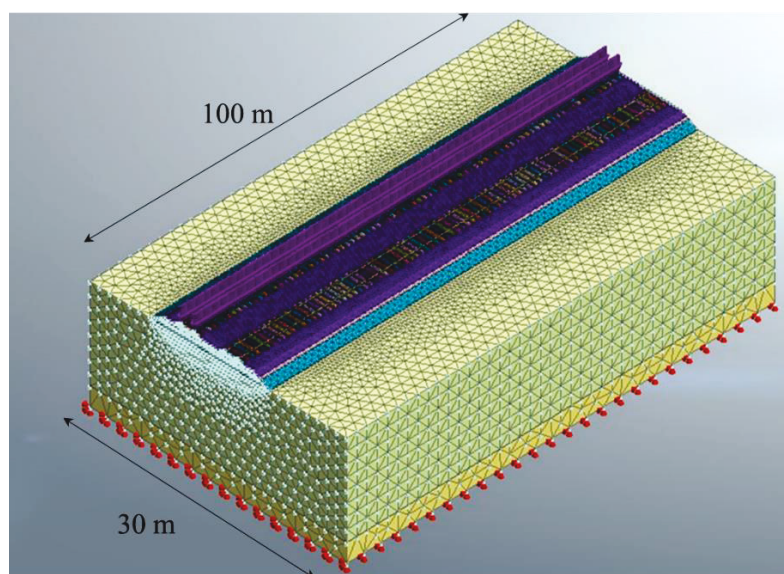


Figure 4.2. Mesh of the 3D model (Midas GTS NX)

The commercial FE codes used in this thesis have an in-built absorbing boundary condition that has been used to simulate infinite boundary conditions in all models (Figure 4.2).

Here, the material damping of the FE model was characterized by the mass and stiffness proportional coefficients, normally referred to as the Rayleigh damping. These coefficients are commonly used in dynamic analyses. The generalized equation for the Rayleigh damping is as follows:

$$[C] = \alpha[M] + \beta[K] \quad (4.1)$$

where $[C]$ is the damping matrix, $[M]$ is the mass matrix, and $[K]$ is the stiffness matrix. The parameters α and β are the mass and stiffness proportional damping coefficients, which are frequency-dependent. Their relation to the damping ratio ξ can be presented as follows:

$$\alpha + \beta\omega^2 = 2\omega, \text{ and } \omega = 2\pi f \quad (4.2)$$

Solving the equation for two different target frequencies and corresponding target damping ratios gives the required Rayleigh damping coefficients, shown as Equations 4.3 and 4.4.

$$\alpha = 2\omega_i\omega_j \frac{\omega_i\xi_j - \omega_j\xi_i}{\omega_i^2 - \omega_j^2} \quad (4.3)$$

$$\beta = 2 \frac{\omega_i\xi_j - \omega_j\xi_i}{\omega_i^2 - \omega_j^2} \quad (4.4)$$

where ω_i and ω_j are the natural frequencies of the first and second modes of the full model, for which the effective modal mass participation factors are high in the loading direction. Moreover, ξ_i and ξ_j are the hysteretic material damping ratios in the frequency range of interest. The natural frequency modes of the FE models are obtained by a separate eigenvalue analysis by Midas GTS NX, considering the subgrade reaction at the boundary of the layered material mesh before implementing the train load.

Another important factor in dynamic FE model analysis is the element size. For FE simulations it is recommended that element size should be at least 10 times smaller than wavelength. In this case, Equation 4.5 is applied:

$$10\Delta y = \frac{v_{\min}}{f_{\max}} \quad (4.5)$$

where v_{\min} is the minimum speed of waves, which can be approximated by the shear wave velocity.

4.2.2 Material properties

An isotropic linear elastic model is defined by the Young's modulus E and the Poisson's ratio ν . In the previous chapter, Table 3.1 and Table 3.4 presented the values of these physical properties and the mass density ρ of the various soil layers and elements. For the rail pad, usually the vertical stiffness is given rather than Young's modulus and Poisson's ratio. Here, rail pads with a Poisson ratio ν_{rp} equal to 0.25 and a vertical stiffness of $k_{rp} = 300$ kN/mm were considered. It was then possible to obtain an equivalent Young's modulus from Equation 4.6.

$$E_{rp} = k_{rp} \frac{\Delta h_{rp}}{A_{rp}} \cdot \frac{(1 + \nu_{rp})(1 - 2\nu_{rp})}{(1 - \nu_{rp})} \quad (4.6)$$

where the thickness of the rail pad is Δh_{rp} and the contact surface between the rail and the rail pad is represented as A_{rp} .

4.2.3 Loading procedure

Despite many types of commercial software having been introduced to geotechnical engineering, only a few (i.e. Midas GTS NX) are effective for solving railway geotechnical problems. To analyze the sites introduced in the last chapter, one of the main concerns was to generate the moving load; this can be achieved using two procedures. One is the frequency domain approach, which investigates the wheel response to a “moving irregularity”. The other one is the time domain analysis, which uses a numerical time interrogation process to investigate train-track dynamic properties. The Newmark integration method is an example (Dahlberg, 2004). In the literature, various methods are proposed for modeling the train load using FEM. In the case of linear elastic mechanical behavior, Hall (2002) modeled a full train load at the highest train speed, but to prevent errors arising at boundaries, only a point in the middle of the track was observed. Connolly et al. (2013) and Kouroussis et al. (2011) also used viscous boundaries with infinite elements.

In this study, a time domain approach was adopted, based on (Zhao et al., 2006, Kouroussis et al., 2009). All simulations were analyzed in the time domain using direct integration with implicit schemes. Generally, the train moving load was modeled in accordance with Jiang et al. (2014) and Araújo (2011). That is, the rail was connected to sleepers by rigid connection of the rail pads, and a single wheel load – the value of which changed over time – was located on each FE node above the rail. The loading procedure is schematically shown in Figure 4.3. The train moving loads were considered as triangular pulses distributed among three nodes, namely the main node and two adjacent nodes.

By way of explanation, the wheel load (F) on a certain node ($N+1$) gradually increased while the load moved from node N towards $N+1$. The load reaches the maximum value as the load arrives exactly above the node ($N+1$). Then, continuous reduction of the wheel load to zero at node $N+1$ begins as soon as the load moves towards node $N+2$. Consequently, the triangular pulse moves from one node to the next in a specific time interval, which is the distance between the nodes divided by the speed of the moving load. In this manner, a series of train wheels was considered to move along the track; however, the model simulates track-subsoil, and a vehicle-track model is not considered. The time step for simulating the moving loads was selected based on the Courant–Friedrichs–Lewy condition (Galavi and Brinkgreve, 2015), as shown in Equation 4.7.

$$C_n = \frac{\Delta t \cdot V}{L_{min}} \leq C_{max} \quad (4.7)$$

where Δt is time step and V is the train speed. The distance between two adjacent nodes is L_{min} . In this equation, C_n is called the Courant number, and the value of C_{max} changes with the method used to solve the discretized equation, which largely depends on whether the method is explicit or implicit. If an explicit solver is used, typically C_{max} is equal to 1, whereas implicit solvers are less sensitive to numerical instability and C_{max} can be greater than 1.

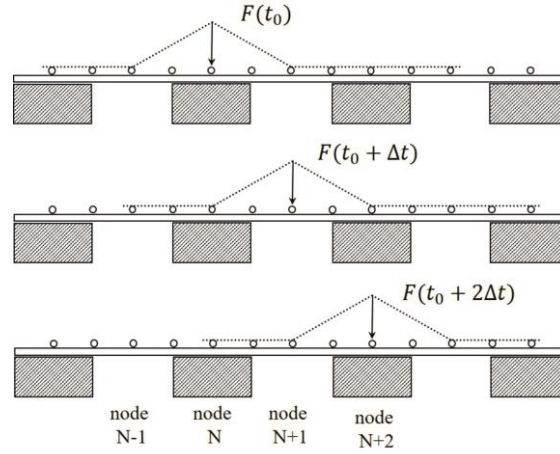


Figure 4.3 Modeling of the moving load (Araújo, 2011, Jiang et al., 2014)

4.2.4 Results

The results of the 3D FE models are presented in term of vertical velocity; to validate these results, they are compared with the field measurements. The first test site data (Section 3.2) were used to verify the model for the checkpoints that were located in the far-field regions and at different distances from the track (Figure 3.4). The second site data (Section 3.3) were used to verify the accuracy of the model for the checkpoints in different soil layers beneath the track (Figure 3.8).

Model validation of the first site

In the previous chapter (Sections 3.2.1), the geometry, soil properties, and train configurations for the first site were discussed; specifications for a 3D FE model have already been explained. The results of the 3D model were compared to the corresponding field measurements. Figure 4.4 shows the comparison of the numerical simulation with field data from the first site, under passage of a TGV train with a speed of 280 km/h. This figure indicates the accuracy of the model compared with the field data.

Figure 4.5 shows the results of the same site for the passage of a Thalys train at a speed of 299 km/h. Again, the results of the 3D model agreed well with the field data from four checkpoints. It may be concluded that the 3D model described and used in this study provides a trustworthy numerical model for predicting railway track behavior.

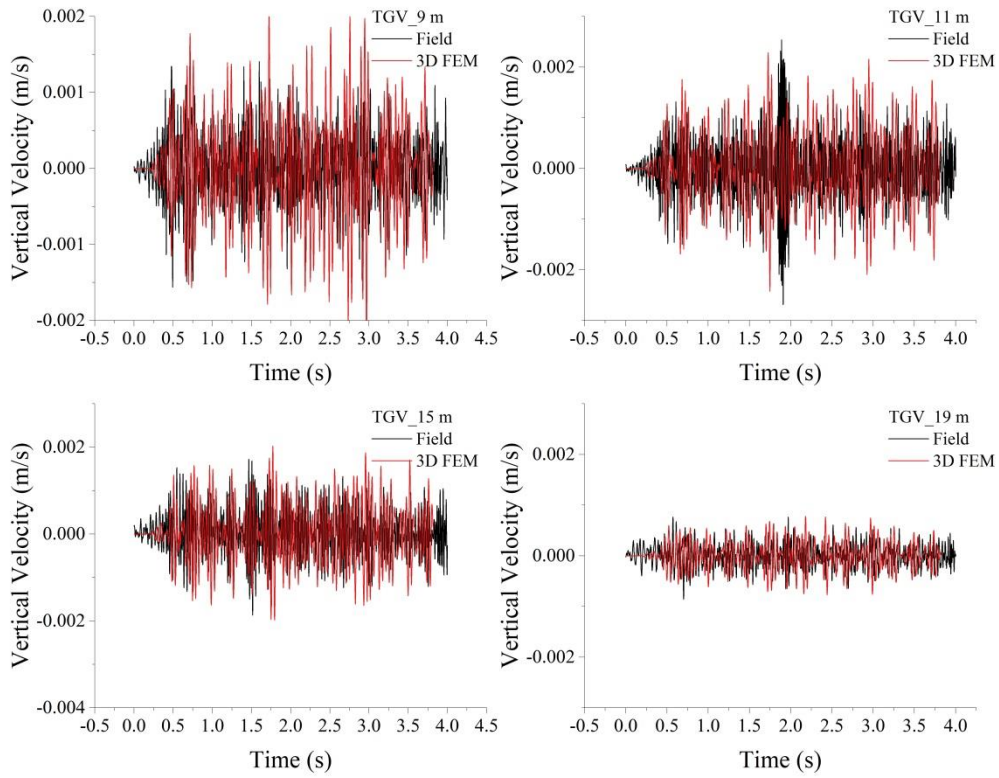


Figure 4.4 Results of 3D FE simulations for the first site under passage of TGV train at 280 km/h compare to field measurements, at various distances (9, 11, 15, and 19 m) from the nearest track.

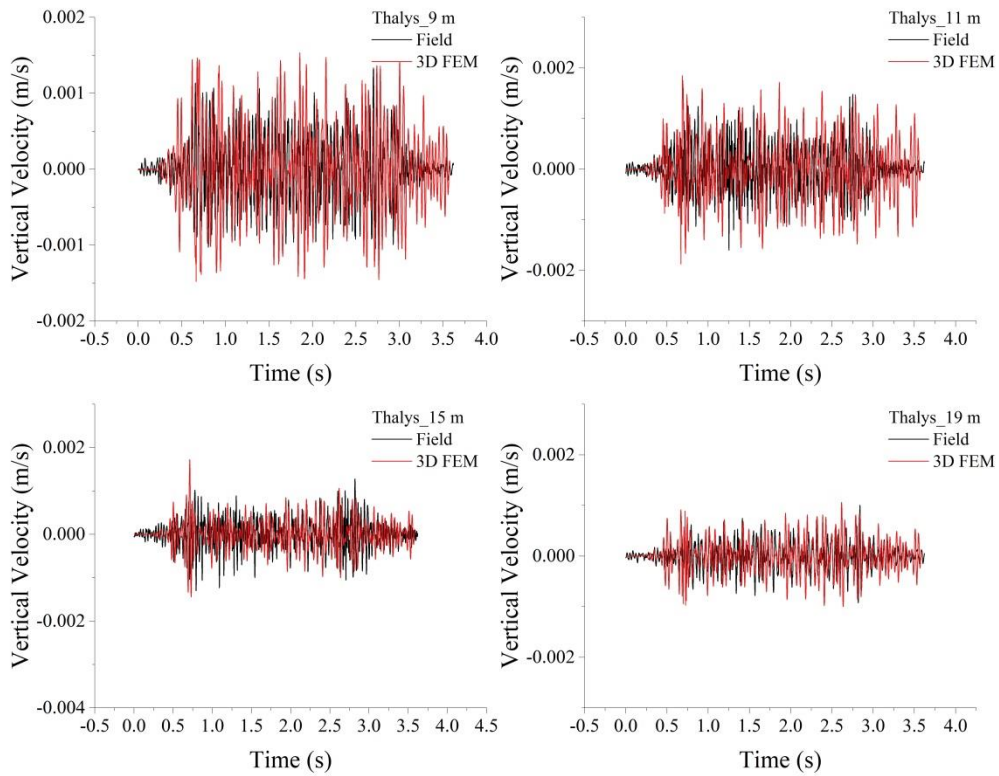


Figure 4.5 Results of 3D FE simulations for the first site under passage of Thalys train at 299 km/h compare to the field measurements, at various distances (9, 11, 15, and 19 m) from the nearest track.

Model validation of the second site

Details of the second site, including the track geometry and component properties, were described in the previous chapter (Section 3.3). Here, the results of a 3D model for vertical velocity and displacement from four checkpoints located at different depths are compared with the field measurements. The locations of the checkpoints – at depths of 0 m, 0.3 m, 2 m, and 4 m beneath the sleeper – are schematically shown in Figure 3.8. The results of the 3D FE model are presented in Figure 4.6 and Figure 4.7; these results show very good agreement with the measured vertical velocity from the second site. However, for the first checkpoint beneath the sleeper, less upward movement was predicted. The discrepancy might be a result of the defined connection between the sleeper and ballast beneath it, as well as the rigid connection of the rail to the sleeper by a rail pad.

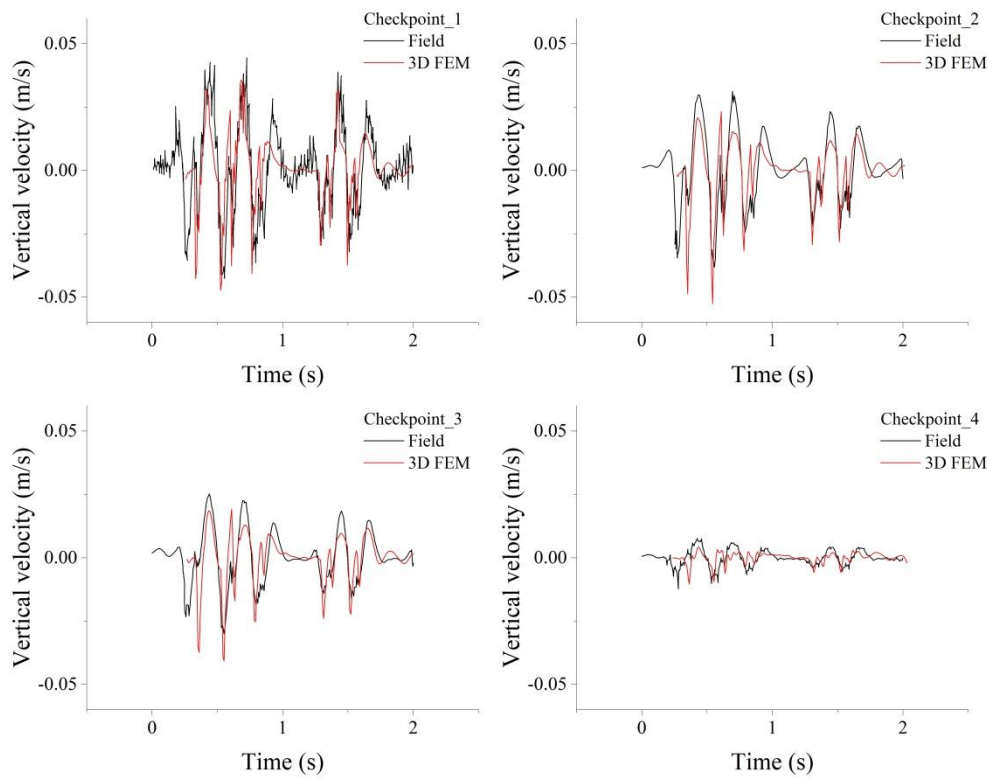


Figure 4.6 Vertical velocity from 3D FE model compared with field data from the second site (depths of 0, 0.3, 2, and 4 m beneath the sleeper).

To conclude, the 3D FE model with acceptable accuracy predicts the ground vibration, but its use is costly and time-consuming. In this study, 3D models were used as a powerful tool for further analysis to verify the 2D FE model where no field data were available.

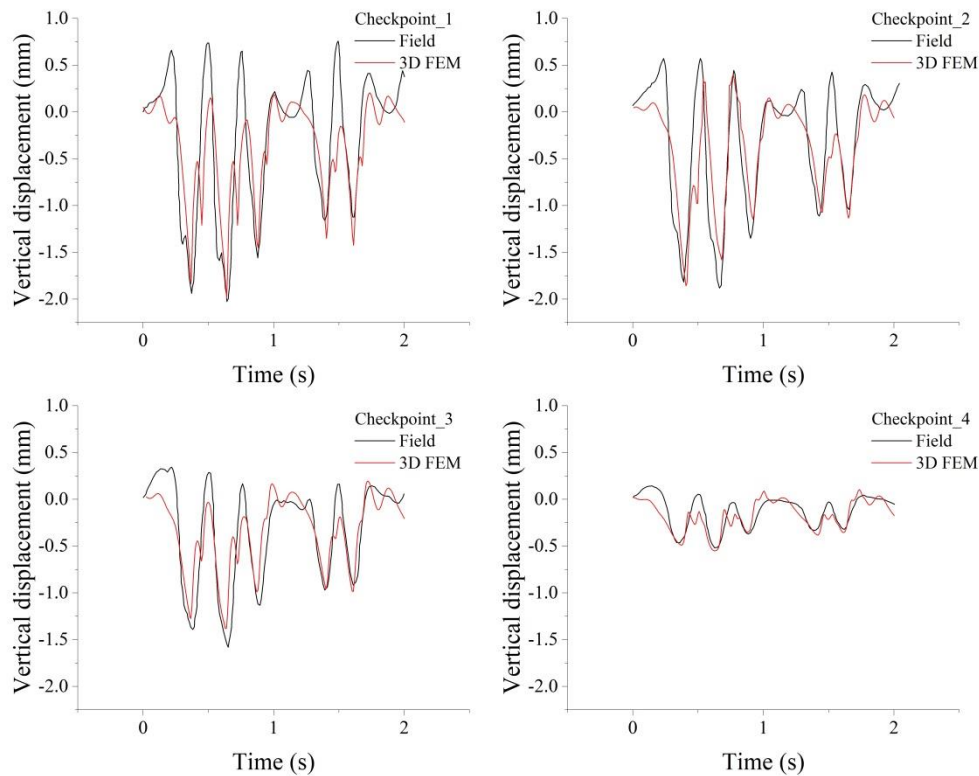


Figure 4.7 Displacement of 3D FE model compared with field data from the second site (depths of 0, 0.3, 2, and 4 m beneath the sleeper).

4.3 Two-dimensional modeling

4.3.1 Background

A railway track is a fully 3D problem, but complete 3D analysis by considering the material properties rather than linear elastics (including the subgrade) is costly. Many researchers have tried to propose a suitable approach to apply a 2D calculation. Depending on the problem, either relatively simple 2D design models or developed models with many equations can be used. Railway track operations can be described in terms of strain rather than the motion of solids, which is applicable for rolling stock. Often, models based on the theory of elasticity are used to describe the railway track through numerical simulation.

A railway track problem represents an interaction between the train and soil body, but combining different approaches to solve a model leads to great complexity in generating the model. In many cases and especially in studies on the soil body alone, the use of such complex models is unreasonable. Therefore, many researchers have considered the track as a system of different bodies or layers, with elastic strain under the load. These models are quasi-static. To create such models, one of the main conditions is an assumption of instant and full constant volume (during static load) delivery of the strain caused by the applied load. Normally, to consider the dynamic action of the load, a magnification factor is applied to its static value.

Hall (2000) created an axisymmetric model to simulate train-induced ground vibrations, based on the beam on Winkler foundation method. Hall concluded that calculation of a railway track according to the Winkler model, under stationary excitation of loading on the soft ground in Ledsgard in Sweden, yielded good agreement with measured data. Here, the model consisted of a track dynamic model for determining stationary excitation, and a plane-strain FE model to simulate the effect of the load in the lower soil layers. The bottom layer in the FE model is bedrock, and the time history of the vertical stress obtained from quasi-dynamic analysis is used as an input for FE modeling in PLAXIS.

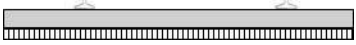




4.3.2 Superstructure

The Winkler model of the beam on elastic foundation was modified by Zimmermann to be applicable for railway tracks. Later, Eisenmann overcame certain limitations of earlier models. The idea of this method is to transform the single supported beam by converting the bearing area into a continuously supported beam. The substructure and ground are modeled by the spring and damper, based on the comprehensive guidelines by Frýba (1999). In this approach the moving train load is modeled as a stationary but time-dependent load. The axle loads of the corresponding cars and bogies can be considered realistically. However, the dynamic effect of the adjacent axle loads for high-speed trains cannot be neglected and is represented as factor α in Equation 4.8 (Adam and Kopf, 2003). For static conditions, α is equal to zero, and in the worst case (which is resonance) it is equal to 1.

$$\alpha = \frac{v_{\text{train}}}{v_{\text{critical}}} \quad (4.8)$$

Different pressure distributions between the sleeper and ballast are highly important in the modeling, and are identified based on the track service time. In a freshly tamped track, pressure transferred from sleeper to ballast is concentrated below each rail seat. After a long service time, the pressure tends to have a uniform distribution. This condition is associated with a gap between the sleeper and the ballast surface below the rail seat. The most accepted contact pressure distribution patterns between sleeper and ballast are presented in Table 4.1.

Table 4.1 Contact pressure distribution patterns (after Sadeghi and Barati, 2010)

Description	Pressure distribution
Uniform pressure	
Principal bearing on rails	
Tamped either side of rail	
Maximum intensity in middle	
Laboratory test	

The uniform pressures under the sleepers distribute along certain portions of the sleeper length. This length is called “effective length” and is represented as l_a . Several models have been proposed for the

contact pressure distribution patterns under sleepers; the most applicable ones are shown in Table 4.2. The sleeper length is denoted as l_s .

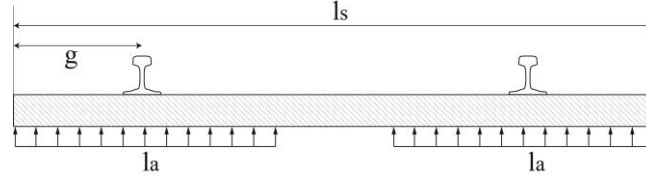


Figure 4.8 Simplified effective length of sleeper

Table 4.2 Effective length (area) of sleeper support at rail seat (Sadeghi and Barati, 2010)

AREMA	A_e = two-thirds of sleeper area at its bottom surface
UIC	A_e = 6000 cm ² for l_s = 2.5 m A_e = 7000 cm ² for l_s = 2.6 m
Australia	$2l_a = l_s - g$, for bending moment calculation at rail seat $2l_a = 0.9(l_s - g)$, for bending moment calculation at sleeper center
Clarke	$2l_a = (l_s - g) \left[1 - \frac{l_s - g}{125t^{0.75}} \right]$, t is the sleeper height
Simplified, German	$2l_a = l_s - 0.5$

In this thesis, the simplified German equation for finding the effective length is used. The effective area under each sleeper side is calculated by multiplying the effective length to the sleeper's width b_s .

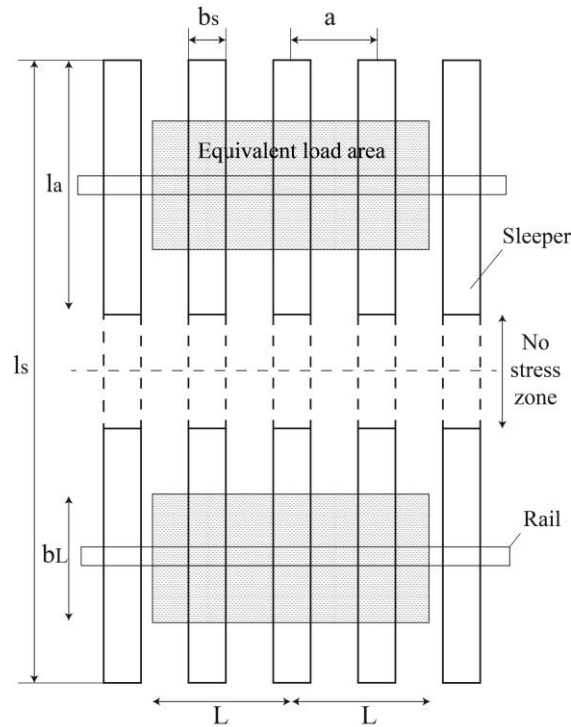


Figure 4.9 Conversion of discrete supports to continuous support

However, to satisfy the Winkler model for a continuum length, the cross sleepers are transposed into two fictitious longitudinal sleepers, one under each rail; the idea is that per unit length of track, the area giving support to the load should be the same after the transition to longitudinal sleepers. An equal area for the longitudinal beam should be created by dividing the effective area by the sleeper distance a , which results in an ideal strip width, b_L . Figure 4.9 illustrates the conversion of discrete supported sleepers to a continuous supported area

$$A_e = l_a \cdot b_s \quad (4.9)$$

$$b_L = \frac{A_e}{a} \quad (4.10)$$

Clearly, axle load is associated with the longitudinal beam with a width of $2b_L$, and a wheel is related to the width of b_L . Using all the formulations in Section 2.5 and the mechanical model of the dynamic load Fryba (1999), the vertical stress can be obtained from Equations 4.11 and 4.12.

$$p(x) = \frac{Q}{2b_L \cdot L} \cdot \left\{ \frac{2}{a_1(D_1^2 + D_2^2)} e^{-a_0 \frac{x}{L}} \cdot \left[D_1 \cos\left(a_1 \cdot \frac{x}{L}\right) + D_2 \sin\left(a_1 \cdot \frac{x}{L}\right) \right] \right\} \text{ for } x \geq 0 \quad (4.11)$$

$$p(x) = \frac{Q}{2b_L \cdot L} \cdot \left\{ \frac{2}{a_1(D_3^2 + D_4^2)} e^{-a_0 \frac{x}{L}} \cdot \left[D_3 \cos\left(a_4 \cdot \frac{x}{L}\right) - D_4 \sin\left(a_2 \cdot \frac{x}{L}\right) \right] \right\} \text{ for } x < 0 \quad (4.12)$$

where x is the longitudinal distance from the wheel load, and L is the characteristic length or the elastic length. The L term is computed as follows:

$$L = \sqrt[4]{\frac{4E \cdot I}{b_L \cdot c_t}} \quad (4.13)$$

where E is Young's modulus and I is the moment of inertia of one rail. Equation 4.14 represents the total track modulus c_t , which consists of the moduli of reaction for the pad c_p , sleeper c_s , and substructure c_{soil} , respectively.

$$\frac{1}{c_t} = \frac{1}{c_p} + \frac{1}{c_s} + \frac{1}{c_{soil}} \quad (4.14)$$

The terms D_1 , D_2 , D_3 and D_4 are dynamic magnification factors for the vertical deflection at the point underneath the moving load. The values are obtained as follows (Wegener, 2012):

$$D_1 = a_0 \cdot a_1 \quad (4.15)$$

$$D_2 = a_0^2 - 0.25(a_1^2 + a_2^2) \quad (4.16)$$

$$D_3 = a_0 \cdot a_2 \quad (4.17)$$

$$D_4 = a_0^2 + 0.25(a_1^2 + a_2^2) \quad (4.18)$$

where in practical railway construction for a light damping situation, $\beta < 1$ when $\alpha < 1$. Therefore, approximate solutions to calculate factors a_0 , a_1 and a_2 are as follows:

$$a_0 = \sqrt{1 - \alpha^2} \quad (4.19)$$

$$a_{1,2} = \sqrt{1 + \alpha^2 \pm \frac{2\alpha \cdot \beta}{\sqrt{1 - \alpha^2}}} \quad (4.20)$$

The α term was introduced earlier (Equation 4.8). The damping factor is the ratio of actual damping c to critical damping $c_{critical}$, as shown in Equations 4.21 to 4.23.

$$\beta = \frac{c}{c_{critical}} \quad (4.21)$$

$$c_{critical} = 2m \cdot \omega \quad (4.22)$$

$$\omega = \sqrt{\frac{k}{m}} \quad (4.23)$$

The resonance speed for a common superstructure, constructed of rails (UIC60) and sleepers (B70) with a distance of 60 cm, is between 800 km/h and 1300 km/h. The lower boundary indicates very soft ground with a characteristic length around 1.3 m, and the upper boundary suggests a relatively rigid ground and a characteristic length of 0.8 m. The superstructure resonance speed is always higher than the train speed. However, many site investigations have revealed that trains theoretically may show another lower critical speed when reaching the Rayleigh wave velocity of the ground. For instance, Ledsgard track in Sweden has been studied by many researchers (Madshus and Kaynia, 2000, Picoux and Le Houédec, 2005) for passage of X2000 trains with different speeds, and this problem has been extensively addressed. Madshus and Kaynia (2000) stated that a condition similar to resonance could occur when a moving linear point-load reaches Rayleigh wave speed, and the rail and embankment system behaves as a beam in dynamic interaction with the ground. They suggested that beams on a homogeneous half-space should have two critical speeds, one equal to the Rayleigh wave velocity of the ground, and the other related to the bending stiffness and mass of the rail together with the ground properties. For that reason, the average Rayleigh wave velocity, calculated according to Equation 4.24, was considered to be the critical velocity in Equation 4.8.

$$v_{Rayleigh} = \left(\frac{0.87 + 1.17\nu}{1 + \nu} \right) \sqrt{\frac{G}{\rho}} \quad (4.24)$$

where ν is the Poisson's ratio, and ρ and G are density and shear modulus, respectively. There is no constant Rayleigh or shear wave velocity; these wave velocities depend on type of soil, stress level and amplitude. The average velocity for the system should be estimated by average wave velocities in all layers, using the cone model for the substructure.

4.3.3 Substructure

The substructure and natural ground beneath the ballast were modeled based on the cone theory of Wolf and Deeks (2004) and Wolf (1994). For the mechanical modeling of the track, it is assumed that the soft bending superstructure is elastically embedded. The viscoelastic behavior of the layered structure is

described by a related unit length spring stiffness $k \left(\frac{\text{kN}}{\text{m}^2} \right)$, as well as damping parameters $c \left(\frac{\text{Ns}}{\text{m}^2} \right)$. For a railway track, rails act as flexural beams with the bending resistance EI , which are laid on individual sleepers in addition to inertia forces that occur due to the masses of rails and sleepers. Therefore, the masses of the sleepers' equivalent are converted to a beam.

The basic idea of the cone theory is to ignore that portion of the soil which has little effect on the deformation of the observed material. The model is constructed for reasonable approximation of physical phenomena using simplified mathematical formulations. In the first step, the load transfer surface of the half sleeper, with a length of $2a$ and width of $2b$, on the surface of the layered structure is converted to an equal circular area. The circle's radius is $r = 2\sqrt{a \cdot b/\pi}$. At depth, it forms a truncated cone which is layered at the top surface and is a half-space at the bottom. To construct the cone, the opening angle, which is the ratio of $\frac{z_{cp}}{r_0}$, should be calculated. For the bottom (semi-infinite) layer with the stiffness modulus E_{S0} and the density ρ_0 , the top surface is $A_0 = 4a_0 \cdot b_0$, with the equivalent radius $r_0 = 2\sqrt{a_0 \cdot b_0/\pi}$.

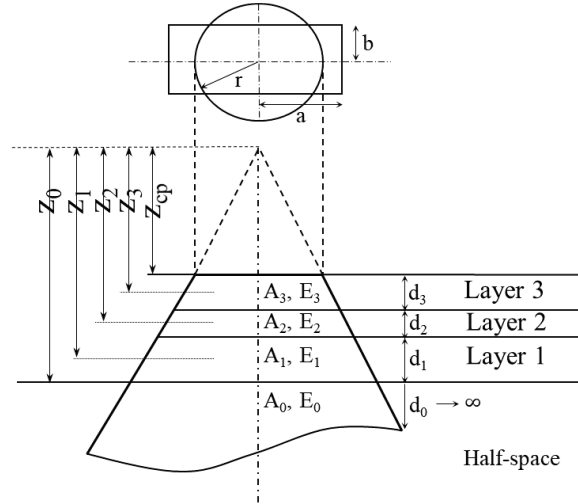


Figure 4.10 Cone model (after Adam and Kopf, 2003)

The cone can be calculated according to the beam theory as a semi-infinite bar, with a square and variable cross-sectional area. For the dynamic case, inertial forces are considered and the equilibrium of momentum leads to a one-dimensional wave equation. Taking into account the boundary condition that the displacement of the surface value (z_0) corresponds to the action of the force $F_0 = 0$ at infinity leads to the equation of motion for the homogeneous elastic cone. This is shown as Equation 4.25 below (Wolf, 1994). The constant coefficients of the spring stiffness K_0 and the dashpot C_0 , for the geometric attenuation (radiation attenuation) are calculated from Equation 4.26 and 4.27.

$$F_0(t) = K_0 \cdot z_0(t) + C_0 \cdot \dot{z}_0(t), \text{ and } \dot{z}_0 = \frac{dz_0(t)}{dt} \quad (4.25)$$

$$K_0 = \frac{E_{S0} \cdot A_0}{z_0} \quad (4.26)$$

$$C_0 = A_0 \cdot \sqrt{\rho_0 \cdot E_{S0}} \quad (4.27)$$

The peak height of an homogeneous cone z_0 is obtained on the surface by comparing the stiffness of the cone, K_0 , with the static stiffness of the surface foundation on homogeneous half-space in case of vertical translation for rectangular loading K_R (Wolf, 1994).

$$K_R = \frac{E_{S0} \cdot b_0}{2} \frac{1 - 2\nu}{(1 - \nu)^2} \left[3.1 \left(\frac{a_0}{b_0} \right)^{0.75} + 1.6 \right] \quad (4.28)$$

By equalizing Equations 4.26 and 4.28, the center height of the cone can be determined by Equation 4.29.

$$z_0 = 8a_0 \frac{(1 - \nu)^2}{1 - 2\nu} \left[3.1 \left(\frac{a_0}{b_0} \right)^{0.75} + 1.6 \right]^{-1} \quad (4.29)$$

The homogeneous cone superposed action for overlaid strata is considered in the next step. It is assumed that Poisson's ratio ν in the entire layer is constant. The error of the approximation is low and can be neglected. Thus, the peak height of the layered cone may be defined exactly below the sleeper, similar to Equation 4.30, where $2l_a = a_{hs}$ and $2b_s = b_{hs}$.

$$z_{cp} = 8a_{hs} \frac{(1 - \nu)^2}{1 - 2\nu} \left[3.1 \left(\frac{a_{hs}}{b_{hs}} \right)^{0.75} + 1.6 \right]^{-1} \quad (4.30)$$

The stiffness K_i of each layer i with a thicknesses of d_i and stiffness modulus E_s result in the underlying linear elastic behavior of the cone, shown in Equation 4.31. The size of the area A_i is determined using Thales theorem, as shown in Equations 4.32 to 4.34.

$$K_i = \frac{A_i \cdot E_{Si}}{d_i} \quad (4.31)$$

$$A_i = z_i^2 \frac{4a \cdot b}{z_{cp}^2} \quad (4.32)$$

$$z_0 = z_{cp} + \sum_{i=1}^n d_i \quad (4.33)$$

$$z_i = z_{cp} + \frac{d_i}{2} + d_{i+1} + \dots + d_n, i = 1 \dots n \quad (4.34)$$

The total spring stiffness K of layered soils below the sleeper is obtained by serial arrangement of the individual spring stiffness, depicted as Equation 4.35. This allows the average stiffness modulus of all layers to be calculated by Equation 4.36

$$K = \frac{1}{\frac{z_0}{E_{S0} \cdot A_0} + \sum_{i=1}^n \frac{d_i}{E_{Si} \cdot A_i}} \quad (4.35)$$

$$E_s = \frac{2K(1 - \nu)^2}{b} \frac{1 - 2\nu}{1 - 2\nu} \left[3.1 \left(\frac{a}{b} \right)^{0.75} + 1.6 \right]^{-1} \quad (4.36)$$

Equation 4.37 can be used to determine the damping C of the layered cone. The required average value of density and the Poisson's ratio for the layered substructure can be calculated from Equations 4.38 and 4.39, which comprise the known parameters of each layer i .

$$\text{Damping:} \quad C = 4a \cdot b \sqrt{\rho_a \cdot E_s} \quad (4.37)$$

$$\text{Density:} \quad \rho_a = \frac{\sum_{i=0}^n \rho_i \frac{z_i}{A_i}}{\sum_{i=0}^n \frac{d_i}{A_i}} \quad (4.38)$$

$$\text{Poisson's ratio} \quad \nu_a = \frac{\sum_{i=0}^n \nu_i \frac{z_i}{A_i}}{\sum_{i=0}^n \frac{d_i}{A_i}} \quad (4.39)$$

Finally, the unit length spring stiffness k and the unit length damping parameter c are obtained from dividing the total spring stiffness and viscous damper of the layered cone by the sleeper distance. It should be noted that the effects of reflections and refractions of waves at the layer boundaries cannot be considered in this model. Nonetheless, no large difference exist between the stiffness of layers, and the approximation is sufficiently accurate (Wolf, 1994).

4.3.4 Sample calculation for the second site

Details of the geometry and elements of a track were explained in Section 3.3. Table 4.3 presents a list of those details and all calculated parameters that were used as the input for calculations in previous sections. It should be noted that similar calculations have been performed for the first site.

Table 4.3 Available input data based on the data from second site

Axle load	P	215 and 130 kN
Sleeper length	l_s	2.6 m
Sleeper width	b_s	0.27 m
Sleeper distance	a	0.6 m
Effective length	l_a	1.05 m
Ideal strip width	b_L	0.47425 m
Mass of rail	m_r	60.34 kg/m
Mass of sleeper	m_s	305 kg
Characteristic length	L	1.059 m
Total track modulus	C_t	4.30 e+04 kN/m ²
Train speed	v_{train}	130 km/h
Young's modulus of rail	E_r	2.10 e+08 kN/m ²
Moment of inertia of rail	I_r	3.06 e-05 m ⁴

In the first step, the Thales theorem was applied and the related area of each layer was obtained. The properties of substructure layers (thickness, density, and calculated area) are shown in Table 4.4.

Table 4.4 Basic calculations for Cone

	Poisson's ratio	Density (kg/m ³)	Thickness (m)	z_i (m)	A_i (m ²)	E_s (MPa)
Ballast	0.30	1750	0.4	0.81	0.50	241
Sub-ballast	0.30	2200	0.5	1.26	1.22	390
Subgrade	0.40	2000	0.5	1.76	2.38	95
Backfill	0.45	1730	1.5	2.76	5.85	61
Soil layer 1	0.47	1030	3.1	5.06	19.66	22
Soil layer 2	0.485	2080	-	6.61	33.56	200

In the next step, the average properties of all layers were calculated – namely average density, Poisson's ratio, and stiffness modulus. Using the formulas introduced earlier in this thesis, all other required data were calculated. The results are listed in Table 4.5.

Table 4.5 Obtained results for the substructure calculations

Half of the sleeper width	b_{hs}	0.1355 m
Half of the effective length	a_{hs}	0.525 m
Peak height of the cone from the last layer	z_0	6.609 m
Peak height of the cone from surface	z_{cp}	0.609 m
Effective length	l_a	1.05 m
Average density	ρ_a	1841 kg/m ³
Average Poisson's ratio	ν_a	0.36
Average stiffness modulus	E_s	85.5 MPa
Total spring stiffness of series of layers	K	4.00 e+04 kN/m
Unit length spring stiffness	k	6.66 e+04 kN/m ²
Rayleigh wave speed	$V_{Rayleigh}$	338.3 km/h
Factor of the dynamic effect of the adjacent axle	α	$0.384 < 1$
Damping factor	β	$0.650 < 1$

The dynamic magnification factors were calculated based on Equations 4.15 to 4.20. The results are presented in Table 4.6.

Table 4.6 Dynamic magnification factors

a_0	a_1	a_2	D_1	D_2	D_3	D_4
0.923	1.299	0.779	1.200	0.580	0.720	1.120

Finally, using Equations 4.11 and 4.12, the time history of vertical stress was obtained. As shown in Figure 4.11, the first four axles were the heaviest and belonged to the locomotive; these axles resulted in higher pressure. The passenger cars had lower axle loads and resulted in lower pressure between the ballast and sleepers. Moreover, pressure in the spaces between two bogies decreased to nearly zero, whereas in the spaces between two adjacent wheels not much reduction was noted due to rapid re-loading.

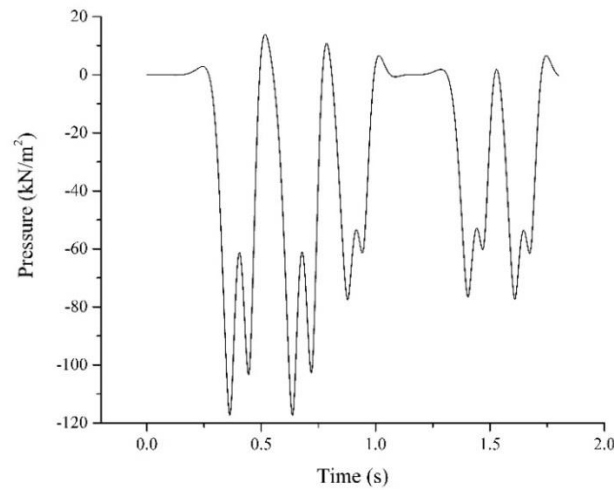


Figure 4.11 Pressure under sleeper on ballast

4.3.5 Results

Pressure between the sleeper and the ballast, for each of the tracks and corresponding trains, was calculated. The results were implemented as an input loading condition in the FE software, PLAXIS 2D, and the results of FE calculation were compared with the measurements in terms of vertical velocity.

The results of 2D FEM plane strain calculations for the first site, under passage of TGV and Thalys trains, are presented in Figure 4.12 and Figure 4.13. The 2D FEM results for the second site in comparison to the measurement are shown in Figure 4.14.

The accuracy of the 2D model, given the reasonable calculation time, was acceptable. However, as was the case for 3D modeling, for the first checkpoint a lower vertical velocity was obtained. The other three checkpoints showed an almost perfect match.

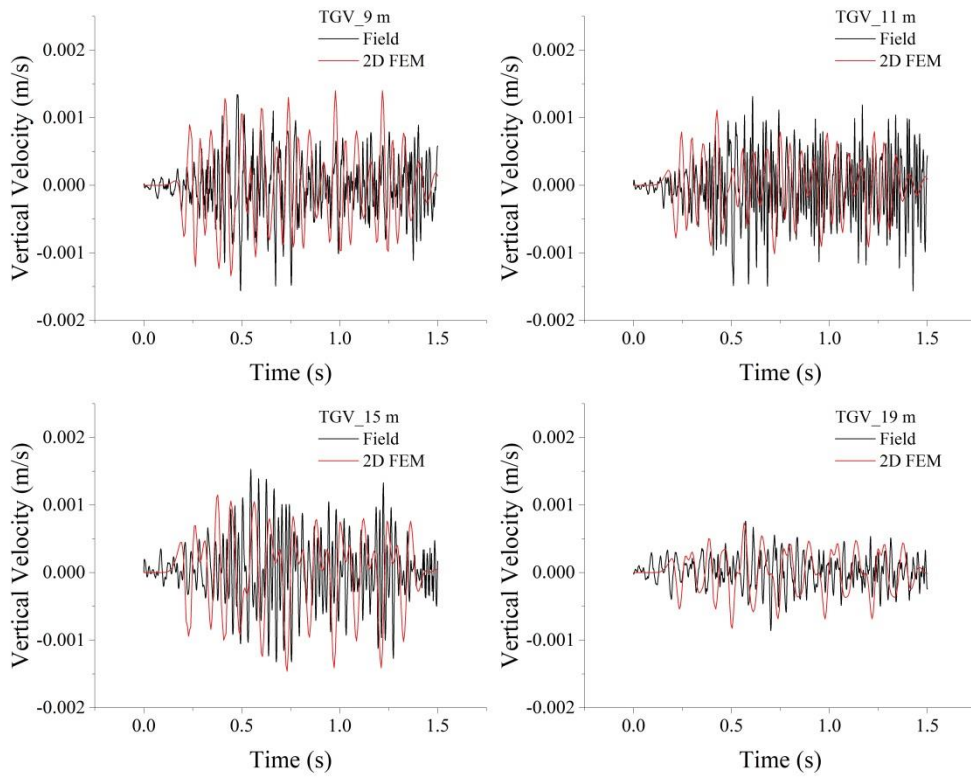


Figure 4.12 Numerical results of 2D FEM for 1st site under passage of TGV train at 280 km/h, at various distances (9, 11, 15, and 19 m) from the nearest track.

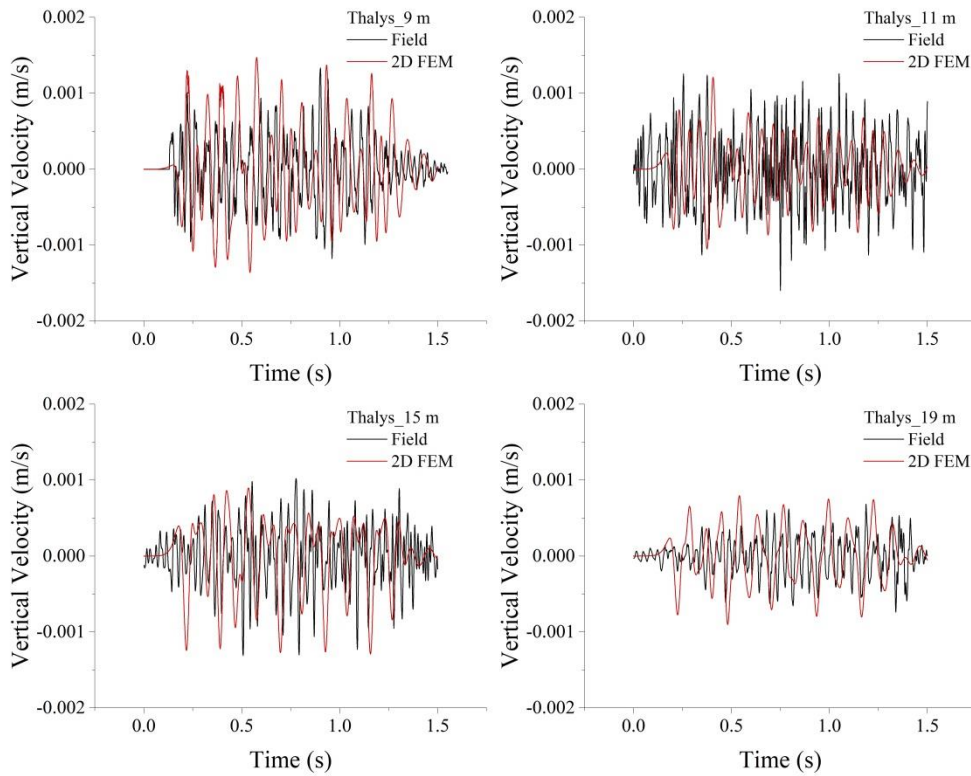


Figure 4.13 Numerical results of 2D FEM for 1st site under passage of Thalys train at 299 km/h, at various distances (9, 11, 15, and 19 m) from the nearest track.

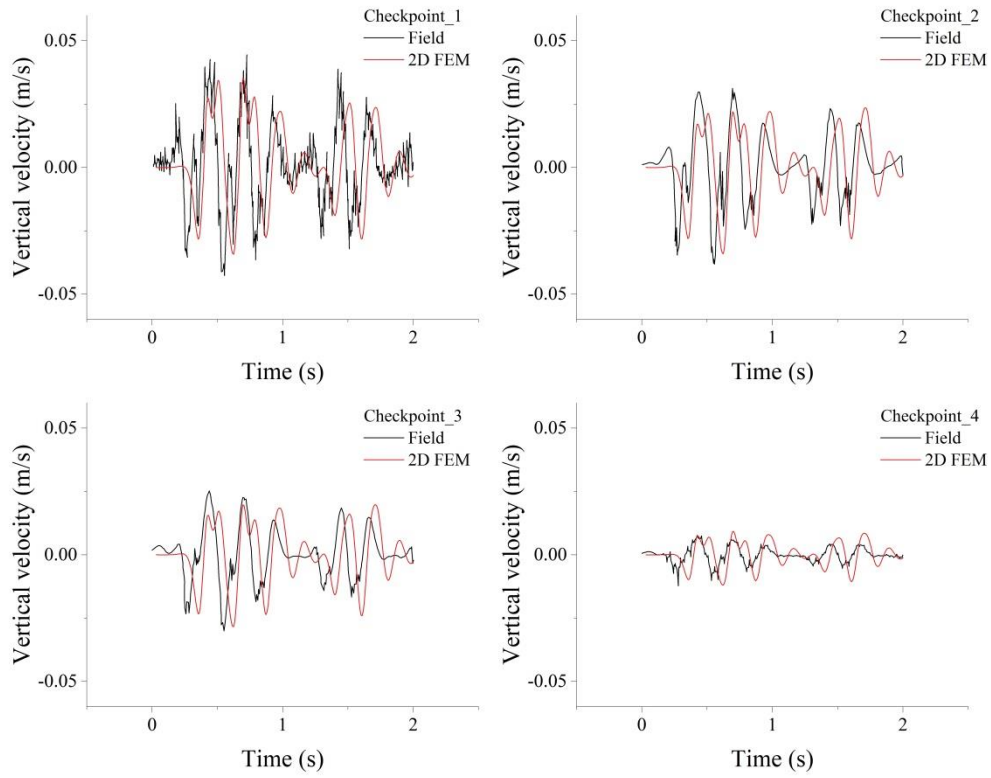


Figure 4.14 Vertical velocity obtained from 2D FE model in four checkpoints at the second site, at various depths (0, 0.3, 2, and 4 m) beneath the sleepers.

5 Stone Column Numerical Simulation

5.1 Introduction

The focus of this chapter is the numerical study of the stone columns (end-bearing and short), using either plastic or consolidation calculations. A comprehensive discussion of the influential parameters in the calculations is also provided. To conduct these studies, two types of simulations are considered. One models the stone column as an axisymmetric problem with a unit cell, and the other is based on plane strain conditions. Thereafter, the influence of column patterns and spacing on the deformation of a railway track due to the train load is investigated by considering the dynamic impact factor.

5.2 Unit cell approach

5.2.1 General study

In this section, an attempt is made to analyze the behavior of a stone column as a unit cell in the axisymmetric condition under a consolidation process. The basic assumption of the unit cell approach is that columns are located in constant spaces and subjected to a uniform load, and all columns can be expected to show the same behavior. Hence, analyzing one column and its influence on the surrounding soil is sufficient, as its behavior can be extrapolated to other columns. Because of the symmetry of the problem, the shear stresses along the border of the unit cell are assumed to be zero.

Here, a unit cell model is constructed based on the work of Tan et al. (2008). The geometry of the axisymmetric model is shown in Figure 5.1. The model has a height of 10 m, with a width R of 1.275 m, which presents the radius of the influence area for a column with the diameter ($2r_c$) of 0.85 m. The standard boundary conditions including fully fixed at the bottom and horizontally fixed on the vertical sides are implemented in the model.

The input parameters for the Mohr–Coulomb (MC) model are stiffness modulus E , cohesion c , internal friction angle φ , Poisson's ratio ν , and unit weight γ . The material parameters for the soft soil and stone column are presented in Table 5.1. For the stone column, it is recommended that the elastic modulus of the stone column should be between 10 to 40 times higher than that of the soil material; this ratio is called the modular ratio, m . The elastic modulus of a material is chosen to fulfill this criterion, and the permeability of the column material is assumed to be 10000 times higher than of that soft soil (Ng and Tan, 2014).

Table 5.1 Material properties for unit cell models

	Type	E (kPa)	ν (-)	φ (deg)	c (kPa)	γ_{sat} (kN/m ³)
Soft soil	Undrained	5000	0.30	21	5.0	19
Stone column	Drained	50000	0.30	40	0.1	19

The instantaneous uniform vertical load of 100 kPa was applied at the top of the model through a rigid plate to ensure that the soil and column experienced equal vertical strain. To simulate the consolidation condition, the top boundary was set to open for drainage purposes, and the phreatic level was placed at the top surface to generate pore water for the model. Simulation of the consolidation process continued until the excess pore water pressure dissipated to less than 0.01 kPa.

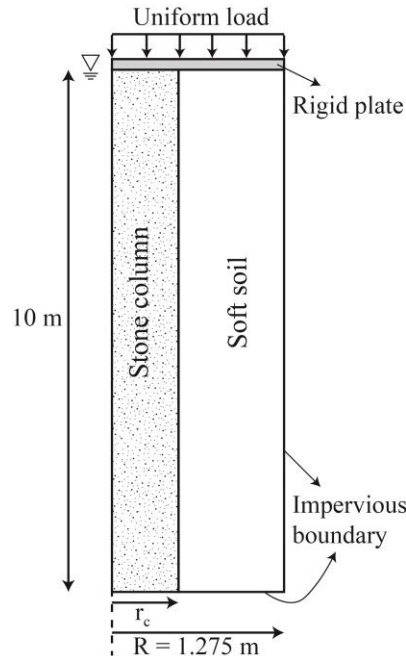


Figure 5.1 Axisymmetric unit cell model (after Tan et al., 2008)

Initial stresses were generated with the K_0 procedure, and the coefficient of consolidation c_v was determined by the software. To study the effect of stone column lengths, all parameters and conditions were held constant while the length of the implemented column was varied to either 10 m, 7 m, 5 m, 3 m, or 0 m. A length of 10 m indicated a fully penetrated column (i.e. end bearing condition) and 0 m implied no existence of a column in the model. To compare the influence of column length on either surface settlement or excess pore water pressure, two check points were considered in the model. One was located at the top of the model to check the settlement; the other was placed at the bottom, far from the column, representing the worst-case scenario for dissipating the excess pore water pressure. Figure 5.2 shows the time history of the excess pore water pressure and the settlement for five different models. The shorter dissipation time for excess pore water pressure and less settlement were attained as stone column length was increased. The results also showed that even the short stone column had no much benefit in terms of decreasing the consolidation time compared with the no-column condition in the model, but minor improvement occurred in the settlement results.

To investigate the usefulness of short stone columns for dissipating excess pore water pressure and shortening the consolidation time, the results of variation of excess pore pressure for different length in the period of one week, and three weeks in depth of 5 m, are shown in Figure 5.3. The rapid reduction in excess pore water pressure within a week, for columns higher than 5 m, was evidently due to the existence of a shorter path for drainage. The shortest column had little impact in the first week but

showed a great influence in terms of reducing the pressure within 3 weeks, compared with the case without a column. For the 5-m column, an immediate drop in excess pore water pressure in the toe of the column was observed, where the soft soil still experienced much higher pressure.

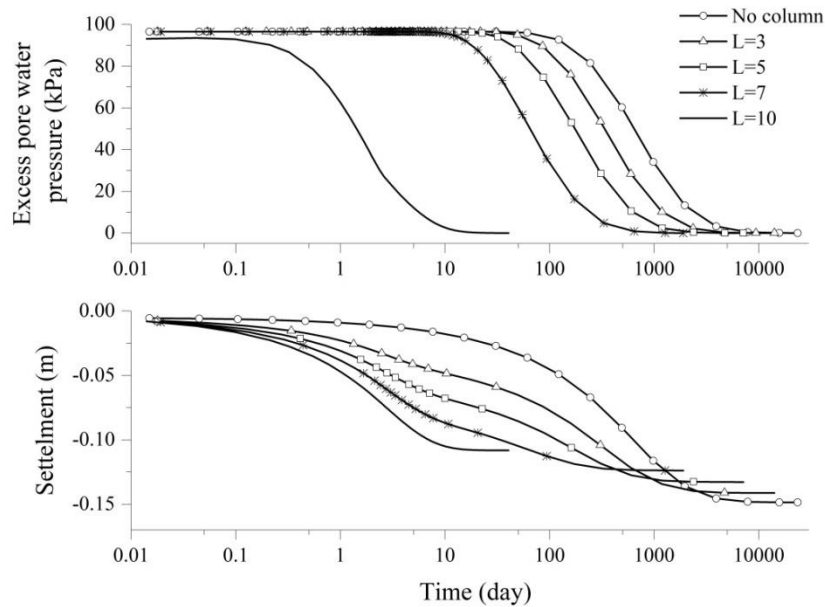


Figure 5.2 Effect of stone column length on excess pore water pressure and settlement

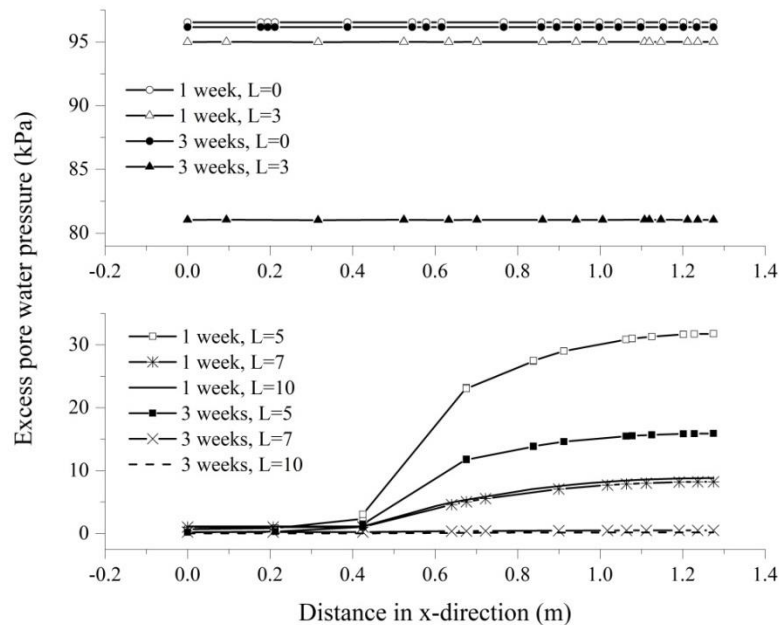


Figure 5.3 Change in excess pore water pressure after 1 and 3 weeks for different lengths of stone columns at a depth of 5 m, in an x-direction (from the outer boundary of the columns to outer boundary of the soil).

Clearly the application of stone columns having even a short length can effectively improve the behavior of soft soil in geotechnical problems. In the next section, the effect of important parameters in stone column applications are studied, to gain a better understanding of which materials and geometry were most suitable for the columns.

5.2.2 Parametric study

The effects of changing the area of replacement and the material properties, including the friction angle of column materials, loading intensity, and the modulus ratio of columns, were investigated. For each parameter a series of values in an applicable range was chosen. The behavior of the material was studied by varying each parameter and evaluating the settlement improvement factor, as shown in Equation 5.1.

$$n = \frac{\text{settlement of untreated soil model}}{\text{settlement of treated soil model}} \quad (5.1)$$

Influence of area replacement ratio (a_s)

The model was explained in detail in Section 5.2.1. Here, the same consolidation analysis was performed, with altering the area of replacement in an acceptable range, to find the impact on the settlement and the time for consolidation. Figure 5.4 shows the time history of the settlement for an area replacement of 11%, 15%, 20%, 25%, and 30% compared with the non-improved soil condition, for various lengths of stone columns.

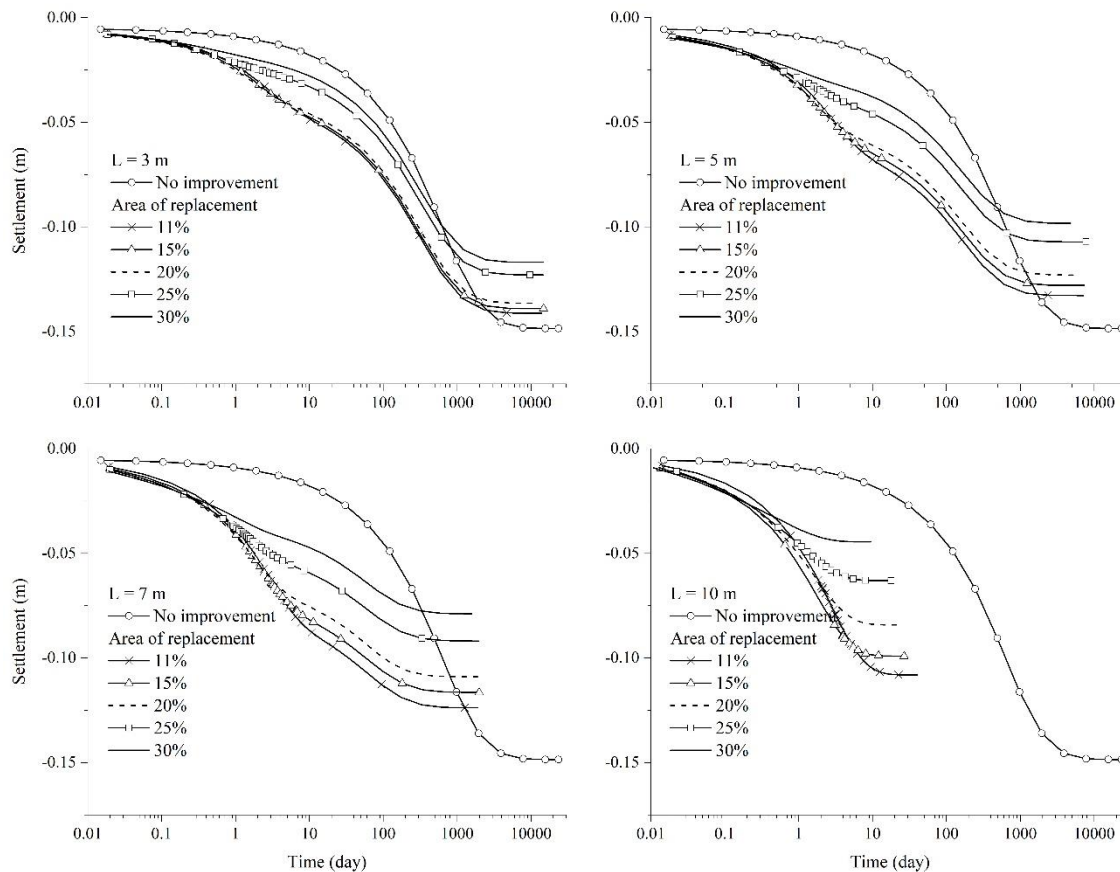


Figure 5.4 Effect of the area ratio ($a_s = 11, 15, 20, 25$, and 30%) on settlement and consolidation time in case of different stone columns length ($L = 3, 5, 7$, and 10 m) compared to no-improved soil model

For a 10-m column, an increase in the area of replacement led to much less settlement and a rapid reduction in the consolidation time, compared with the non-improved condition. The same behavior was

observed for lengths of 5 m and 7 m, although longer columns were needed to attain a shorter time for consolidation with less settlement. The shortest column, 3 m, did not noticeably decrease the consolidation time but did reduce the settlement. For the 11% area replacement, the settlement improvement factor was 1.05 for the shortest column and 1.37 for the longest column. For the 30% replacement case, these values were 1.27 and 3.34 respectively.

In general, the area of replacement had a strong effect on the improvement of settlement. Higher area of replacement reduced the overall settlement by improving the composite stiffness of the whole model. However, the rate of consolidation for short columns was not improved, whereas increasing the length raised the consolidation rate noticeably. Short columns were suitable for controlling the settlement rather than boosting the consolidation rate.

Influence of friction angle of column material

The results for increasing the friction angle of stone columns in relation to the depth of the columns at constant area of replacement are presented in Figure 5.5.

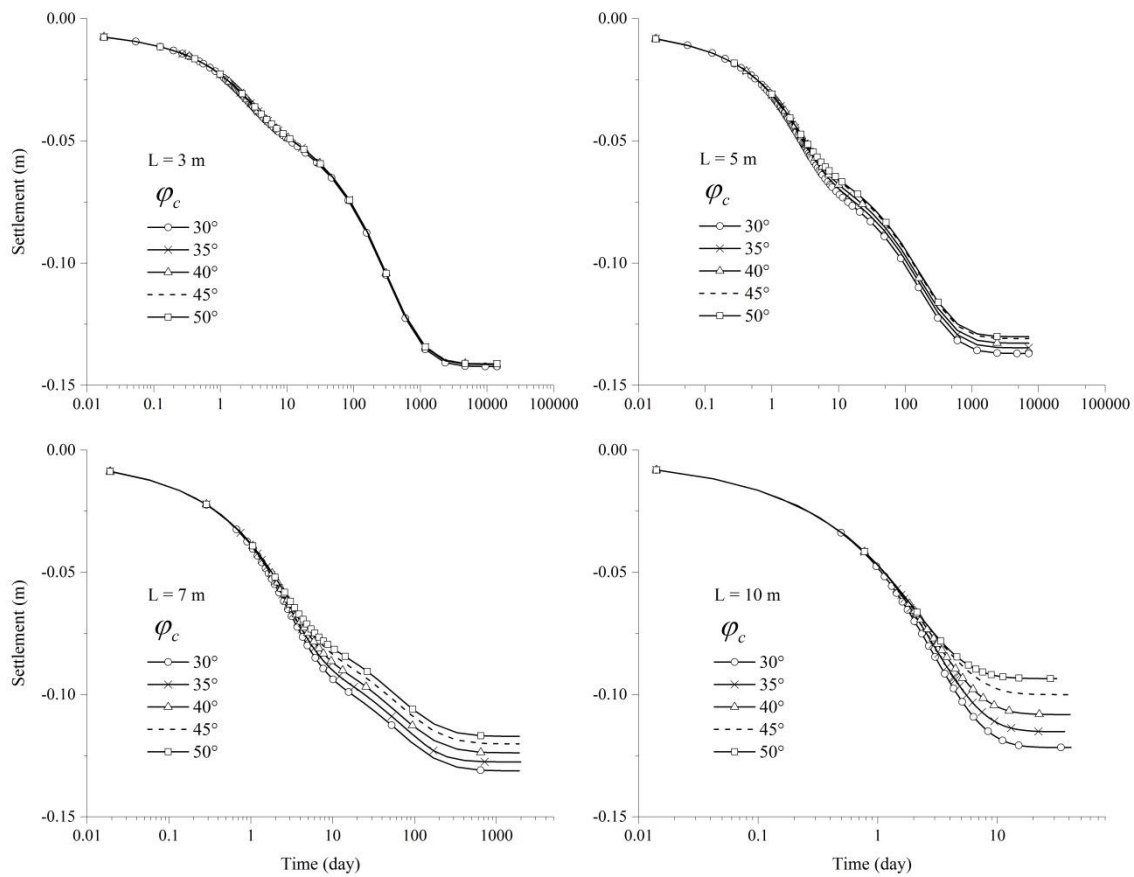


Figure 5.5 Effect of the friction angle ($\varphi_c = 30, 35, 40, 45$, and 50 degrees) on different stone column lengths ($L = 3, 5, 7$, and 10 m).

By increasing the depth of the column, the effect of the friction angle on reducing the total settlement was greater. For instance, increasing the friction angle for the shortest column had no effect on

decreasing the settlement, whereas a more substantial decrease was noted for the fully penetrated column. For short columns, changing the friction angle had no effect on the settlement improvement factor. However, for columns based on the dense layer at the bottom, the settlement improvement factor was increased from 1.23 (the lowest friction angle) to 1.6 (the highest friction angle). This was only a small increment and changing the friction angle parameter to achieve a higher improvement factor might not be cost effective.

Influence of applied load

Figure 5.6 shows that an increase in the applied load caused nearly the same increment in the settlement for all length of columns. However, as expected, the final settlement for the fully penetrated column was less than the others. The development of plastic strains in the soil and column as a result of the higher applied surface load prevented any gain in shear strength for the improved soil; therefore, settlement continued to increase under greater loads. It was also expected, based on the slope of the settlement increment, that the settlement improvement factor would be reduced for all lengths of columns when the applied load was increased.

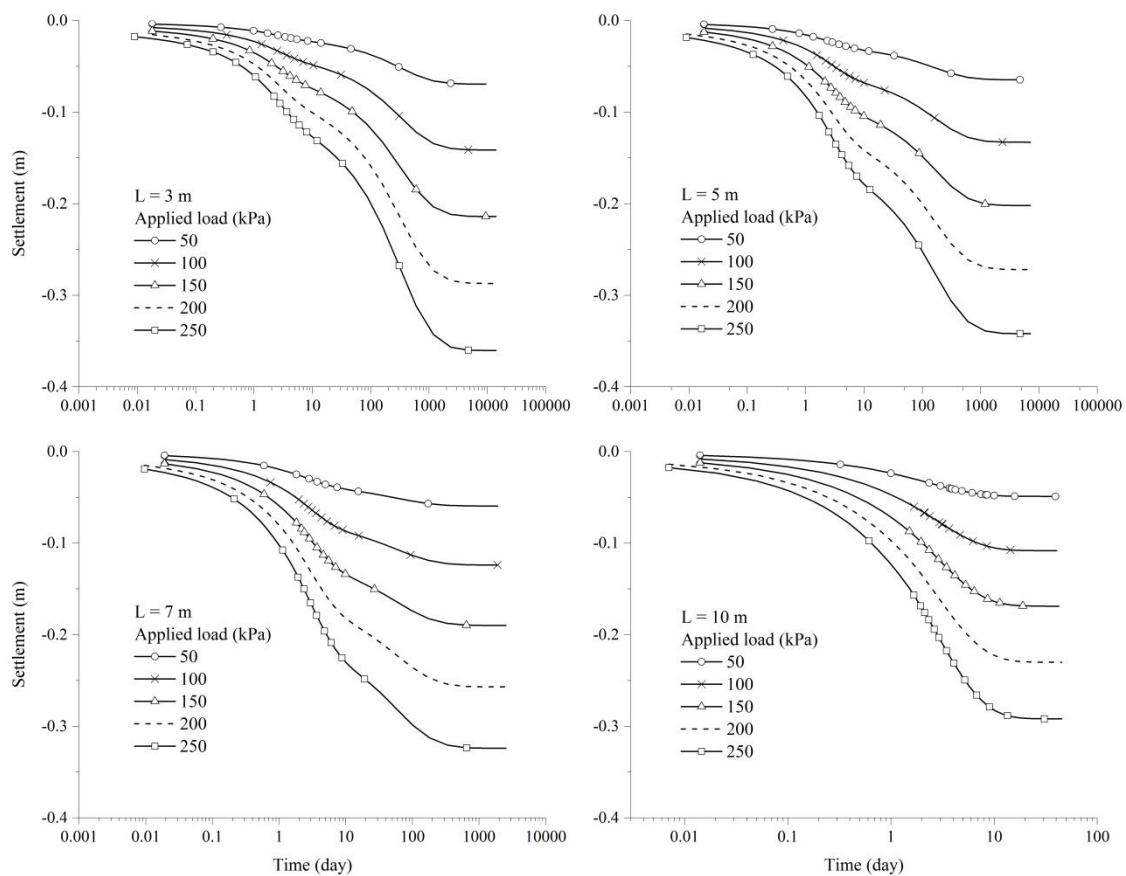


Figure 5.6 Effect of the applied load (50, 100, 150, 200, and 250 kPa) on settlement and consolidation time in case of different stone column lengths ($L = 3, 5, 7$, and 10 m).

Influence of modulus ratio (m)

The results shown in Figure 5.7 indicate a negligible effect of the modulus ratio ($m = \frac{E_{\text{stone column}}}{E_{\text{Soil}}}$) on the settlement, in all cases. However, increasing the modulus ratio led to very slight positive effects in case of longer column. It can be concluded that parameters other than column stiffness were more important in controlling the settlement after implementing the stone columns. In addition, apparently the effect of the size of isolated soft soil between adjacent columns played a more important role than the stiffness of the material used for constructing stone columns.

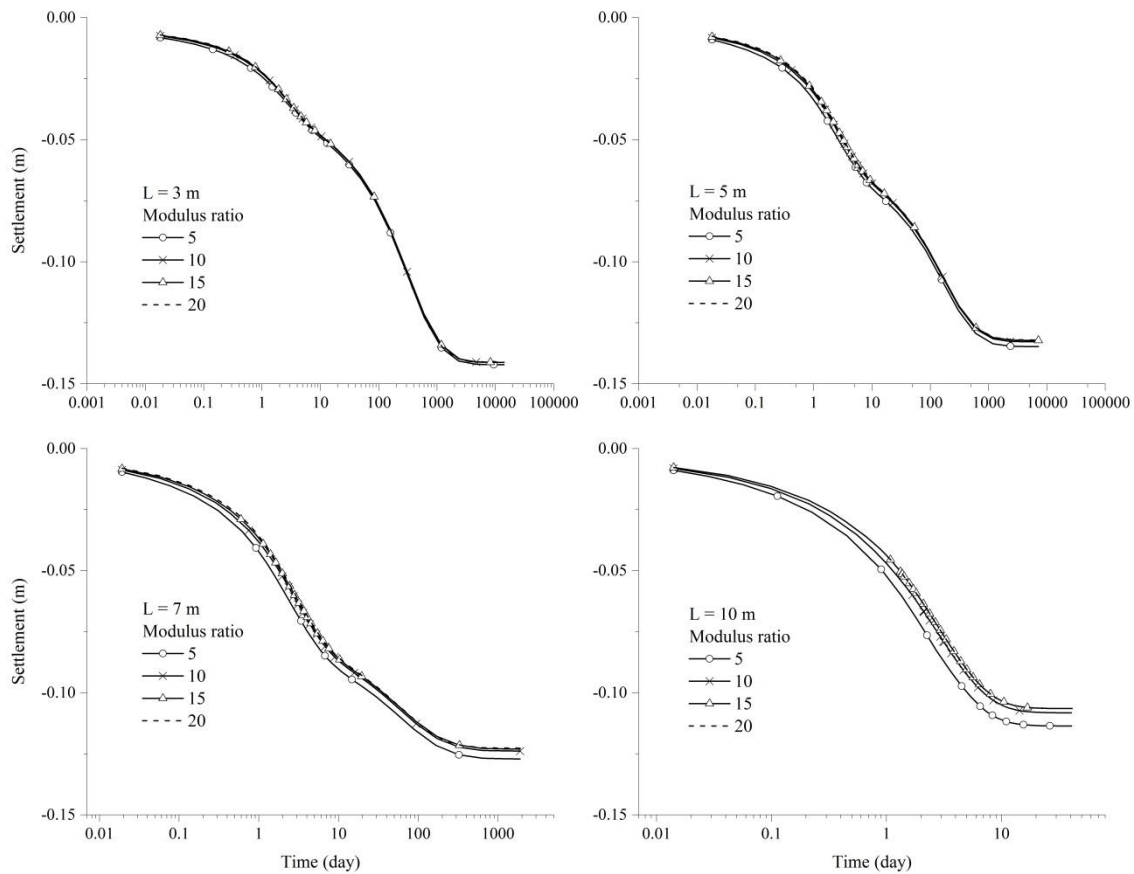


Figure 5.7 Effect of the modulus ratio ($m = 5, 10, 15$, and 20) on different stone column lengths ($L = 3, 5, 7$, and 10 m).

Influence of column space at constant area of replacement

The effects of the spacing between adjacent columns were studied by keeping the area of replacement constant. The center-to-center distance among the columns was assumed to be 1, 1.5, 2, 2.5, and 3 meters, respectively. The influence area of the columns varied accordingly, and to maintain a constant area of replacement value of 20%, the diameter of columns was also varied. Table 5.2 shows the diameter of columns and their influence diameters (based on Figure 5.1).

Table 5.2 Model dimensions for equal areas of replacement but different spacing between columns

Stone column spacing, S (m)	Area of replacement, a_s (%)	Diameter of column, d (m)	Diameter of area of influence, $d_e = 1.13S$ (m)
1.0	20	0.55	0.57
1.5	20	0.76	0.85
2.0	20	1.0	1.13
2.5	20	1.26	1.42
3.0	20	1.5	1.70

In Figure 5.8, it can be seen that increasing the distance between stone columns from 1.5 m to 3 m had little effect on the settlement. However, for the same area of replacement, spacing of 1 m resulted in less settlement for all lengths of the columns. The effect was much smaller for shorter columns than for longer columns, but construction of the columns with such small spaces and diameters is problematic and not easy. Nevertheless, a variation of the distance does not have a large effect on settlement for all considered lengths of the columns.

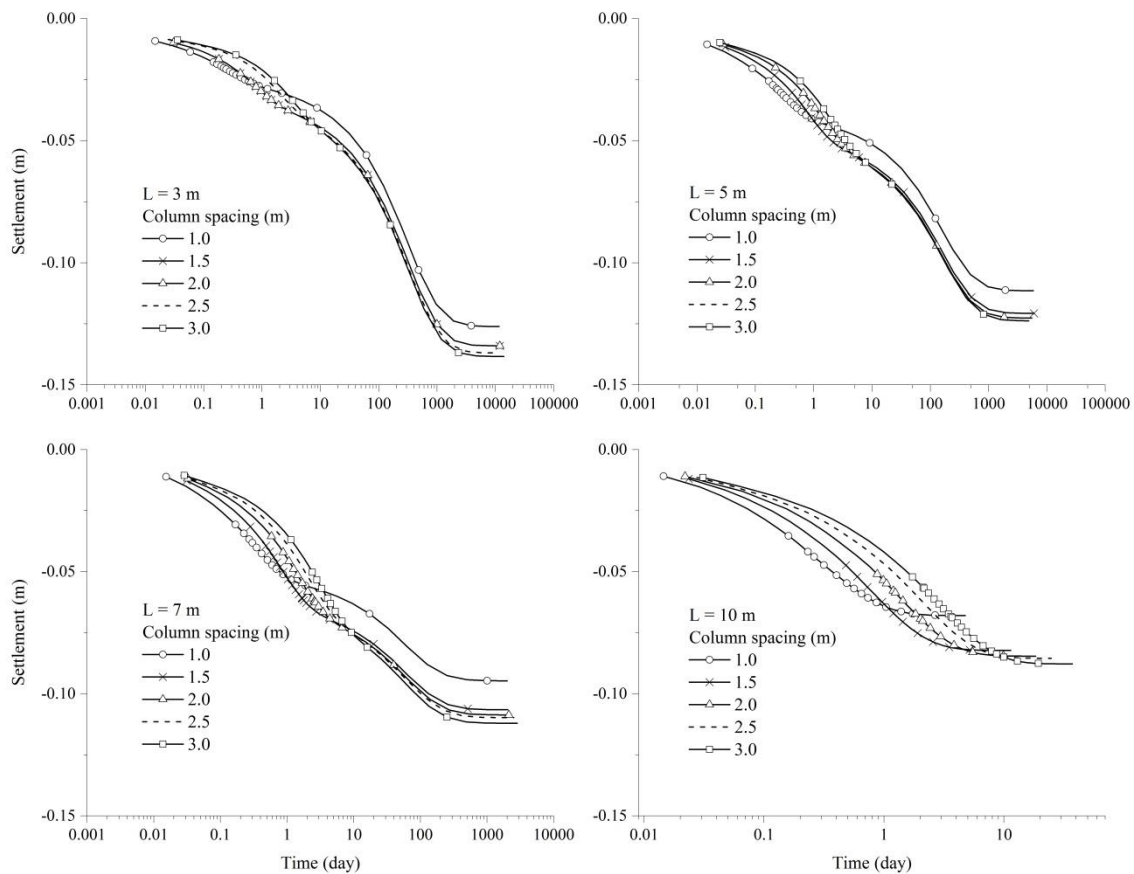


Figure 5.8 Effect of column spacing ($S = 1, 1.5, 2, 2.5$, and 3 m) on settlement for different stone columns lengths ($L = 3, 5, 7$, and 10 m) while the area of replacement is constant ($a_s = 20\%$).

5.3 Plane strain modeling

5.3.1 Geometry and material properties

The plane strain approach involves replacing the stone columns with stone walls (strips) to create an equivalent overall plan area. The application of a profile method or equivalent strip for modeling the stone columns (Section 2.10.4) is necessary for modeling in plane strain conditions. The idealization formula for the equivalent strip is given in Equation 55.2.

$$w = a_s \cdot s \quad (55.2)$$

In the above formula, the distance between two adjacent columns in a plane section is represented by s and the percentage of the area replacement a_s is the total area of the stone columns divided by the original area of unreinforced soil. This calculation can be simplified as Equation 55.3.

$$a_s = \frac{d^2}{(d_e)^2} \cdot 100 \quad (55.3)$$

The area replacement percent is limited to the range of 10% to 30%. For replacement of less than 10%, minor improvement can be achieved, whereas if the replacement exceeds 30% then installation difficulties can occur. With reference to parametric studies on the area of replacement, particularly Figure 5.4, the choice of 20% of replacement suggests a good balance between ease of construction, costs, and providing the required improvement. Therefore, this percentage was used for the simulation.

In this section, a plane strain condition is considered and due to the symmetry, only half of the geometry was modeled. It was assumed that stone columns and soft soil both experienced the same amount of settlement. This is common in many practical case studies; a sandy layer covers the top surface of the composite stone column and soft soil layer. A sand layer of 0.2 m thickness was therefore placed at top of the model.

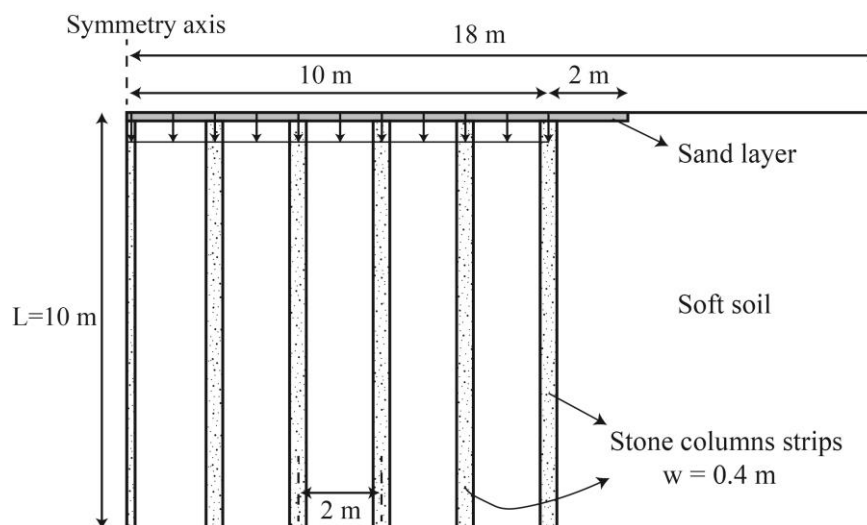


Figure 5.9 Schematic view of the plane strain numerical analysis model (Stone column length $L = 10$ m).

The diameters of the stone columns were assumed to be 1 m, with a center-to-center of 2 m; therefore, strips 0.4 m wide were placed at a distance of 2 m in the plane strain model. Fixed supports were considered at the bottom of the geometry and roller supports occurred at the vertical boundaries. To study the effect of the lateral earth pressure on the behavior of the system after installing the columns, and to keep all other parameters constant, a prescribed settlement of 0.2 m was applied at the top of the model and with a lateral extension of 10 m, being identical with the length of the implemented columns. The model is shown in Figure 5.9.

The material properties were chosen identical to those as in the previous sections. Drainage behavior was assumed for all the materials and no ground water was considered in the model. All properties including those of the sand layer are listed in Table 5.3.

Table 5.3 Material properties for the plane strain calculation

	Type	E (kPa)	ν (-)	ϕ (°)	c (kPa)	γ_{sat} (kN/m ³)
Soft soil	Drained	5000	0.30	21.0	5.0	19.0
Stone column	Drained	50000	0.30	40.0	0.1	19.0
Sand	Drained	20000	0.30	30.0	4.0	16.0

5.3.2 Effect of lateral earth pressure

One of the reasons that construction of stone columns improves the behavior of soft soil is the densification of soil around the columns. Due to the installation process, vibrations and horizontal displacement cause compression in the soil and an increase in lateral earth pressure. However, the amount of the increase depends on the type of soil, spacing of stone columns, and installation method.

To calculate the effect of the lateral earth pressure on the behavior of the improved ground, the coefficient of the earth pressure K_0 was increased by 25%, 50%, and 75% for different lengths of stone columns. All other parameters were kept constant, as explained in Section 5.3.1.

Figure 5.10 shows the stress-settlement behavior of the ground for different lateral earth pressures, whereas the curves for k_0 correspond to the case that no effect of installation on the surrounding soil was considered. An increase in the coefficient of lateral earth pressure increased the stresses only slightly and it was neglected for the analyses of stone columns. Increasing the length of the stone columns led to higher stress, which meant greater stiffness. In other words, by increasing the length of stone column, the soil could bear higher stress for the same amount of settlement.

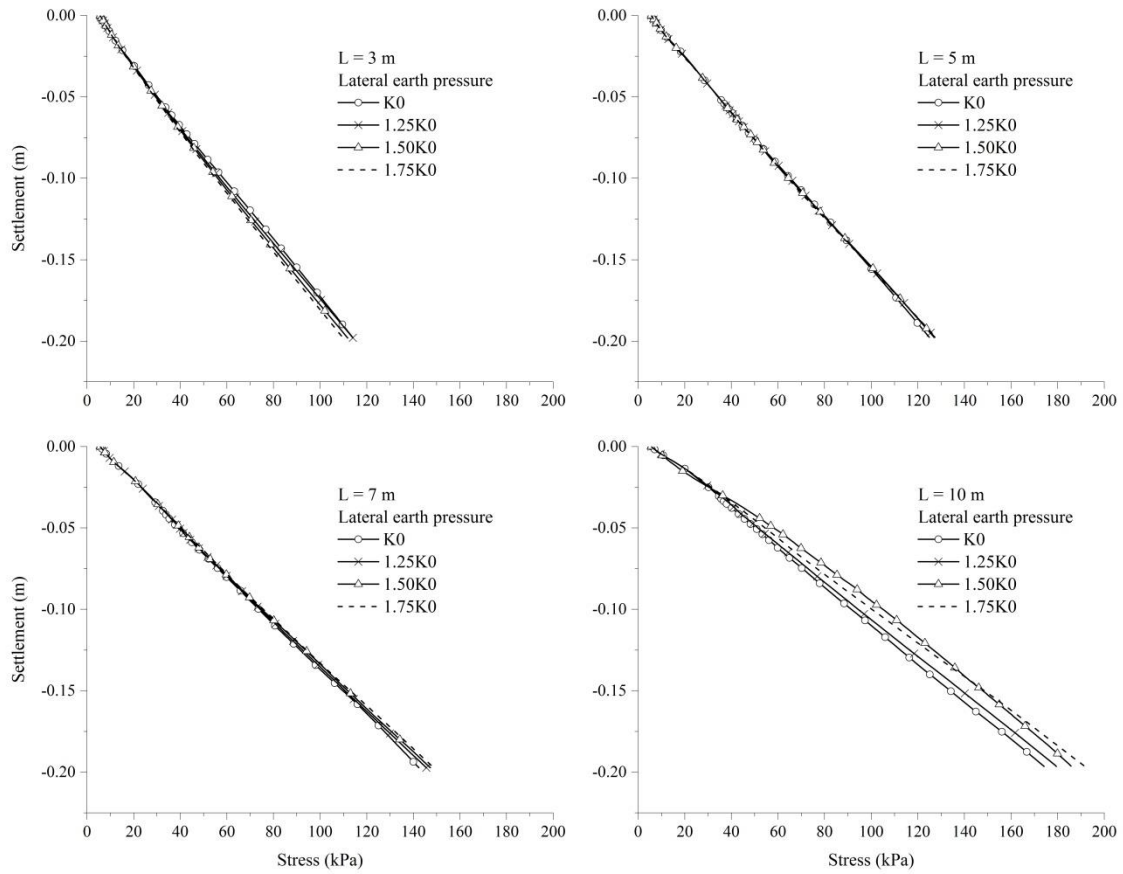


Figure 5.10 Stress-settlement behavior of stone columns with different lengths ($L = 3, 5, 7$, and 10 m) when increasing lateral earth pressure and keeping the area of replacement constant ($a_s = 20\%$).

5.4 Arrangement of stone columns beneath a railway track

Plane strain (2D) finite element (FE) analyses were performed on a cross-section of the track to find the optimal arrangement of the stone columns with respect to the center line of the loaded track (track axis). Sleepers are discrete elements in conventional railway track, whereas in a 2D analysis they are modeled continuously. Hence, Young's modulus of the sleepers was scaled with the aid of Equation 5.4, that means by the ratio of sleeper width w to spacing a , to give the same value of lateral bending stiffness EI per meter run of the track as occurs in reality for discrete sleepers. In addition, the same assumption was used to adjust the Young's modulus of the rail pads.

$$E(2D) = \frac{E(3D) \cdot w}{a} \quad (5.4)$$

Due to the symmetry of the railway track, only half of it was modeled. Its geometry is shown in Figure 5.11, and the material properties of the track are listed in Table 5.4.

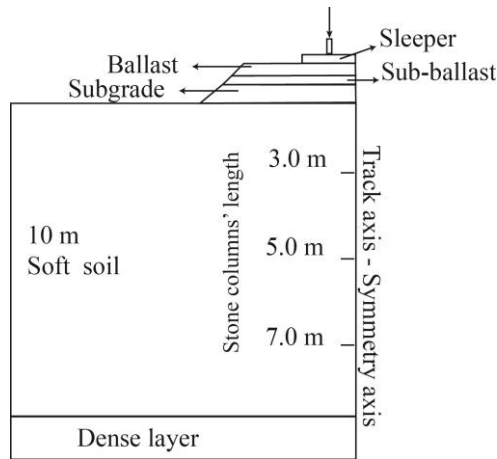


Figure 5.11 Half-symmetric model of the railway track

Table 5.4 Material properties of model used to study stone column patterns beneath a railway track

	Young's modulus (MPa)	Poisson's ratio (-)	Wet density (kg/m ³)	Depth (m)
Rail	200000	0.15	7800	-
Rail pad	30	0.30	950	-
Sleeper	10000	0.3	2400	-
Ballast	200	0.20	1600	0.30
Sub-ballast	299	0.30	2200	0.15
Subgrade	100	0.30	2100	0.50
Soft soil	5.00	0.30	2100	10.0
Dense layer	200	0.30	2100	2.00
Stone column	75	0.30	1900	3.0, 5.0, 7.0, 10

A vertical load transferred from the moving train to the track can be higher or smaller than its static value, which depends on downward or upward acceleration of the vehicle at that exact moment. However, it is common in static analysis to consider the dynamic effect by an impact load (dynamic amplification) factor. As mentioned in Section 2.4.4, this factor can be calculated by different approaches; here the American formula – which relates the factor to the train speed and diameter of train wheel – was used. For this calculation, a train speed of 180 km/h was considered. The area of replacement was kept constant at 20%, whereas the center-to-center distance of columns was varied (1, 1.5, 2, and 2.5 meters). Figure 5.12 shows two scenarios for arrangement of stone columns in a square pattern: two rows of columns are located on each side of the track axis in Arrangement 1, while a row of columns is located directly in the track axis in Arrangement 2.

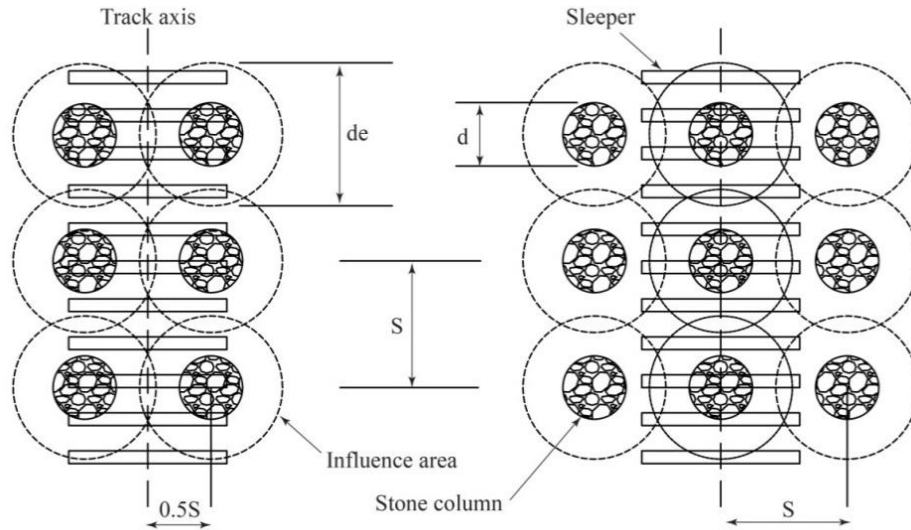


Figure 5.12 Arrangement of stone columns with regard to the track axis. Left, columns with offset from the axis (Arrangement 1); right, center of columns are aligned to the axis (Arrangement 2).

The results of these calculations are presented in terms of vertical and horizontal displacement at the middle of subgrade to find the effect of the stone columns on the track. Figure 5.13 shows the displacement in the subgrade for various column lengths and spacing, in two different arrangements having the same area of replacement, compared with ground that lacked any improvement techniques. The two different arrangements of the stone columns, with and without offset from the track axis (while the area of replacement was kept constant), did not yield different results. However, even the presence of short columns led to much smaller vertical displacement in the subgrade.

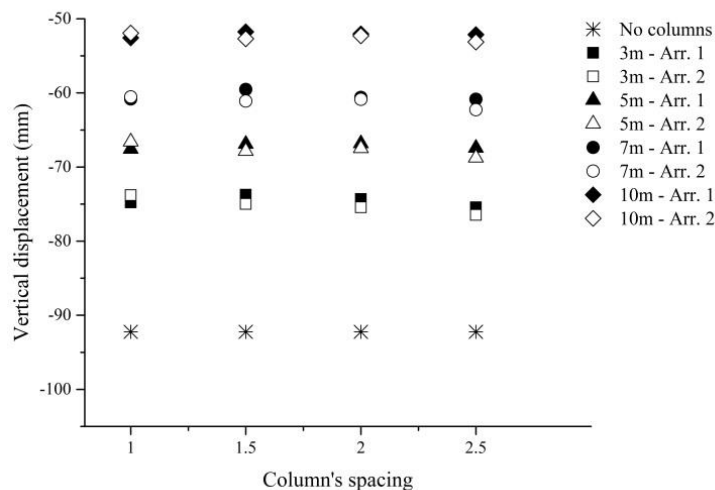


Figure 5.13 Vertical displacement at middle of subgrade for two types of arrangements, columns with and without offset from the axis (Arr.1 and Arr.2) as a function of the spacing of the stone columns (1.0, 1.5, 2.0, and 2.5 m) for different column lengths (3, 5, 7, 10 m)

Similarly, Figure 5.14 shows that the use of stone columns reduced the horizontal displacement compared with the non-improved ground. Unlike for the vertical displacement, when column spacing was greater than 2 m, the second arrangement (in which the center of columns was aligned to the track axis) resulted in much smaller displacement. The effectiveness of the second arrangement was significant. The application of 3-m columns in arrangement 2 reduced the horizontal displacement as effectively as the 10-m columns in the first arrangement.

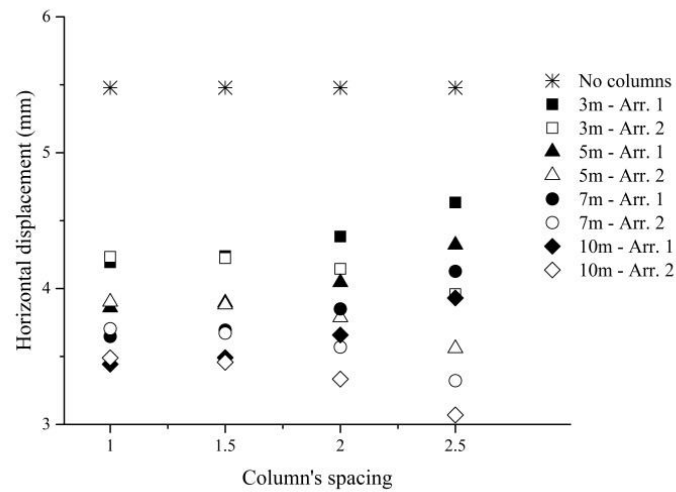


Figure 5.14 Horizontal displacement at middle of subgrade for two arrangements: columns with (Arr. 1) and without (Arr. 2) offset from the axis as a function of the spacing of the stone columns (1, 1.5, 2, and 2.5 m) for different column lengths (3, 5, 7, 10 m).

6 Stone Columns under Railway Tracks

6.1 Introduction

The behavior of railway tracks constructed on soft soil, especially in case of improved ground, under dynamic loading by passing trains has not been thoroughly studied. Moreover, the effects of train speeds on soil improved by stone columns, and the effect of the length of the columns, have not been investigated.

In the previous chapter, the effect of stone columns, in particular their length for improvement of soft ground was comprehensively studied. Here, the benefits of stone columns under the passage of a train travelling at various speeds are examined, and the response of the track in terms of stress and strain fields is analyzed. A hypothetical geometry of a railway track on a soft soil layer with a depth of about 10 m, based on real railway tracks (Chapter 3) is introduced for numerical simulations.

During the passage of a train, all components of a track are exposed to vertical and horizontal vibrations. As mentioned earlier, the vibrations induced in the system consist of compression and shear waves in the soil body and Rayleigh waves at the surface (Figure 6.1). However, the impact of these waves depends on many factors, such as the depth, density, and stiffness of the soil. In general, the amplitude of these oscillations increases with a decrease in the soil stiffness.

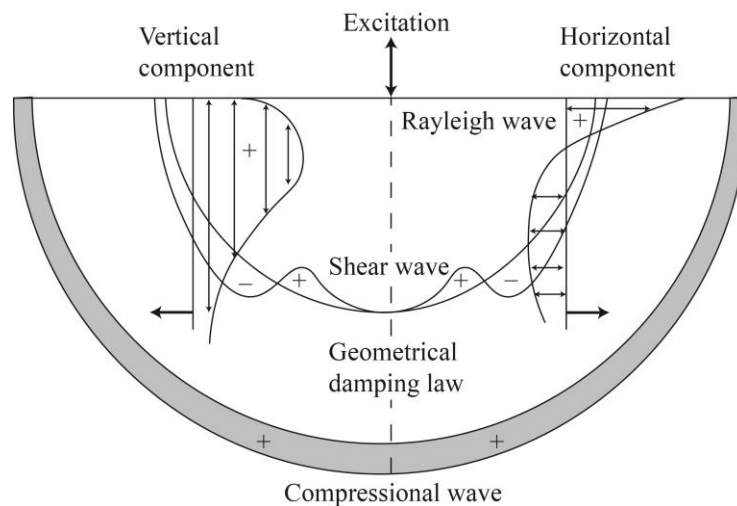


Figure 6.1 Seismic wave distribution (after Connolly et al., 2013)

Two main factors control the amplitude of the vibrations. One is the active frequency f_A , which is related to the train's passage; the other is the natural frequency, f_N , of the whole track. According to the equation of motion, if active frequency becomes equal to natural frequency, the critical situation of an undamped system occurs, which leads to infinite motion. These two frequencies can be obtained from Equations 6.1 and 6.2, where distance between wheels is a , train speed V and d is the layer thickness (Katzenbach and Ittershagen, 2004).

$$f_A = \frac{V}{a} \quad (6.1)$$

$$f_N = \frac{V_s}{2d} = \frac{\sqrt{\frac{E}{2(1+\nu)\rho}}}{2d} \quad (6.2)$$

The relationship between the active frequency and the distance between the wheels is given in Figure 6.2. In the same figure, natural frequency is plotted versus depth of the underlying soil layer for different values of soil stiffness. When the train speed does not exceed 180 km/h and the wheel set distance is at least 5 m, the active frequency is limited to 10 Hz. If the soil layer has a low stiffness (e.g. 10000 kN/m² or less) and the depth is more than 2 m, the natural frequency is limited to 10 Hz as well. Therefore, both frequencies fall into the same range and controlling deformations becomes problematic. In such a situation, train speed for the track will be restricted to low speeds or the track must be closed temporarily. Increasing the stiffness of the soil is one approach to overcome the problem; this can be achieved, by adding stone columns which increase the average stiffness of the soil under the railway track. The track will further benefit from the reduction of consolidation time and show a better response against vibrations.

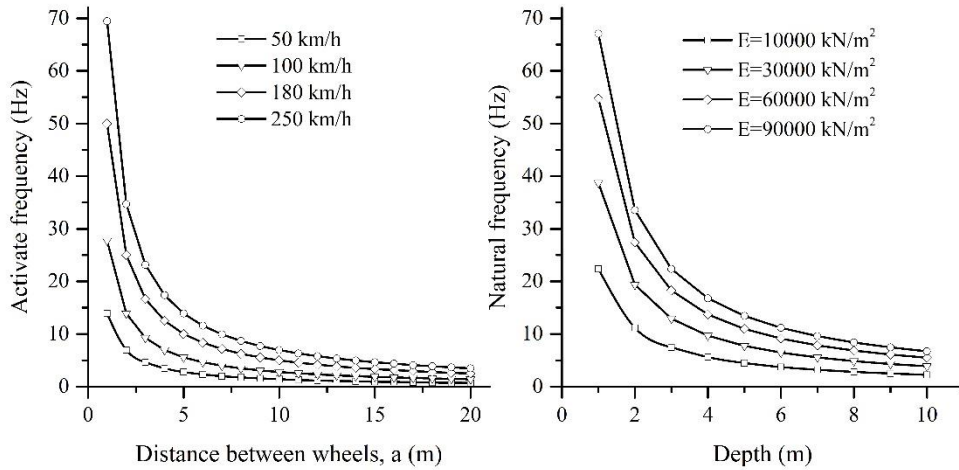


Figure 6.2 Active (f_A) and natural (f_N) frequencies in relation to wheel distance and depth of soil layer, respectively (after Katzenbach and Ittershagen, 2004).

6.2 Numerical simulation

6.2.1 Properties of the track and train

The hypothetical geometry of a conventional ballasted double railway track is considered in this chapter. This geometry is defined based on the soil layers of field measurements, as explained in Chapter 3. To study the effect of the length of the stone columns, soft soil depth was increased to 10 m. All properties and the geometry of the case are presented in Table 6.1 and Figure 6.3.

Table 6.1 Material properties of the hypothetical geometry to study the effect of the length of the stone columns

	Young's modulus (MPa)	Poisson's ratio (-)	Density (kg/m ³)	Depth (m)
Ballast	200	0.20	1600	0.30
Sub-ballast	299	0.30	2200	0.15
Subgrade	100	0.30	2100	0.50
Soil layer 1 – Soft soil	5.00	0.30	2100	10.0
Soil layer 2 – Dense layer	200	0.30	2100	2.00
Stone column	75	0.30	1900	3.0, 5.0, 7.0, 10

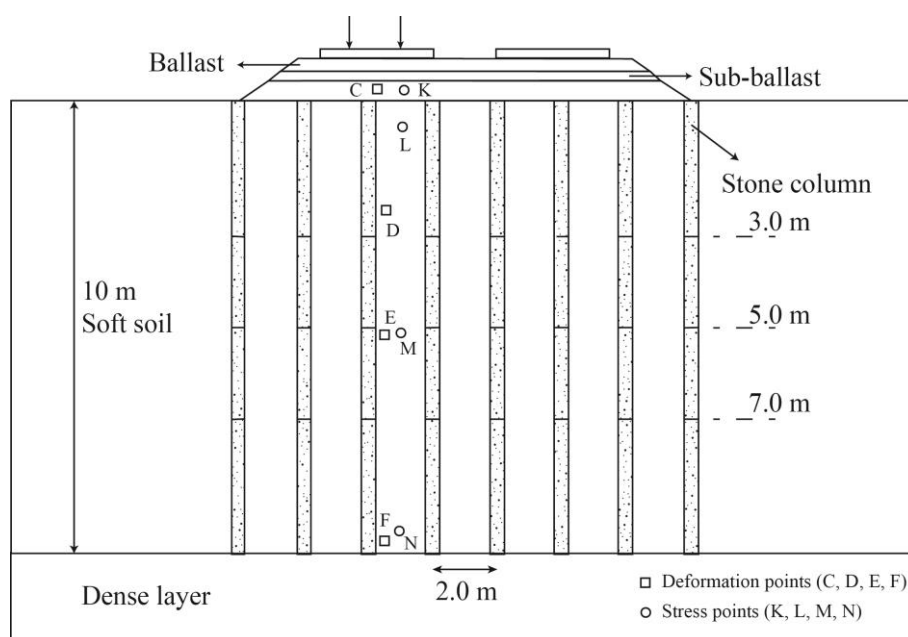


Figure 6.3 Geometry of the hypothetical railway track, with different stone column lengths (3, 5, 7 and 10 m) and a center-to-center distance of 2 m. The locations of the stress and deformation checkpoints are shown.

A TGV train, including 12 axles with a load of 170 kN, was used to induce the dynamic loading. Detailed information about the train configuration is provided in Section 3. It should be noted that changes in the soft soil properties due to the installation of stone columns (Section 5.3.2) were minimal and are ignored in this study. Stone columns were arranged in a square pattern with a center-to-center of 2 m and a diameter of 1 m – which is equal to a strip of 0.4 m width in the plain strain condition (Section 2.10.4 and Section 5.3.1). According to the analysis discussed in Section 5.4, the columns were aligned with the center of a track.

To consider the worst-case scenario in construction of stone columns and their immediate behavior under the passage of the first train, the sand blanket or geogrids which are normally implemented in constructions are neglected in the model. For later calculations and analysis of the results, deformation points and stress points are defined in the model. The deformation points are C, D, E, and F, with depths of 0.7 m, 2.3 m, 5.3 m and 10 m below the top surface of the ballast layer. The stress points are K, L, M, and N, located at depths of 0.8 m, 1.4 m, 6 m and 10 m, respectively. All the stress points were

aligned to the load on the right- hand side rail, whereas the deformation points were not exactly adjusted to lie beneath the load.

6.2.2 Verification of developed 2D model

In the previous chapters a simple 2D model was developed and verified with available field data, and the accuracy of a 3D model was also investigated. As mentioned, to study the effect of the stone columns, a hypothetical geometry was considered. Due to the lack of field measurements for such a case, the developed 2D model was verified against the 3D model. Because of the effort and time that are needed for a 3D model, only two 3D models were simulated, using one train speed. One was the geometry without improvement – that is, no stone column; the other was the same geometry with implementation of 3-m stone columns. The models were tested for the passage of a train at a speed of 130 km/h.

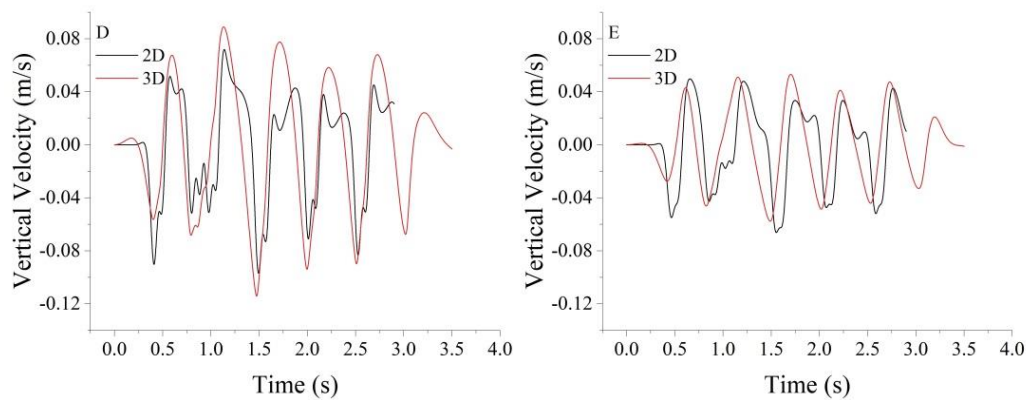


Figure 6.4 Vertical velocity in 2D model and 3D model with no stone columns determined in points D and E (train speed 130 km/h).

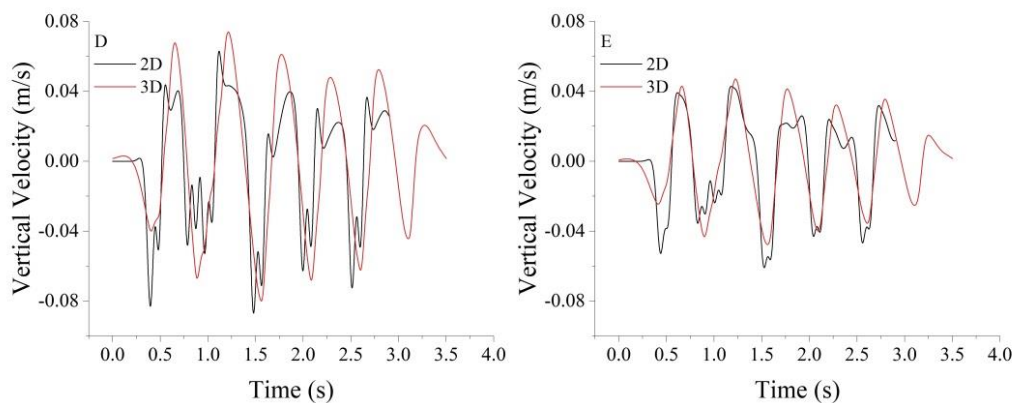


Figure 6.5 Vertical velocity in 2D model and 3D model with stone columns with a depth of 3 m (train speed 130 km/h).

Figure 6.4 shows the verification of the developed 2D model and 3D simulation for the case that there are no stone columns. Figure 6.5 presents the same comparisons, but for a case in which there were stone columns with an embedding depth of 3 m.

The results from the 2D model showed good agreement with the more elaborate 3D model. Therefore, the 2D model can be used as a trustworthy approach for later studies on the influence of train speed and stone column depth. Closer examination of both figures suggested that constructing stone columns, even of a short length, would improve the performance of a track under the passage of a train.

Owing to the good performance of the developed 2D model (at a much lower computational cost), further analysis of the linear and nonlinear responses of the track relied on the 2D model alone. To study the response of the track, in particular the effect of stone column lengths, simulations of the model under the passage of trains with various speeds was necessary. To accomplish this, the procedures described in Section 4.3 were applied to the new geometry, and pressures under the sleepers at various train speeds (50, 80, 100, 130, 180, 220, 250 and 270 km/h) were obtained. These data were then used as the train load input in the FE model.

6.3 Effect of stone columns

6.3.1 Horizontal and vertical displacement

One of the main purposes of applying stone columns is to reduce settlement and horizontal displacement of the improved soil. The benefits of stone columns of different penetration lengths were studied in terms of decreasing the horizontal and vertical displacement of the track under the passage of a train travelling at various speeds. Figure 6.6 illustrates the horizontal displacement of the stone columns at their boundary as a function of depth. It is evident that even the shortest stone column (3 m) results in much smaller horizontal displacements. As the column length increases, the displacement decreases. However, when the speed of the train increased to over 180 km/h, the effect of the depth of the stone column in reducing the horizontal displacement was decreased. In other words, for higher speeds, in terms of horizontal displacement reduction there are negligible effects from increasing the length of stone columns.

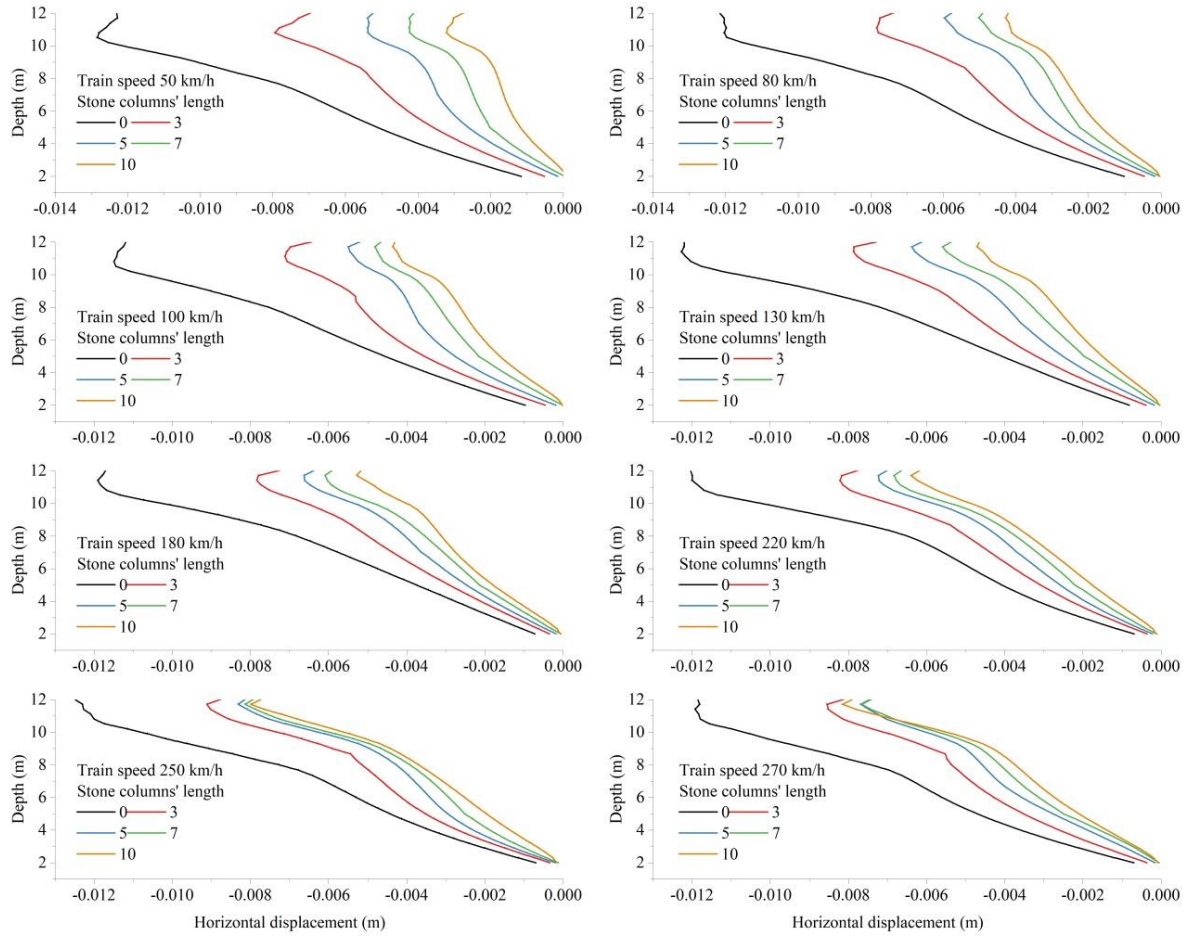


Figure 6.6 Horizontal displacement along a stone column (column length/depth was 2–12 m)

Vertical displacement was also highly affected by introducing stone columns into the model. As Figure 6.7 shows, even the shortest stone column resulted in smaller displacement in the upper layers (subgrade). As the stone column extends deeper into the soil, displacement reduction is greater. However, there were minor differences between the 7-m stone column and the fully penetrated one. In general, fully penetrated stone columns can reduce the vertical displacement of the subgrade to half of non-improved ground. An important finding from these calculations is that an increase in train speed does not necessarily lead to higher displacement in subgrade. For instance, speeds of 130 km/h and 180 km/h caused smaller displacements than lower speeds. This finding shows the importance of considering different effects of train speeds when designing a railway track; in some conditions, higher speeds would cause less harm to the track than lower speeds.

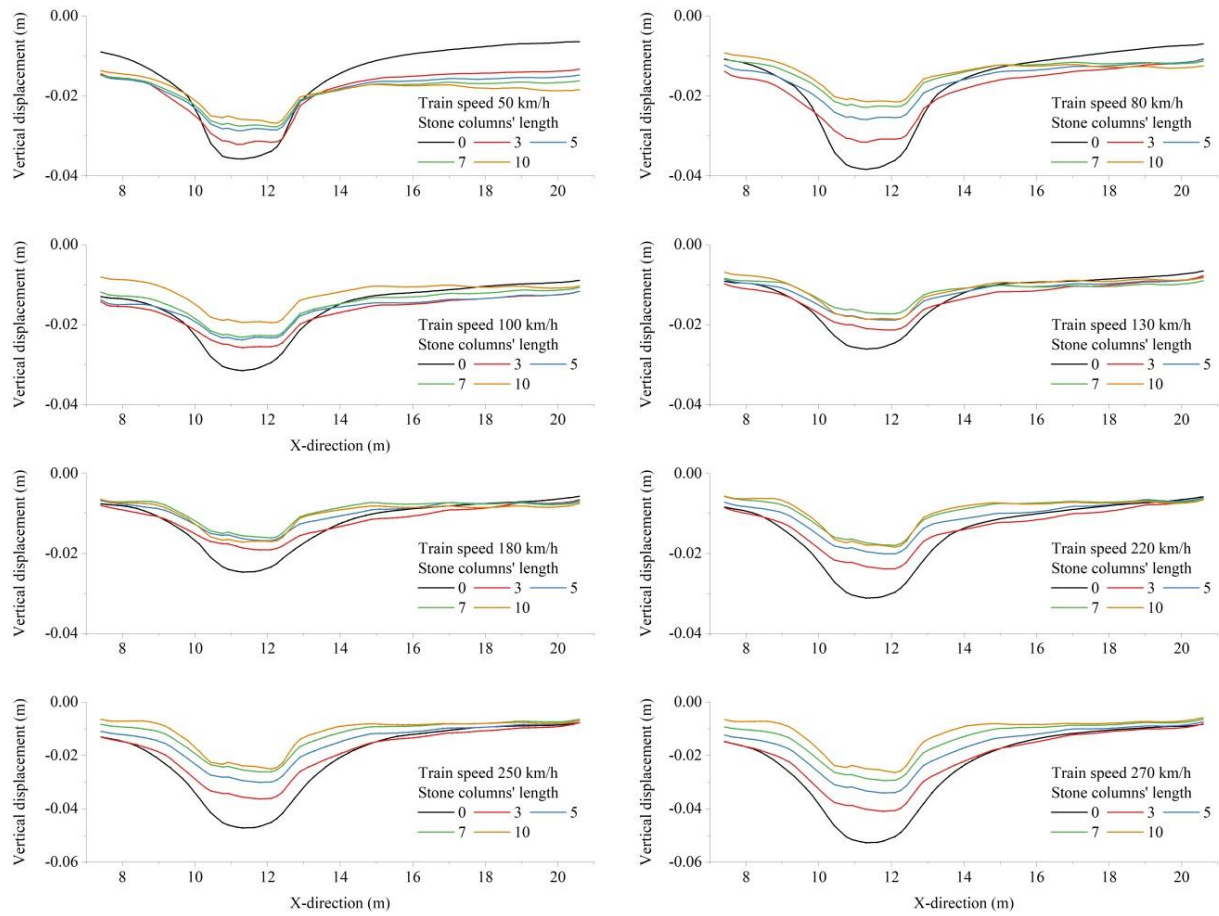


Figure 6.7 Vertical displacement of the cross-section in the middle height of the subgrade.

6.3.2 Reduction of induced vibrations

Train-induced vibrations on the surface of a railway track often have peak amplitudes as frequencies below 30 Hz, and as explained in Section 6.1, these amplitudes are important to identify. In this section, the vibration amplitude in the subgrade and soft soil due to the passage of a train at various speeds is discussed. The effects of different stone column lengths are also investigated.

As already discussed, at larger depths the individual wheel effect disappears and the impact of train passage is felt in the bogies. Hence, the peak amplitude is generated in frequencies that coincide with the active frequencies and can be calculated from Equation 6.1. As shown in Figure 6.8, for each speed, two amplitude peaks are identified that match the calculated active frequencies for different bogie distances in a train configuration. According to Figure 3.2, the shortest interval is the distance between the last bogie of the locomotive and its adjacent passenger car (9.3 m), which increases the vibration amplitude in higher frequencies. The only exception is a train travelling at 50 km/h, for which the highest frequency peak results from only the first bogie of the locomotive. The reason is the low velocity of the train gives enough time for the induced vibration to be felt at deeper depths before the vibrations of other bogies reach the deep soil. Nonetheless, the peak amplitude is related to the distance between two

adjacent bogies in passenger cars (21.7 m). By contrast, the third peak in low frequencies for train speeds over 180 km/h is induced due to the distance between the first and last bogies in the entire train's length. In general, as the train speed increases, the peak of vibration amplitude occurs at higher frequencies; this is because of short vibration periods induced by the train bogies that pass into the depth.

Implementation of stone columns has no effect on reducing the peak vibration amplitude in the high frequencies. However, the columns can decrease the highest peak amplitude that results from two adjacent bogies of passenger cars. A fully penetrated stone column drastically reduces the highest vibration amplitude; although this reduction is limited to train speeds lower than 180 km/h. For train speeds of 180 km/h and higher, stone columns bring down the vibration amplitude of low frequencies, which are the result of the longest bogie distances across the whole train. Moreover, as the speed of the train increases, the advantage of short columns in reducing the vibration at low frequencies is lost. In other words, short stone columns have little benefit for reducing the vibrations if train speeds go over 270 km/h.

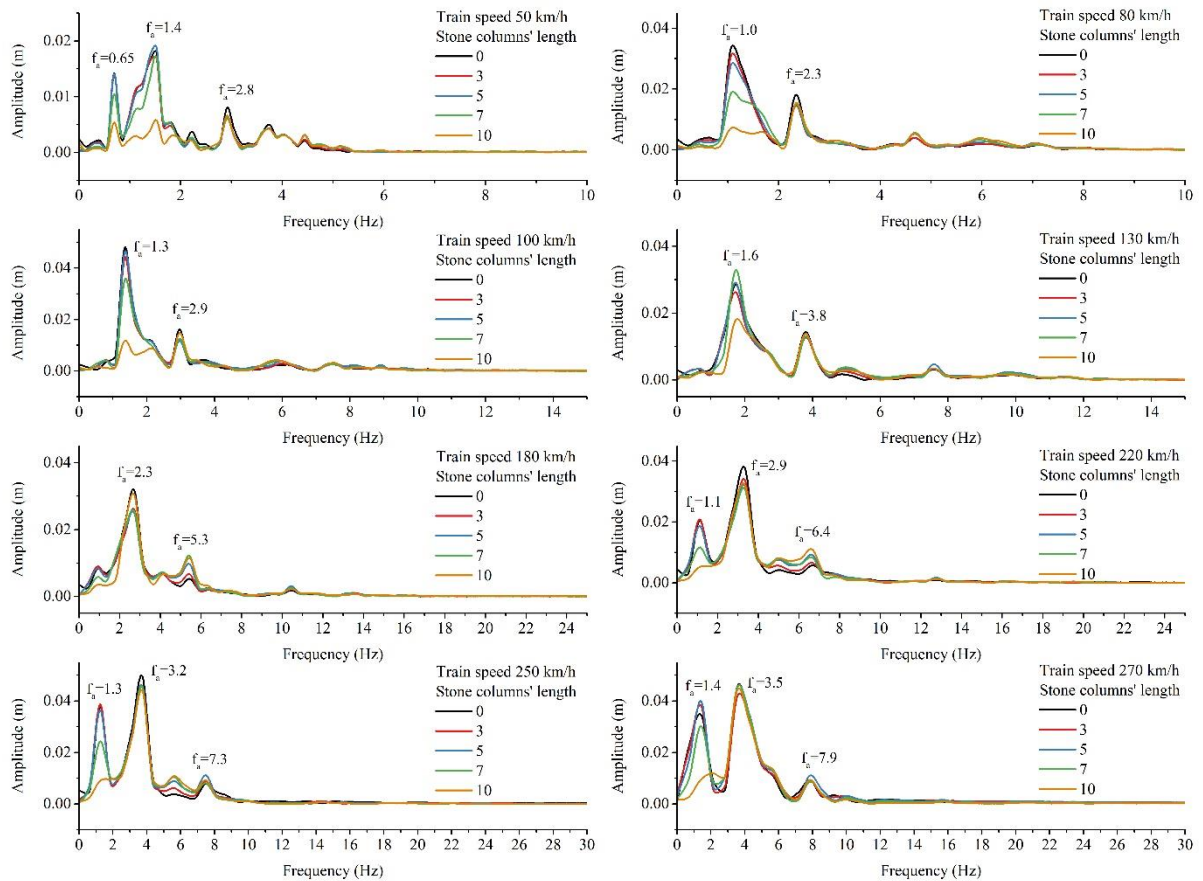


Figure 6.8 Vertical vibration amplitude in the middle of soft soil (point E). The graphs show the effect of stone column length (0, 3, 5, 7, and 10 m) under the passage of trains at various speeds (50, 80, 100, 130, 180, 220, 250, and 270 km/h).

In cases of horizontal vibration at a considerable distance from the track, namely 12 m from the center line of the loaded track, short stone columns reduce the horizontal vibration amplitude in the same manner. However, fully penetrated columns lead to smaller amplitudes than do shorter columns. As shown in Figure 6.9, when the train speed is higher this difference becomes smaller, and all columns – regardless of their length – provide similar reductions in the amplitude of horizontal vibrations. Hence, it can be concluded that the application of stone columns not only improves the ground but could also provide a simple and cost-effective reduction in vibrations from the passage of trains, in nearby buildings.

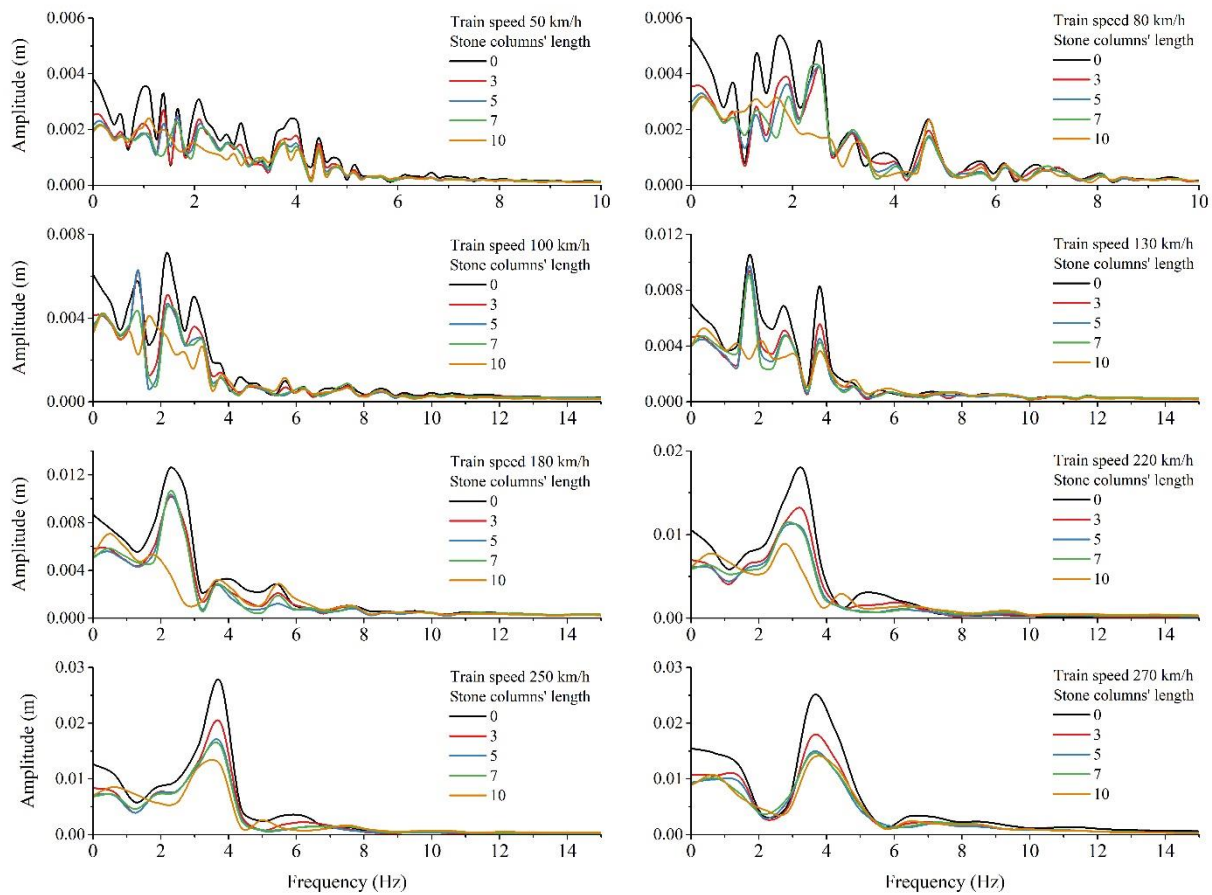


Figure 6.9 Horizontal vibration amplitude at 12 m from the center of loaded track (point G). The graphs show the effect of stone column length (0, 3, 5, 7, and 10 m) under the passage of trains at various speeds (50, 80, 100, 130, 180, 220, 250, and 270 km/h).

6.3.3 Change in pore water pressure

To study the effect of stone column length on the change of pore water pressure by passing train, soft soil is modeled with undrained condition and a global groundwater table on top. Figure 6.10 shows the effective value (RMS) of the pore water pressure for different train speeds, and different depths of the stone columns in the middle of soft soil (5 m). Clearly, columns with a length shorter than 5 m show a small reduction in pore water pressure compared with the no-column condition. Extension of the length

of columns to 5 m, 7 m, and 10 m decreases the drainage path and lowers the pore water pressure to the hydrostatic level in a shorter time. Stone columns that are 7 m long showed smaller values of pore water pressure compared with fully penetrated stone columns; the reason is that shorter columns provided two extra boundaries for drainage. The middle point was surrounded by two adjacent columns and two drainage boundaries (left and right outer boundaries of the right and left side stone columns, respectively). The 7-m column provided two more boundaries from the bottom side, in the vicinity of the middle point.

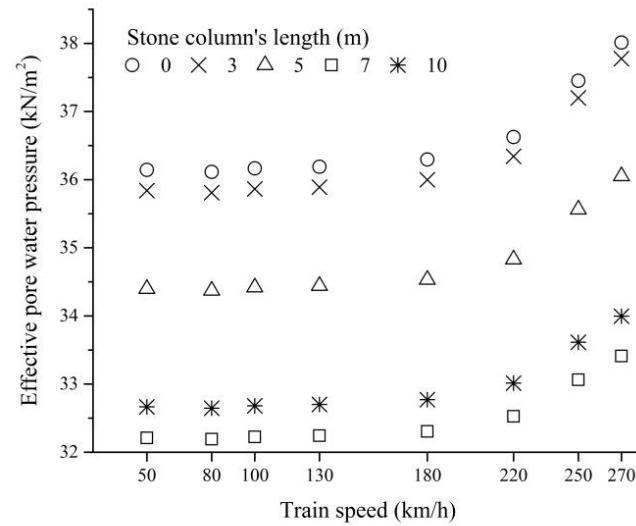


Figure 6.10 Effective pore water pressure in middle of the soft soil layer for various train speeds (50, 80, 100, 130, 180, 220, 250, and 270 km/h) and stone column lengths (0, 3, 5, 7, and 10 m).

Passage of a train causes excess pore water pressure of around 5 kN/m² in the middle of the soft soil, in ground without improvement. This value drops to less than 2.5 kN/m² in improved ground, and once the train load is removed the pressure decreases rapidly to the initial hydrostatic value. In terms of train speed, increasing the speed from 50 km/h to 180 km/h does not alter the pore water pressure much and indeed the change is considered negligible. However, raising the speed to over 180 km/h leads to an increase in the pore water pressure, which is more substantial in ground that has no stone columns, compared with improved ground. For instance, for non-improved ground, the pore water pressure increases by 5.35% when the speed increases from 50 km/h to 270 km/h, while for ground improved by 10-m stone columns this value is 4%. Nevertheless, application of specific lengths of stone columns reduces the pore water pressure by a similar amount regardless of speed. For example, if the length of stone column is kept constant at 10 m, the observed reduction of 11.3% for a train speed of 50 km/h is comparable with the observed 12.5% reduction at a speed of 270 km/h.

6.4 Elastic response of the railway track

Numerical quantification of strain and stress evolution requires numerically robust models, and all possible simplifications should be used. In the numerical simulation of railway tracks presented in this section, all layers are assumed to behave in an elastic manner. This assumption is used in this section of the analysis to define the basic stress and strain properties of the soil.

The dynamic response of a ballasted railway track subjected to a moving load at different speeds (up to 270 km/h) is analyzed. The material properties of the track were provided in previous sections. The geometry itself is hypothetical, with a 10-m depth of soft soil to allow an analysis of different lengths of stone columns (Figure 6.3). The dynamic responses of the same track after implementing different lengths of stone columns are investigated. Moreover, the influence of train speed on the elastic response of the railway track is studied. The track response for half a length of a TGV train – travelling at various speeds – is analyzed for ballast, subgrade, and the soft soil layer.

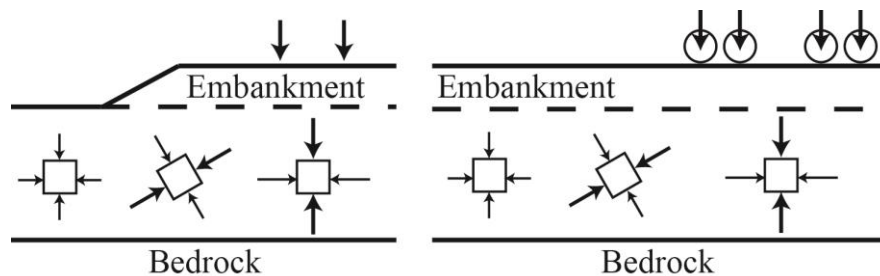


Figure 6.11 Spatial distribution of principal stress under axle loads. Left, cross-section of an embankment. Right, in plane parallel to embankment (after Hendry et al., 2013)

Stresses change in the soil beneath a track in a complex manner, due to the rotation of principal stress directions as a train passes. The rotation of stress occurs in both the longitudinal and transverse planes, while its magnitude decreases with depth as the loads are spread through the soil. Therefore, the magnitude of stress is highest near the surface, where the confining stress is the smallest where the effects of the load are felt as individual axles. By contrast, at larger depths the magnitude of stress is smaller and the effect of the train is felt in the bogies.

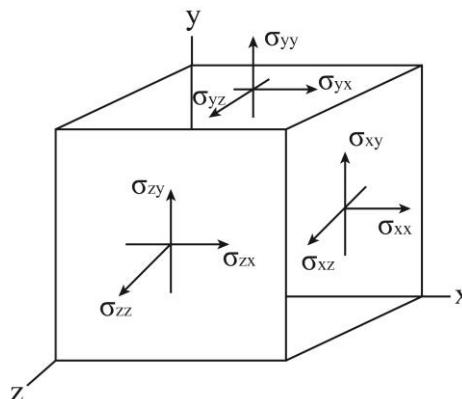


Figure 6.12 Stress tensor and sign convention for stresses (Plaxis bv, 2014).

The orientations of the stresses beneath moving-axle loads are presented in Figure 6.11. The figure shows the changes in orientation and magnitude of the principal stresses along the length of the embankment and perpendicular to it, due to axle loads. The major principal stress directly under the axle loads is vertical and represents the maximum stress that the soil is subjected to. Farther from the load, the principal stresses rotate to the extreme case where the major principal stress lies within the horizontal plane.

To provide a basis to study the influence of speed on the track response, the passage of a train moving at 50 km/h was analyzed for the defined checkpoints; the results are explained thoroughly in this section. The sign convention of stresses used in this analysis is shown in Figure 6.12.

The vertical velocity is a function of time shown in Figure 6.13 for different depths below the track with no stone-column improvement, under the passage of a train at 50 km/h. All track layers are sensible and respond to the passage of the train, but deeper soil layers show lower velocities than the upper layers.

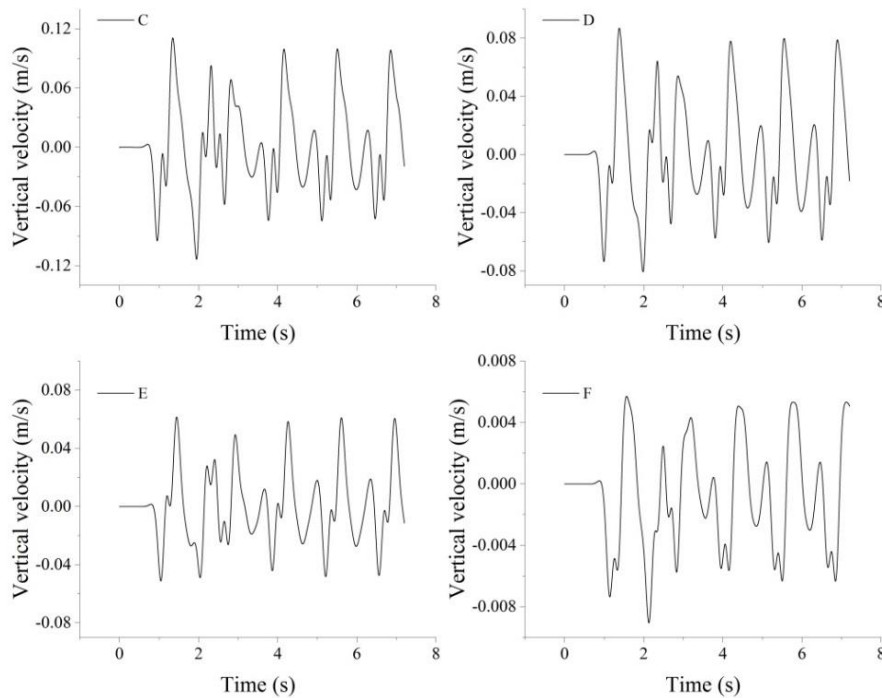


Figure 6.13 Vertical velocity at deformation points C, D, E and F (at depths of 0.7, 2.3, 5.3, and 10 meters respectively). Train speed: 50 km/h; on a track with no improvement.

The evolution of vertical, lateral, and shear stress with loading at different depths was obtained from the model (see Figure 6.14, 6.15 and 6.15). For better comparison of the stress changes at different depths (checkpoints L, M, and N), their values were normalized to the value before arrival of the moving load. The shallowest checkpoint (depth 1.4 m, at L) showed the highest increase in vertical stress – from 28 kPa to 43 kPa during loading. Large differences in the vertical stress between deeper checkpoints (M and N) and the shallow one (L) were evident in the normalized graph. For points at shallow depth, a global increase and decrease of stresses was observed beneath each axle. At deeper levels, the fluctuation was seen in the bogies, which is explained by lower Young's modulus values.

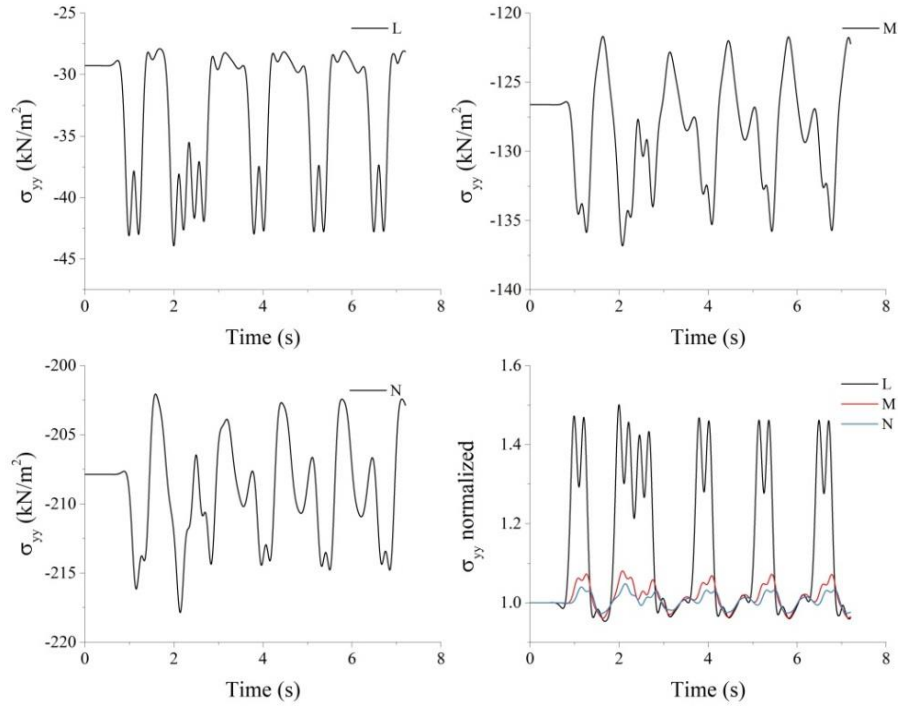


Figure 6.14 Vertical stress at the stress points for L, M and N (at depths of 1.4, 6, and 10 m). Train passage at 50 km/h on a track with no improvement.

Figure 6.15 shows that the change in the lateral stress was much smaller than in case of vertical stress. Similarly, the vertical stress value was higher for shallower depths. However, sensitivity to the depth drastically decreases when depth is high enough.

Figure 6.16 shows that the shear stress did not necessarily decrease with an increase in depth, and its direction changed according to its location in the depth. Increases and decreases in shear stresses for the deeper checkpoints were also examined in the bogies rather than at the level of the axles. Nevertheless, peak to peak of shear stress for the points at depth and near to the loading area were significantly greater than for deeper points. In general, soil elements immediately below the track showed higher stresses than deeper soil elements. As the load approached from a far distance, shear stresses slightly increased before decreasing as the load was close to the considered point. The minimum value was obtained when the first axle approached the considered point in the track. Then shear stress (or shear strain) gradually increased to its maximum value when the first axle had already passed the considered point, and the same process occurred for other axles.

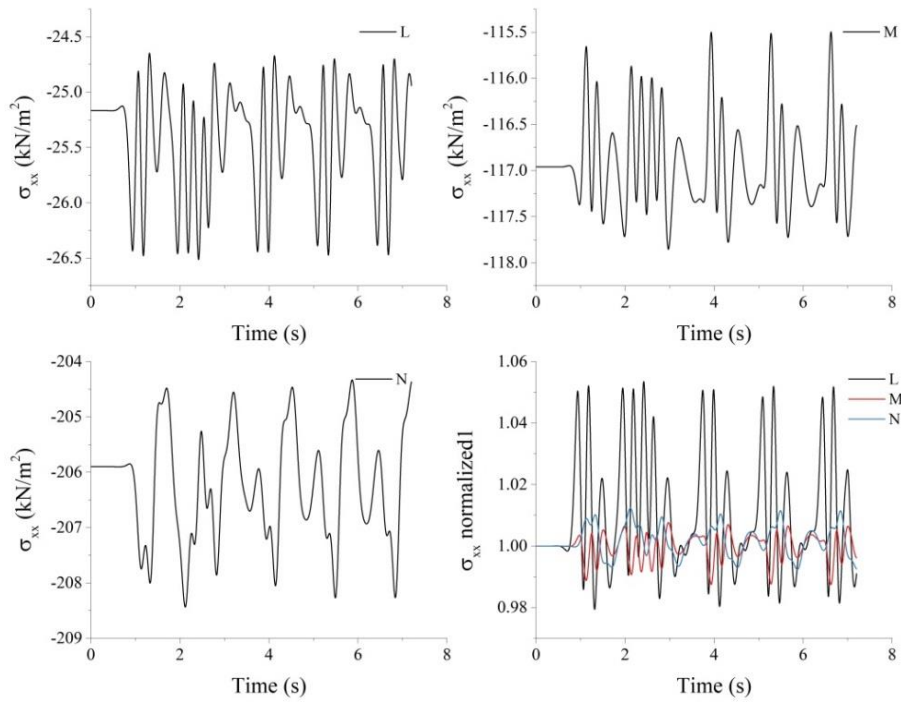


Figure 6.15 Horizontal stress at the stress points for L, M, and N (at depths of 1.4, 6, and 10 m). Train passage at 50 km/h on a track with no improvement.

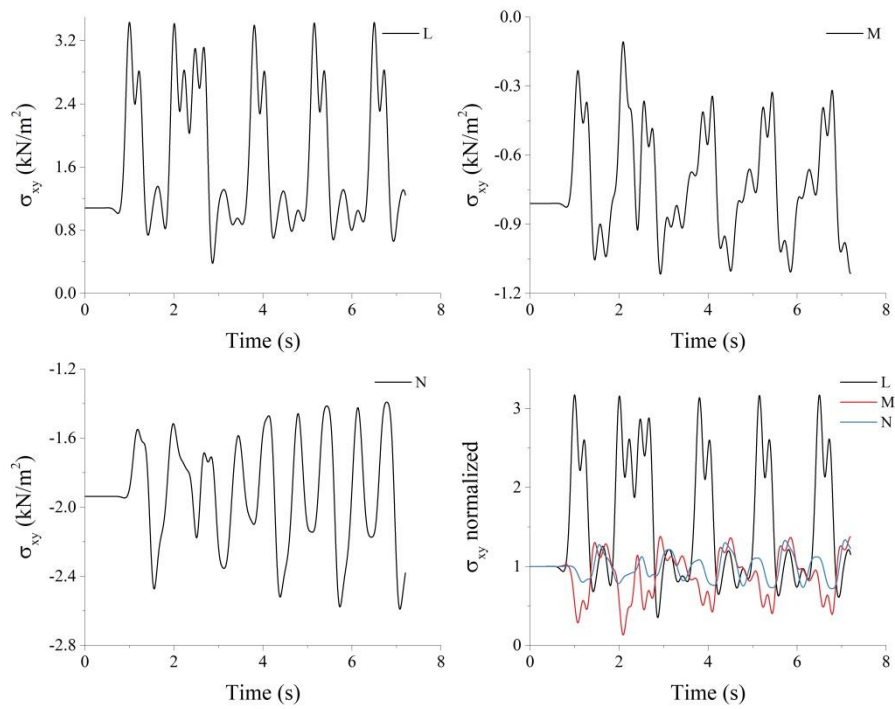


Figure 6.16 Cartesian shear stress at the stress points in depth of 1.4, 6.0, and 10 m for L, M, and N, due to the train passage with speed of 50 km/h on a track with no improvement.

Principal stress axis rotation occurs when the principal stress axes are not aligned with vertical or horizontal axes. When the load arrives at a certain point, vertical stress is maximal and shear stress is minimal. e.g. for a point exactly beneath the load, the highest value of the vertical stress obtained while the shear stress is lowest, therefore, no stress axes rotation happens. This phenomenon is observed for the checkpoint L in Figure 6.14 and Figure 6.18, where at 2 s of passage of the train, vertical stress peaked while the rotational angle was at its lowest. The principal axis rotation angle (α_{xy}) is calculated by Equation 6.3; the results are shown in Figure 6.18.

$$\alpha_{xy} = 0.5 \tan^{-1} \left(\frac{2\sigma_{xy}}{\sigma_{yy} - \sigma_{xx}} \right) \frac{180}{\pi} \quad (6.3)$$

A positive value of shear stress leads to clockwise rotation of the principal stress direction, whereas a negative shear stress denotes a counter-clockwise rotation. A graphic description of the principal stress direction is shown in Figure 6.17.

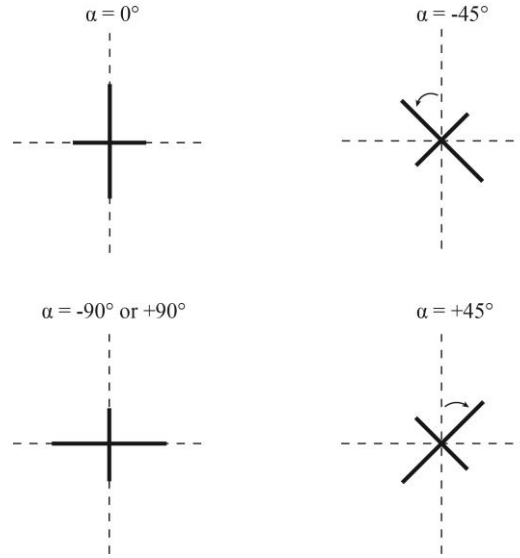


Figure 6.17 Principal stress directions: clockwise rotation is positive and counter-clockwise rotation is negative (Plaxis bv, 2014).

The weakest state - lowest mean effective stress - in the soft soil occurs when rotation of the major principal stresses to the horizontal plane occurs. In addition, interaction between the soft soil layer with adjacent stiff soil causes a concentration of shear stresses to develop, which leads to a higher potential of plastic yielding.

It is useful to define invariants of stress, which are stress measures that are independent of the orientation of the coordinate system. Two useful stress invariants are isotropic stress or mean stress (p), and deviatoric stress (q). the corresponding strain invariants are the volumetric (ϵ_v) and deviatoric (ϵ_d) strains. In case of a 2D plain strain model as used in this section these invariants are defined as follows:

$$p = \frac{\sigma_{xx} + \sigma_{yy}}{2} \quad (6.4)$$

$$q = \sqrt{\left(\frac{\sigma_{xx} - \sigma_{yy}}{2}\right)^2 + \sigma_{xy}^2} \quad (6.5)$$

$$\varepsilon_v = \varepsilon_{xx} + \varepsilon_{yy} \quad (6.6)$$

$$\varepsilon_d = \sqrt{\left(\frac{\varepsilon_{xx} - \varepsilon_{yy}}{2}\right)^2 + \varepsilon_{xy}^2} \quad (6.7)$$

Figure 6.19 and Figure 6.20 present mean and deviatoric stresses which increase when the load approaches, and their maximum values occur when the load is exactly over the considered point. Deviatoric stresses have shown higher increases for shallow depths, whereas at greater depths the change in stresses is smaller. Deviatoric stress has also displayed higher sensitivity to each individual axle of trains than the mean stress. However, the main parameter to control the fluctuation of mean stress, especially for the deeper layers, is the distance between axles rather than individual axle load. This point was discussed in the early chapters (e.g. Section 2.4).

Figure 6.21 presents the results in terms of volumetric and deviatoric strain, which indicate the level of strain in different types of material and depths under passage of a train. Checkpoints at a shallow depth beneath the rail showed higher strain than deeper checkpoints.

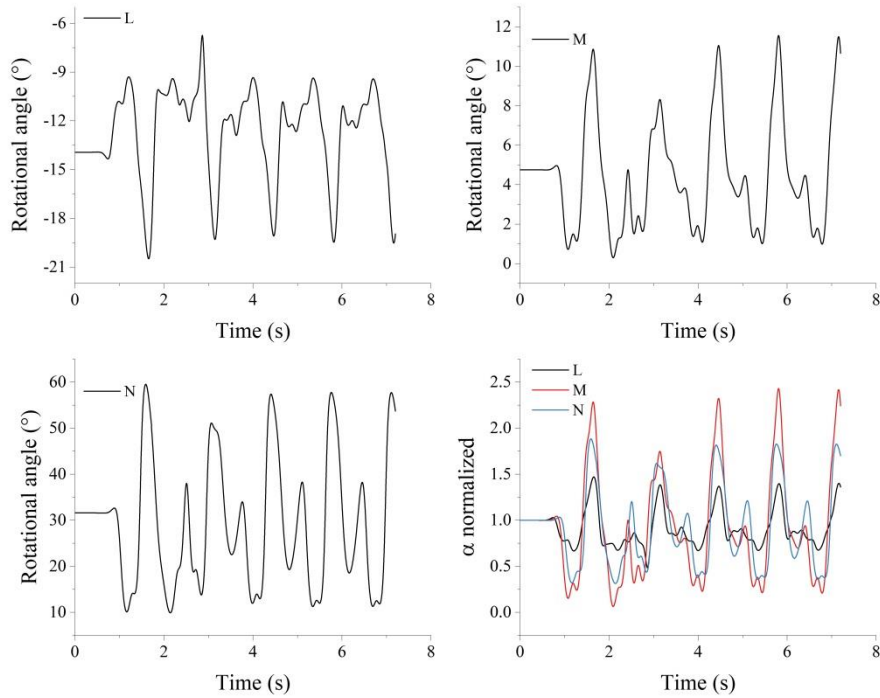


Figure 6.18 Principal stress rotational angle at the points L, M, and N (at depths of 1.4, 6, and 10 m). Train passage at 50 km/h on a track with no improvement.

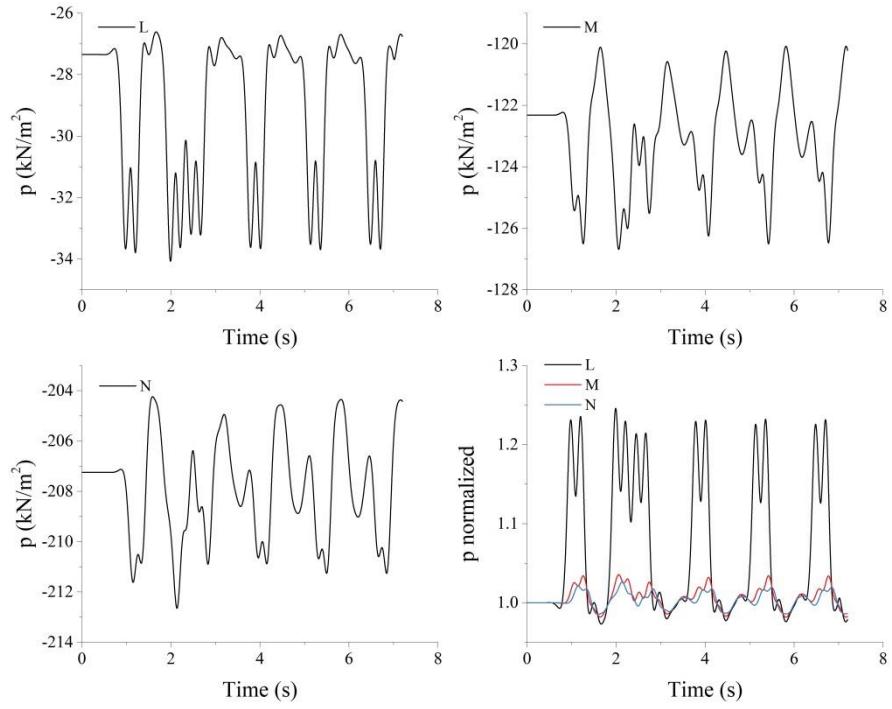


Figure 6.19 Time response of mean stress (p) at the points L, M, and N (at depths of 1.4, 6, and 10 m). Train passage at 50 km/h on a track with no improvement.

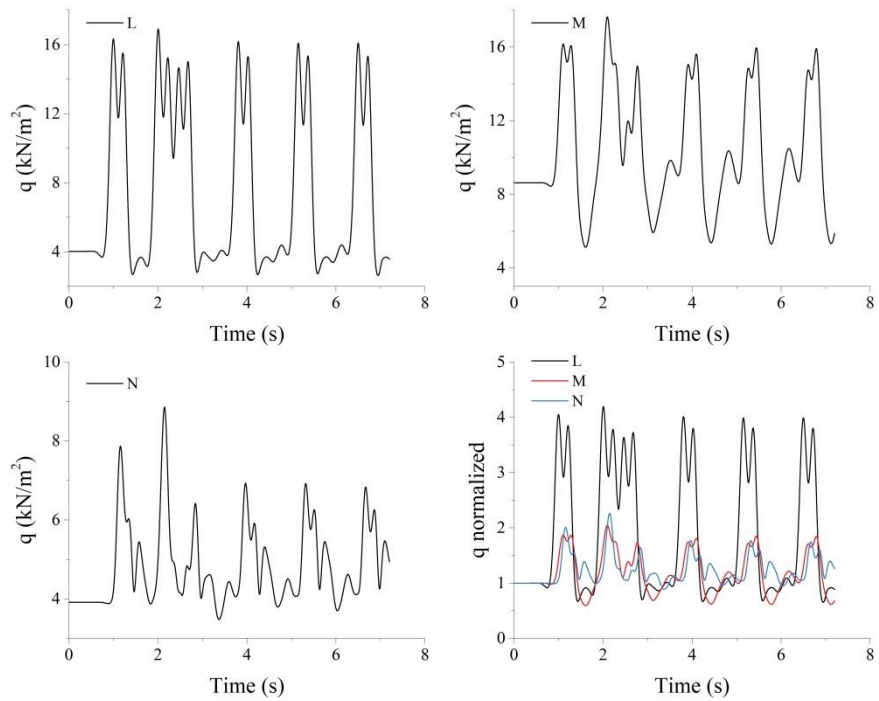


Figure 6.20 Time response of deviatoric stress (q) at the points L, M, and N (at depths of 1.4, 6, and 10 m). Train passage at 50 km/h on a track with no improvement.

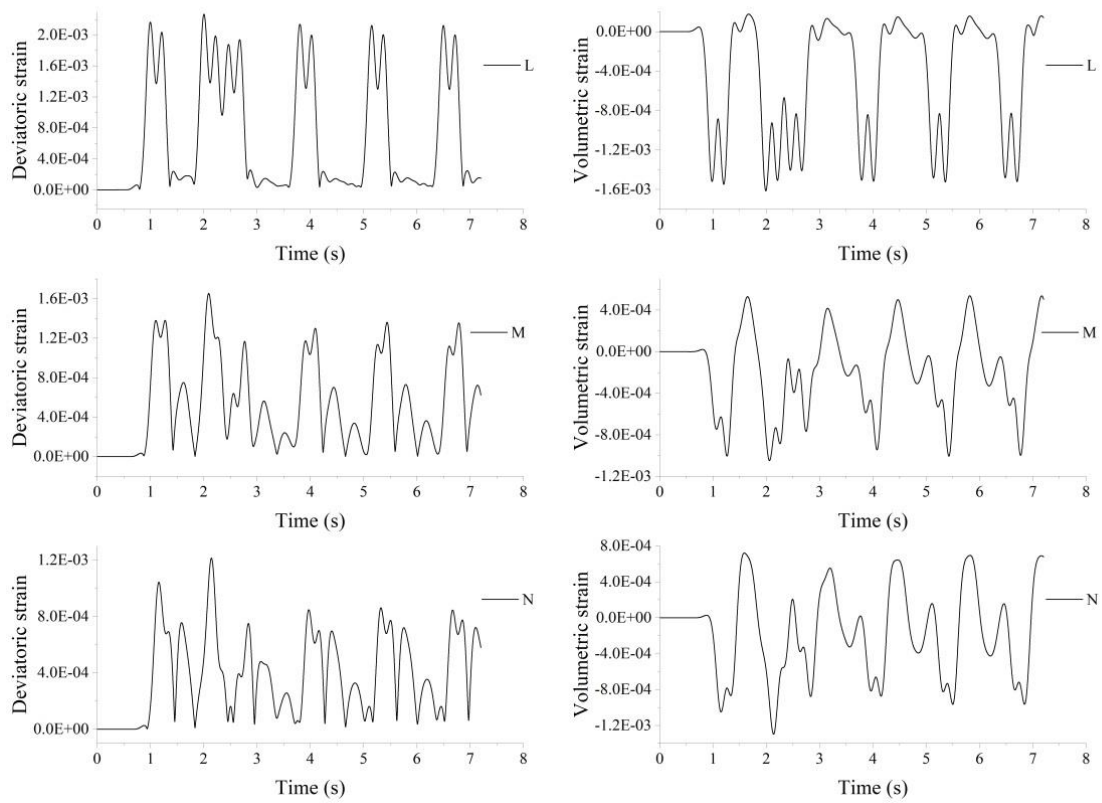


Figure 6.21 Deviatoric and volumetric strain at the points L, M, and N (at depths of 1.4, 6, and 10 m). Train passage at 50 km/h on a track with no improvement.

6.5 Effects of train speed and stone-column length on track response

The influence on the railway track of, firstly, the stone column depth and, secondly, changes in the speed of the trains are assessed in this section. The speeds varied from 50 km/h to 270 km/h. Here, the effective value – also called the root mean square (RMS) – is used to explain and compare the results. In statistics and its applications, the RMS is defined as the mean of the squares of a set of numbers, as shown in Equation 6.8.

$$RMS = \sqrt{\frac{1}{T} \int_0^T x^2(t) dt} \quad (6.8)$$

Numerical simulation was conducted in a plane strain condition, and the equivalent strip method was used for modeling the stone columns (Section 2.10.4). It was assumed that each column had a diameter of 2 m and the columns were arranged in square patterns, with a center-to-center distance of 2 m.

To provide a basis to study the influence of stone column length on the track response, the passage of a train at 50 km/h was analyzed for the defined checkpoints. The results are explained in Section 6.4. The normalized mechanical responses of the track, in terms of RMS, to the train speed of 50 km/h for higher

train speeds (80, 100, 130, 180, 220, 250, and 270 km/h) and different stone column lengths (0, 3, 5, 7 and 10 m) are presented and compared in this section.

Figure 6.22 shows the normalized mechanical response of the middle point of the soft soil layer to minimum speed of 50 km/h for higher train speeds. Figure 6.22 also shows the effect of different lengths of the implemented stone columns. As speed increases, the vertical stress in the middle of the soil layer increases, and its increment is much higher for the case without improvement. For the fully penetrated stone column, no substantial change was observed. Likewise, horizontal stress increased rapidly for higher train speeds, particularly in non-improved ground. However, in all cases a reduction of the effective value of horizontal stress for speeds over 220 km/h was evident. The reduction showed the highest vibration of soil elements in the horizontal direction; in other words, there were large differences between the peak of the minimum and maximum vibration for higher speeds. For lower speeds, this difference was less and not much change was noted in the minimum and maximum values for horizontal stress during the passage of the train. The soil experienced higher vibrations in the horizontal direction, compared with a nearly constant value for lower train speeds.

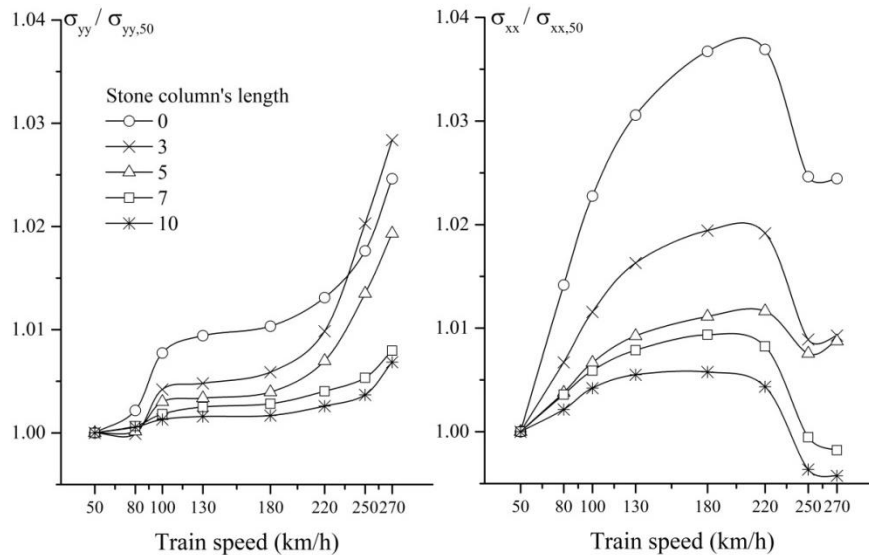


Figure 6.22 Normalized vertical and horizontal stresses (σ_{yy} and σ_{xx}) of the track as a function of train speed, for various lengths of stone columns in the middle of soft soil layer (point M)

Figure 6.23 shows the changes in the mean and deviatoric stress in the middle of the soil layer. The value of the mean stress increased with increasing train speeds. It displayed the least change in case of a 10-m stone column. The analysis also showed that reduction of the effective value of horizontal stress for speeds over 220 km/h had a minimal effect compared with the increment of vertical stress for the same speed. Change in deviatoric stress was almost independent of the length of the stone columns, if they were at least 5 m long, until the train speed exceeded 220 km/h. For non-improvement ground and 3-m stone columns, reduction of q was caused by the simultaneous increase of horizontal stress and decrease of shear stress during the load passage.

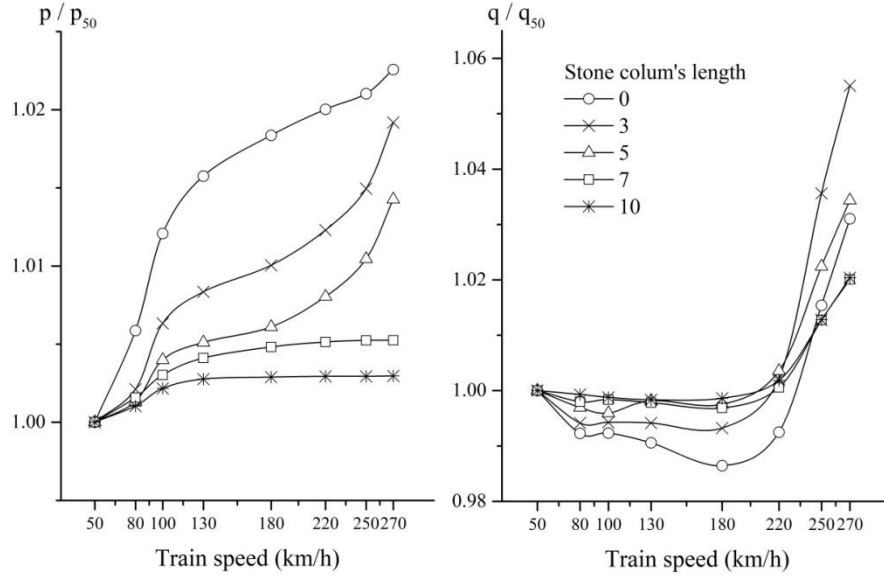


Figure 6.23 Normalized mean and deviatoric stress of the track under increasing train speed, for various lengths of stone columns in the middle of the soft soil layer (point M).

Due to the dependency of the shear stress component on the moving load speed, in such problems a rotation of principal stress axes is expected. In addition, its maximum value depends on the stress condition of that specific point of study, and on the materials. For example, higher rotation might be recorded for the same shear stress level, together with lower vertical and lateral stresses. Increase of the speed has more pronounced impact on the shear stress compared to the vertical stress, and it resulted to higher principal stress rotation angles. Principal stress rotation can be defined as one of the mechanisms leading to higher values of track settlement on conventional railway tracks when train speeds increase.

Generally, the stress path for the first axle is described by an increase in mean stress and deviatoric stress (Figure 6.24). Thereafter, a decrease in deviatoric stress is noted, while mean stress remains constant; finally a decrease in mean stress occurs. The same cycle is repeated for all other axles during the passage of the train. Figure 6.24 also shows that by increasing the depth of the stone columns, this cycle becomes smaller and smaller, that means the changes in mean and deviatoric stress during the passage of a train decrease. The smaller cycles also reduce the chance of reaching the Mohr-Coulomb failure criterium. The mean stress is less sensitive to train speed in comparison with deviatoric stress, but is affected by an increase in lateral and vertical stress at the same time.

Stress-path analysis was used to quantify the influence of the stone column length on the slope of the stress path. The results are presented in Figure 6.24 for the point in the middle of the soft soil (point M). A critical state line (CSL) with slope M_{cs} according to Equation 6.9 represents Mohr-Coulomb failure criterium in compression (Ferreira, 2013). The CSL can be defined as a state when the soil continues to deform without any variation in effective stress and volume. It is described by the friction angle of the soft soil, which equals 21° .

$$M_{cs} = \frac{6 \sin \phi}{3 - \sin \phi} \quad (6.9)$$

Gradually, with increases in train speed, the stress path for non-improved ground reaches the CSL, particularly for speeds over 220 km/h, and crosses the line. However, adding depth to the stone columns brings the stress path to a safe distance from the line; this benefit is obvious for higher speeds.

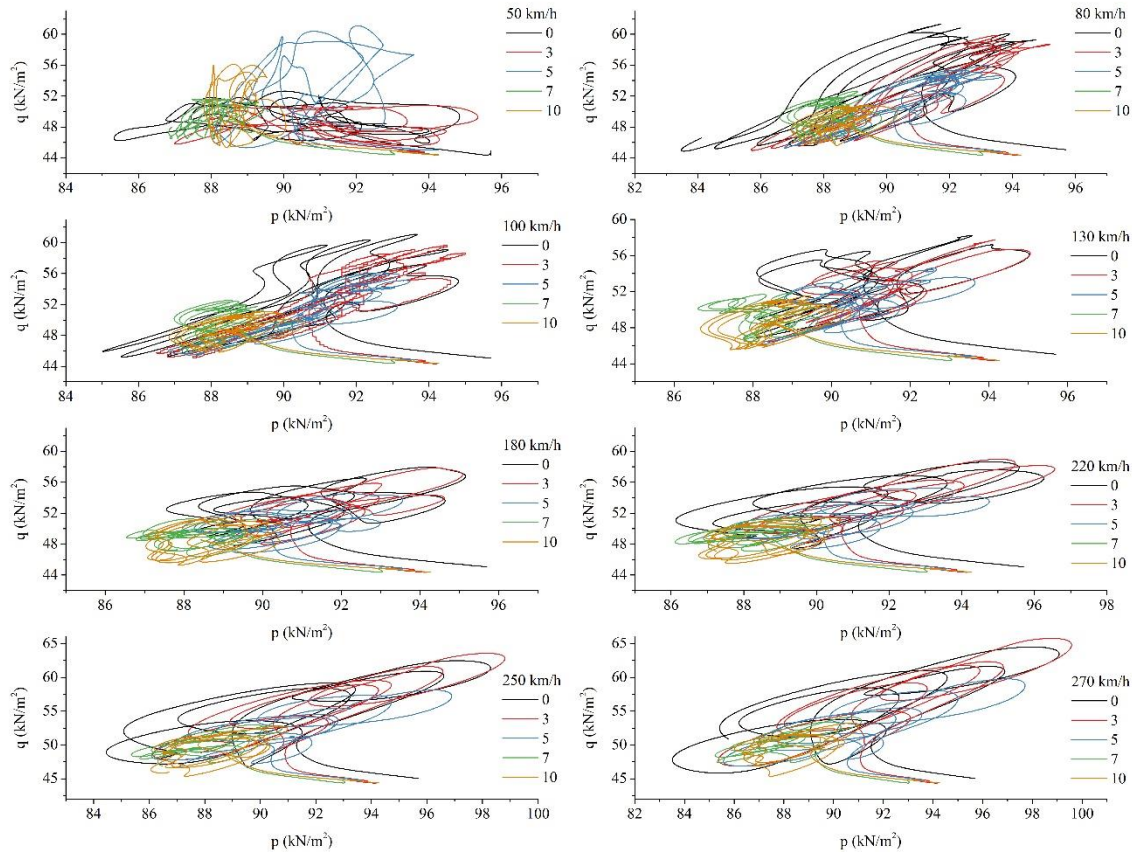


Figure 6.24 Change in stress path for different train speeds (50, 80, 100, 130, 180, 220, 250, and 270 km/h), after implementing stone columns of various lengths (0, 3, 5, 7, and 10 m).

Introducing stone columns to the model increases the average Young's modulus for the whole system. Based on the deviatoric stress results presented in Figure 6.25, changes in Young's modulus can be checked by using the initial results from Equation 6.10 (Cunha, 2013). The comparison shows that an increase of Young's modulus for short stone columns depends on train speed, whereas a fully penetrated stone column leads to a higher Young's modulus regardless of train speed. No clear trend emerges in relation to the volumetric response. However, change in the train speed shows minimum influence on fully penetrated stone columns, whereas shorter columns show dispersal behavior according to changes in train speed. One explanation relates to plastic deformation due to the assumption of isotropic compression stress in the FE model. Materials naturally show higher compaction due to increased confining pressure; however, this pattern can reverse when plastic strains develop due to isotropic compression stress. In other words, more dilatational behavior can be seen for more highly compacted material because of the development of plastic strains.

$$E \approx \frac{q}{\gamma_s} \quad (6.10)$$

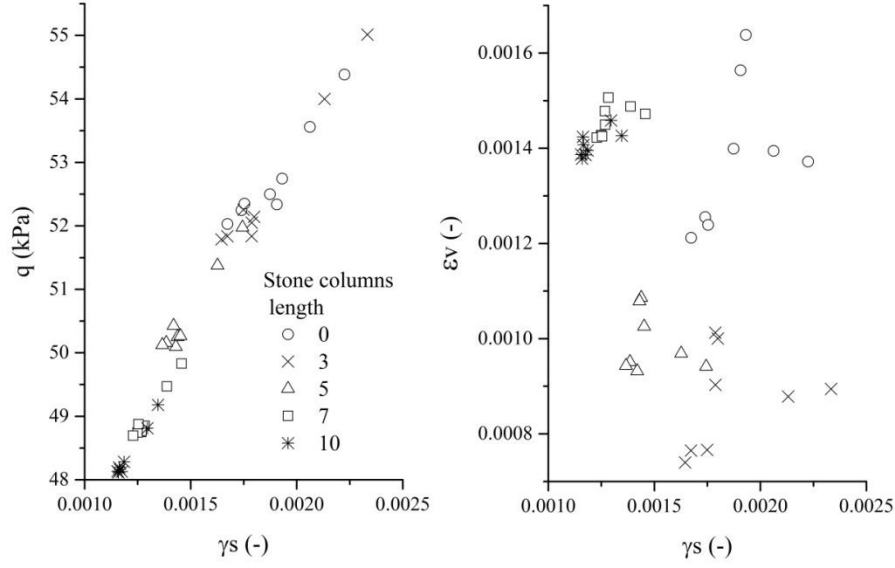


Figure 6.25 Deviatoric and volumetric responses for stone columns of differing lengths (0, 3, 5, 7, and 10 m).

In this study, no change in the value of the train load was analyzed and it was kept constant. Only the dynamic influence of changes in speed was examined, not the train-track dynamic interaction. Due to the dependency of volumetric response on the load magnitude, altering the train speed had minimal effect on it. Changes in train speed had the greatest effect on shear stress and deviatoric stress and strain. Nevertheless, volumetric response was strongly affected by introducing the stone columns to the model under conditions of constant speed; as the stone column length increased, less variation in the volumetric response was observed.

6.6 Non-linear response of the railway track

The behavior of soil is non-linear and irreversible, and soil stiffness increases with increasing depth due to higher confining stress. Using the linear elastic model as a constitutive model for increases in soil depth leads to greater displacement values because of the lower stiffness. This condition is not physically possible; hence, the advanced Hardening Soil small-strain (HS-small) constitutive model was used to more accurately capture the soil behavior.

The goal was to study the first train passage on the railway track, as this is when materials develop the highest deviatoric and volumetric strains. The non-linear mechanical responses of the track for different conditions, including changes in train speed and in the lengths of stone columns, were analyzed. The results for the stress-strain and shear response of soil are presented here. Figure 6.26 and Figure 6.27 show the maximum vertical and lateral strains along the stone column beneath the loading area for different lengths of stone columns (0, 3, 5, 7, and 10 m) under the passage of a train, at speeds of 50 km/h,

130 km/h, and 250 km/h. The maximum vertical and lateral strains were higher for ground with no improvement, with the vertical strain being higher than the lateral strain, especially at lower train speeds.

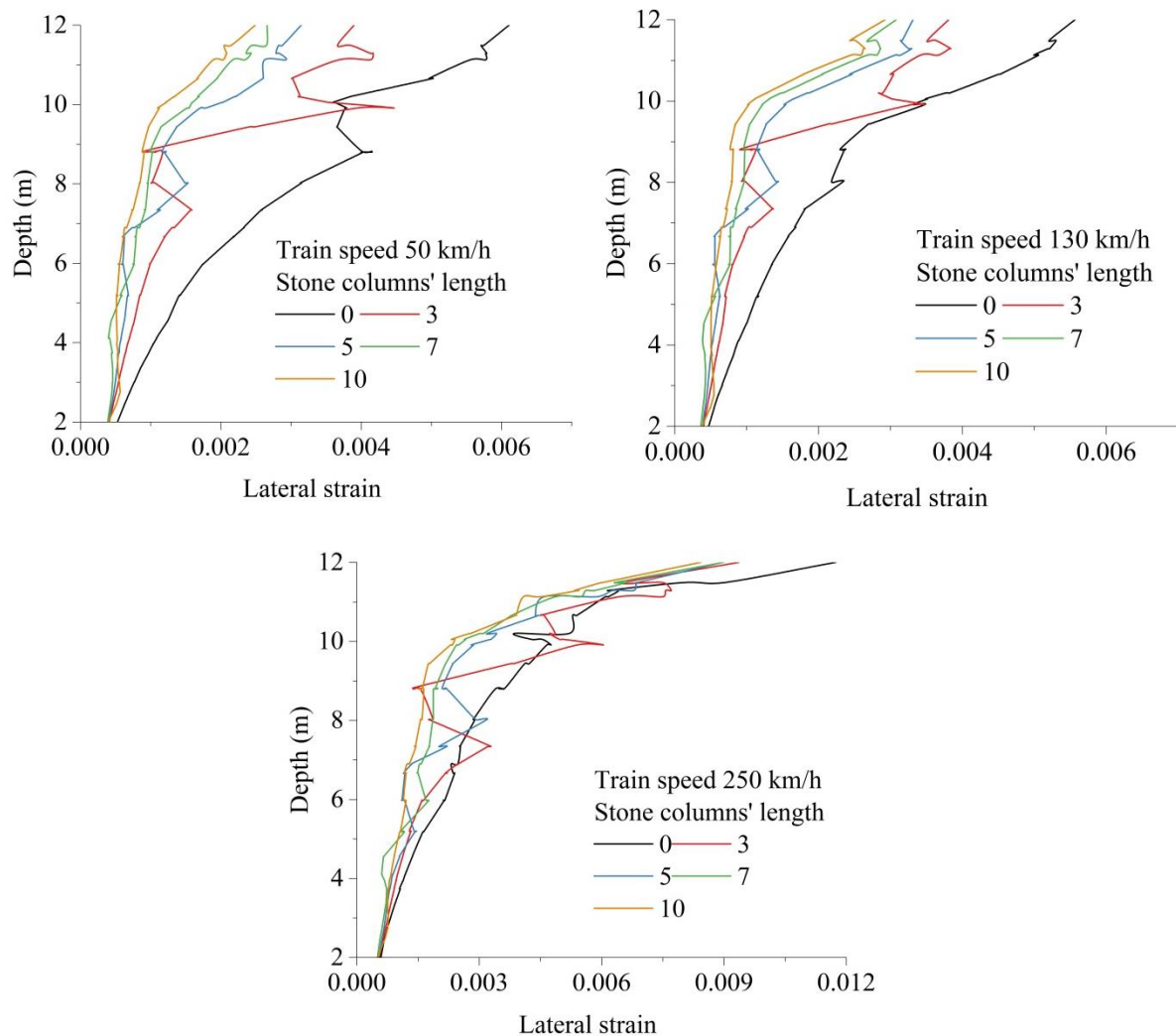


Figure 6.26 Changes in lateral strain along the stone column beneath the loading area, for three train speeds (50, 130, and 250 km/h).

Application of even the short stone columns led to a smaller lateral strain level. However, increased train speeds reduced this effectiveness to a level equal to that of non-improved ground, for a shallow depth near the loading area. Nonetheless, reduced strain levels at greater depths were clear. An abrupt reduction in lateral strain at a depth of 3 m for the shortest stone column (3 m) showed some degree of fixity at the bottom of the column, which was the direct result of increasing the confining stress at greater depths. It also shows the possibility of punching the stone column into the soft soil and creating ended bearing condition in that specific section.

Regarding vertical strain, the length of stone columns did not play an important role; all lengths reduced the strain to almost the same degree. However, the benefit of stone columns for controlling the vertical strain decreased as the train speed increased.

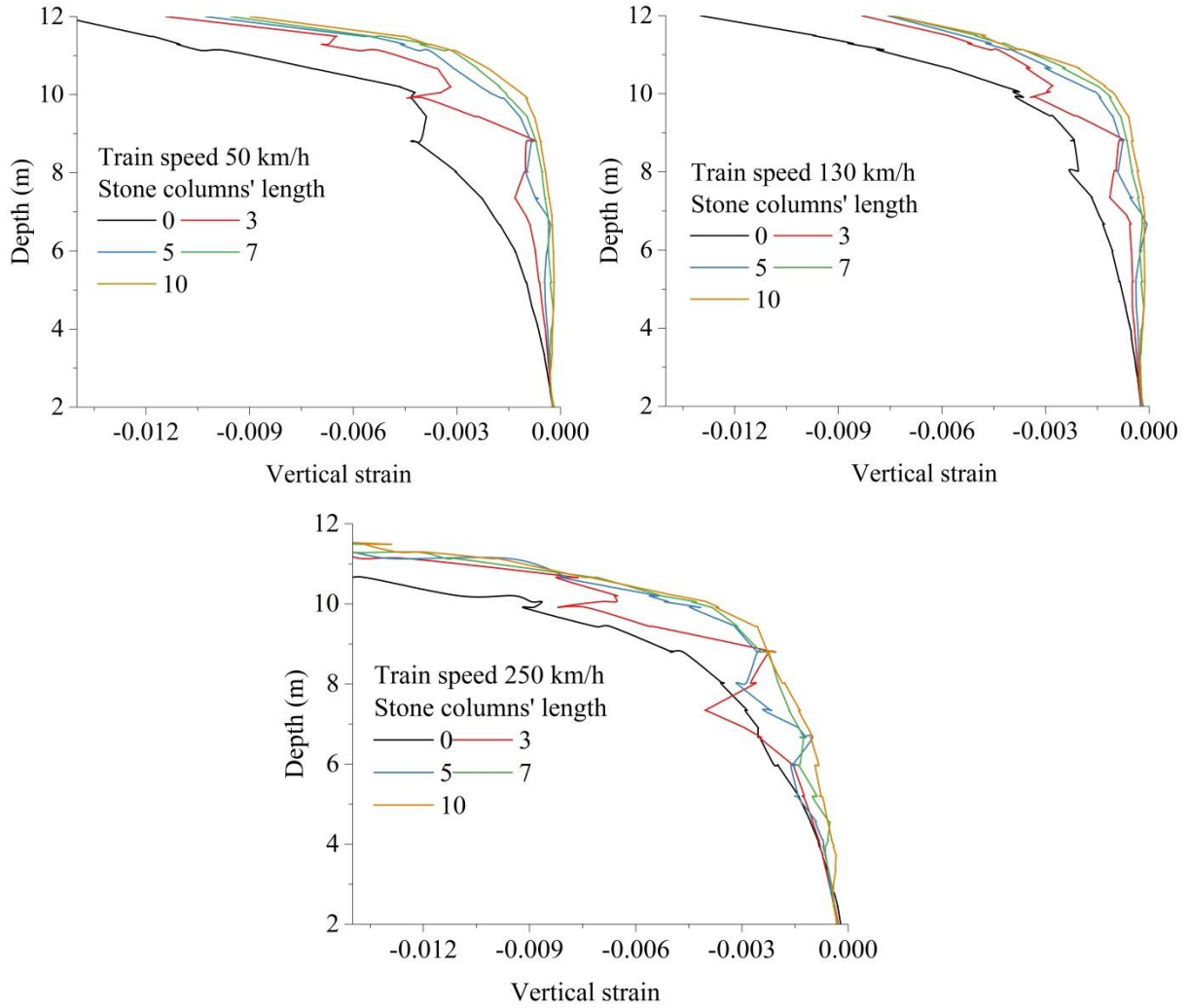


Figure 6.27 Changes in vertical strain along the stone column beneath the loading area, for three train speeds (50, 130, and 250 km/h).

Figure 6.28 shows the stress path after applying the advanced constitutive model. The results can be compared with the similar graph shown in Figure 6.24 which was obtained for the linear elastic–perfectly plastic model. For the present constitutive model (HS-ss), the behavior of soil during loading was also captured due to the volumetric and deviatoric strains. Volumetric, deviatoric, and shear responses of the improved ground under the passage of three train speeds (50, 130, and 250 km/h) at a depth of 1.5 m in soft soil (Point L) are presented and explained in this section. It was expected that the stress path would touch the CSL and this is viewed as perfect plastic behavior. The stress path also reached the characteristic state line, indicating an increased volume and a movement from contractive to dilative behavior in soil. This undesirable phenomenon can lead to high settlement due to the rise in strain levels. Stone columns – particularly fully penetrated columns – decrease the evaluation of the stress path and create a safe distance between the path and the CSL.

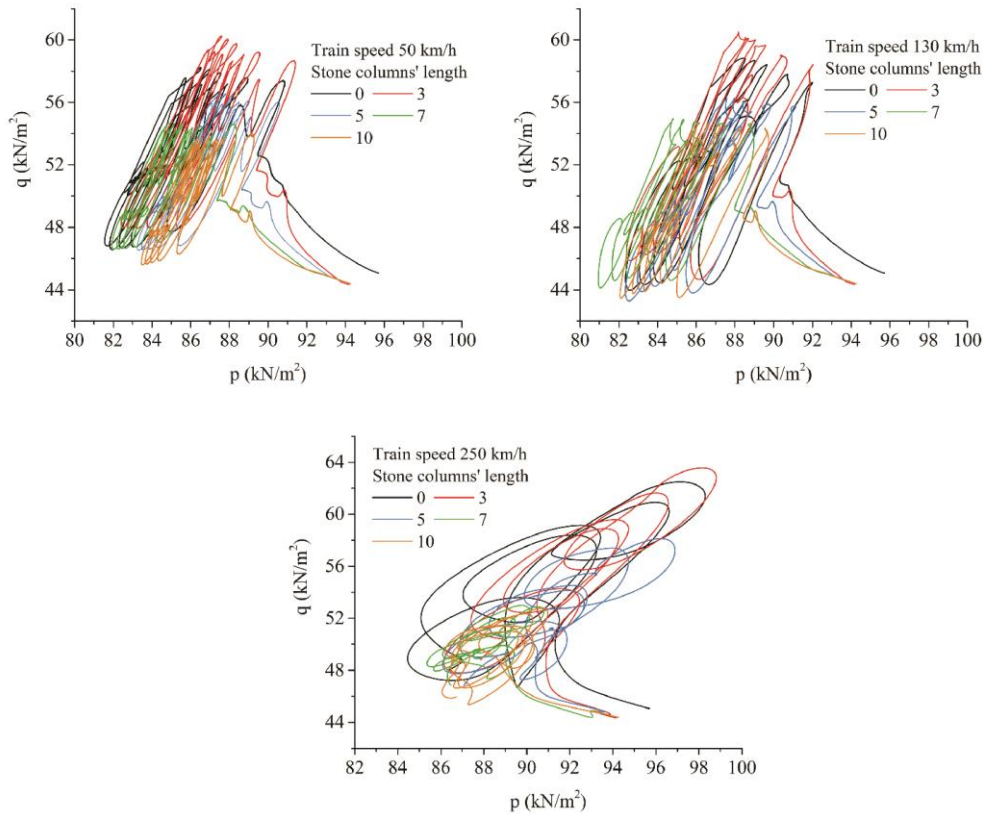


Figure 6.28 Effect of the length of stone columns (0, 3, 5, 7, and 10 m) on the stress path, for three train speeds (50, 130, and 250 km/h).

Figure 6.29 shows that the first axle (or bogie) is responsible for most of the volume change, because the passage of the first axle is the main source of plastic deformation; the following axles only slightly increase the volumetric strain. As train speed increases, the level of volumetric strain induced in the soil is raised. Nonetheless, the use of stone columns, regardless of their length, substantially decreases the volumetric strain. Regarding train speed, an increment in the residual mean stress for higher train speeds was observed and was related to the volume reduction, which implies higher compaction and stiffer material behavior. The maximum values of both mean stress and volumetric strain were highest for 250 km/h, especially the volumetric strain during the first axle passage.

For a specific deviatoric stress, higher strain was obtained for non-improved ground, whereas application of stone columns – regardless of their length – led to a smaller level of strains in the soil. For either short or long stone columns, the obtained strain was nearly unique for the same range of deviatoric stress. However, increases in train speed resulted in wider differences in the strain level associated with stone column length. In other words, less strain was generated in the soil from the passage of a train at high speed if the stone columns were long, within the same level of deviatoric stress. Due to volume reduction and soil stiffening, residual deviatoric stress and strain were higher for 250 km/h compared with lower speeds. Maximum deviatoric strain was magnified for faster train speeds.

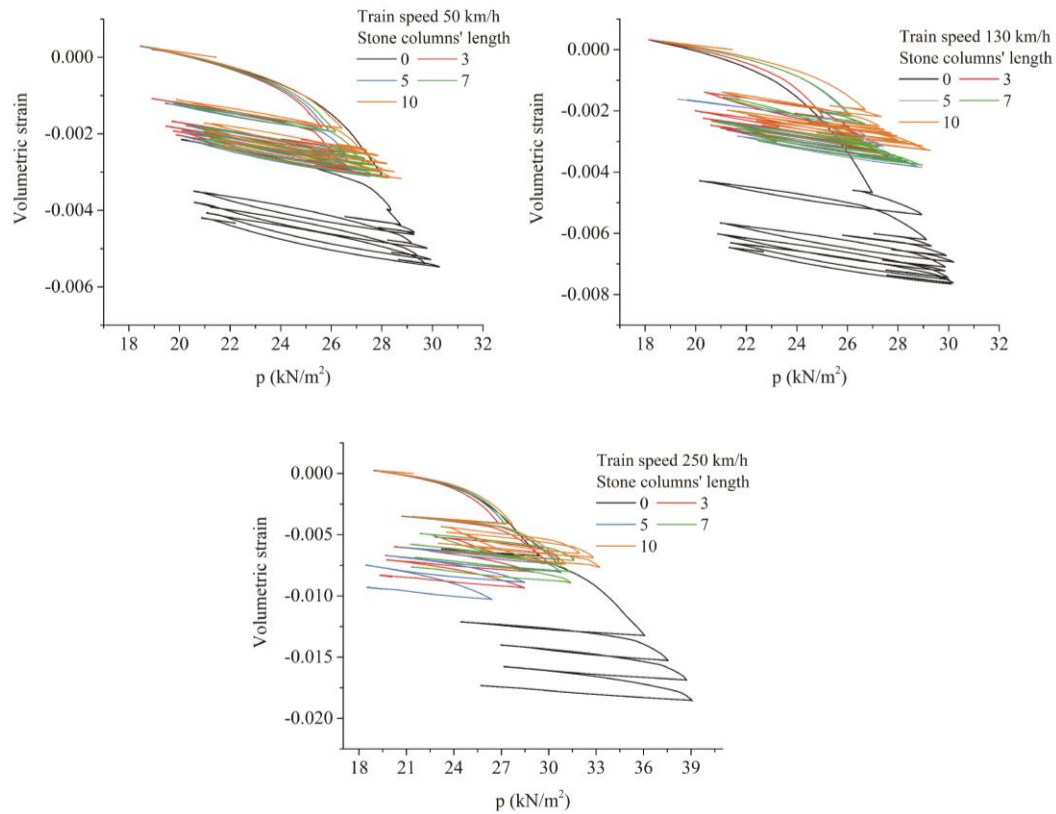


Figure 6.29 Effect of length of stone columns (0, 3, 5, 7, and 10 m) on volumetric strain, corresponding to mean stress for three train speeds (50, 130, and 250 km/h).

In general, an increase in train speed led to higher strains and stresses in the soil. Furthermore, the level of strain and stress was much lower after application of even the short stone columns. However, deviatoric strain was affected more than volumetric strain by changes in the column length. Change in speed affected the stress-strain response of the soil by increasing the maximum mean stress and strains during the passage of trains at higher speeds.

The shear response can be shown in the plane of shear stress and shear strain level, as illustrated in Figure 6.31. The value of shear strain increased to higher levels after passage of the second axle, and it continued as the other axles passed by because of material softening behavior. Figure 6.31 compares the shear response for various lengths of stone columns under passage of a train at various speeds, and clearly higher speeds led to higher shear strain. As mentioned earlier, the first axle generates the highest increment in shear strain and its value is greater for trains travelling at high speed. Shear strain decreased regardless of the length of stone columns, although shear stress remained constant in all improved and non-improved conditions. It should be noted that variation of stresses during the passage of a train causes a large angle of principal stress axis rotation.

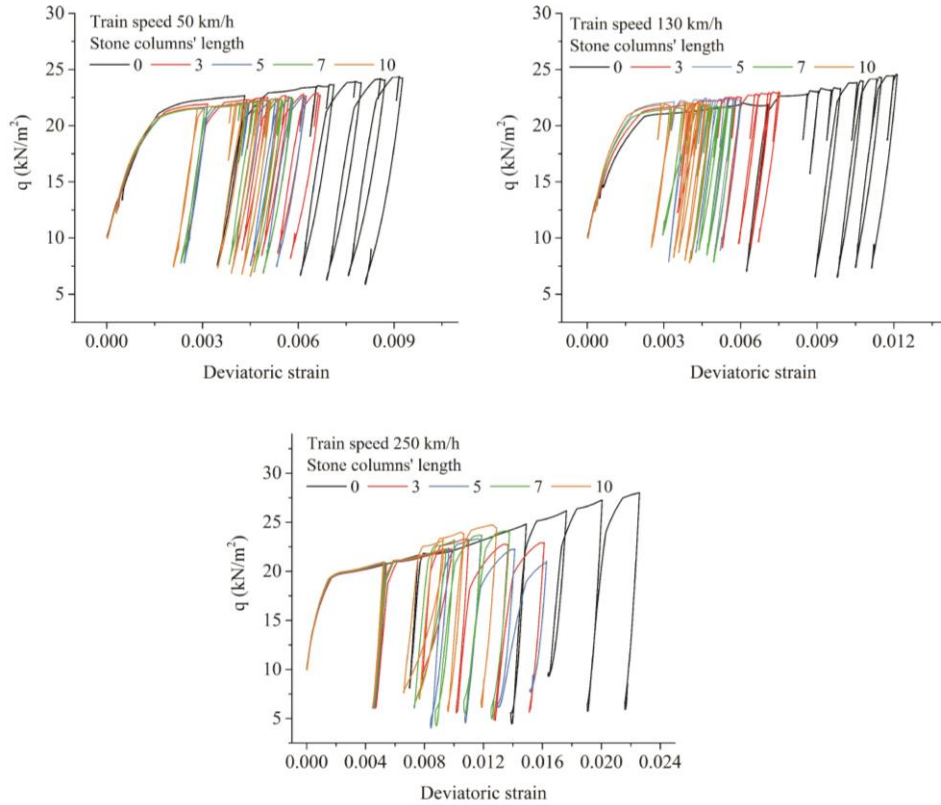


Figure 6.30 Effect of the length of stone columns (0, 3, 5, 7, and 10 m) on deviatoric response, for three train speeds (50, 130, and 250 km/h).

For all cases, the observed increase in stresses under the passage of train loads illustrates the hardening behavior of the soil and an increase in stiffness due to plastic strains. Higher levels of stress resulted as the train speed increased, and due to the volume reduction an increment in vertical settlement was observed. However, increases in the mean and deviatoric stresses also increased the odds of dilative behavior in the soil, which – as shown – can be controlled by using stone columns.

In all results and regardless of the train speed, the importance of the very first cycle – which may be an axle for shallow depth or a bogie for deeper depth – was evident. Preloading a track with a very low train speed initially is likely to reduce the cumulative stress and strains of later loadings at higher speeds. In practical terms, this condition can be created after track maintenance by limiting train speeds to minimal speed for the first few passages.

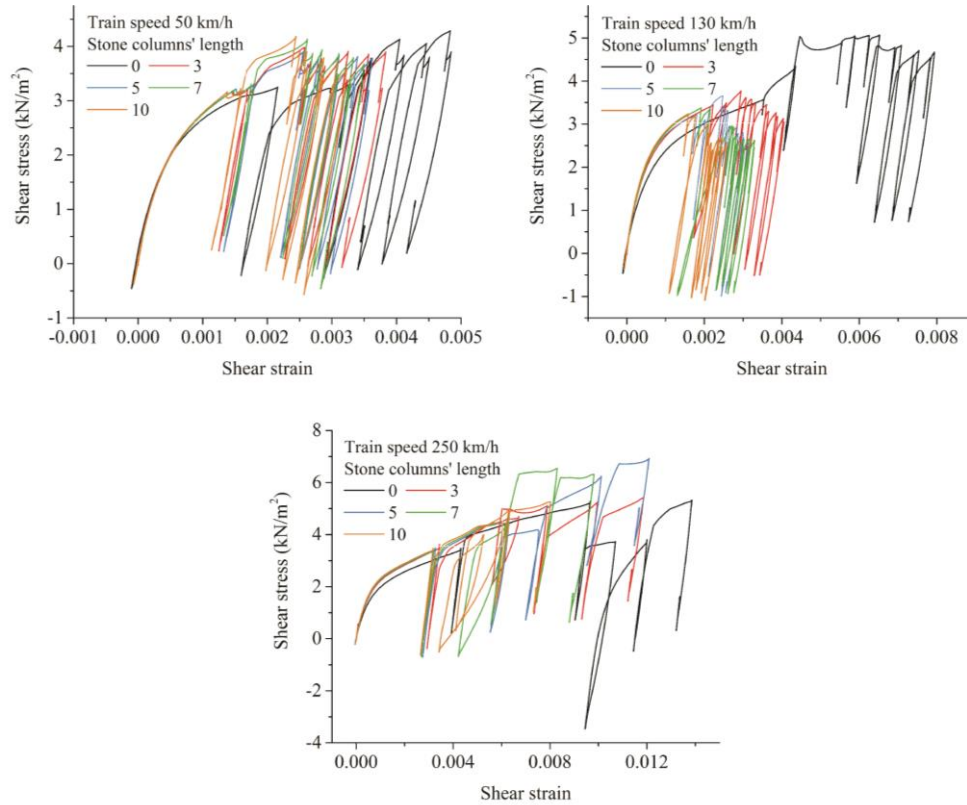


Figure 6.31 Effect of the length of stone columns (0, 3, 5, 7, and 10 m) on shear response, for three train speeds (50, 130, and 250 km/h).

6.7 Application of geosynthetics

In all previous calculations, the track was assumed to have been constructed directly on soft soil without any sand blanket or geosynthetic material. However, in common applications, a geotextile or geogrid is placed between the subgrade or sub-ballast and on top of the stone columns. Moreover, in some cases geotextile is used to cover the shaft of the stone columns, which are called encased stone columns.

In this section, the effect of applying one layer of geosynthetic material is investigated. The material, Stablenka 500/100 with an ultimate tensile strength of 500 kN/m (Alexiew and Raithel, 2015) was placed beneath the track as a basal reinforcement. In FE modeling the geotextile was treated as linear elastic with an input axial stiffness of 5000 kN/m and negligible flexural rigidity. Interface elements simulating the interaction between the geosynthetic material, subgrade, and soft soil (with a strength reduction factor of 0.75 and 0.67 respectively) were included. The effect of basal reinforcement of the track was analyzed for different lengths of stone columns (0, 3, 5, 7, and 10 m) but only two train speeds (80 and 250 km/h). Figure 6.32 shows that implementation of the geosynthetic basal reinforcement reduced the horizontal displacement regardless of the train speed and stone column length. However, the reduction was slight. Nonetheless, it would have a greater effect under an increased number of train passages; also, at higher levels of strains the geosynthetic role would be more dominant.

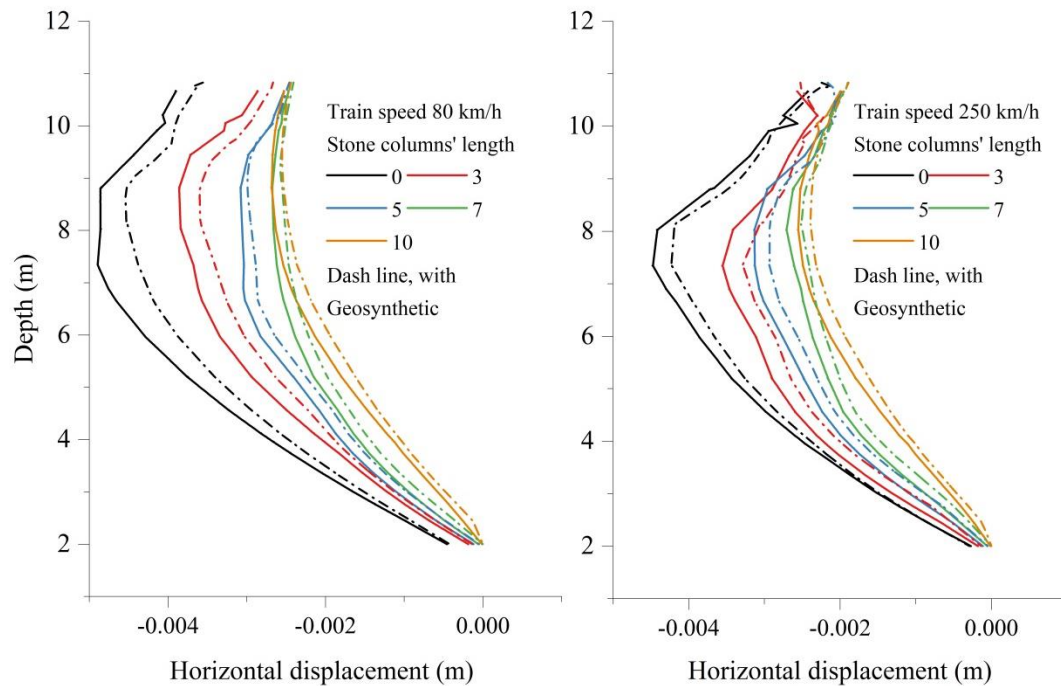


Figure 6.32 Effect of basal reinforcement on horizontal displacement along the stone column at depth.

6.8 Failure mechanism of stone columns

A railway track system constructed on ground improved by stone columns creates a flexible loading condition over that area. Due to the weak foundation, soil tends to move laterally outward to the sides. This problem – called “spreading” occurs for soft soil that is not reinforced by stone columns, and it leads to greater settlement. In groups of stone columns, if adjacent columns cannot provide enough lateral resistance then the columns might experience “bulging”. Bulging refers to an increase in the mean stress in the column, without prevention of radial expansion by adjacent columns. At the edges of the flexible loading area, “bending” occurs; this refers to a lateral deformation of the stone column, especially in slender columns. When a stone column is subjected to a high stress ratio with low lateral restraint, a diagonal shear plane appears, which is due to an insufficient increase in the mean stress. Normally, an overall failure mechanism results in concentration of deformation along the shear plane. However, localization of stresses in the columns alone, and material responding as a single material (not in combination with the surrounding soil) can also lead to such failure. Finally, inadequate skin friction along the stone column length and the surrounding soil can lead to a significant load being transmitted to the base of the column. This means penetration of the column into the soft soil. However, this condition occurs only in stone columns that do not extend to the dense strata or bedrock.

In this study, various modes of deformation were observed, depending on the geometric configuration of the stone columns. The train speed appeared to be irrelevant to the failure mechanism. The main type of failure was bulging in the middle stone column, which was observed for both short and long columns. The bulging was concentrated in the upper region of long columns; short columns tended to bulge and

bend outwards along the entire column length. In short stone columns, contrary to expectation, negligible vertical penetration into the soft soil occurred, especially for low train speeds. The penetration was related to short passage times of trains, as well as little lateral resistance – which makes it easier for columns to spread laterally rather than penetrating downwards. By increasing the column length, the columns tended to bend rather than to separate, due to the higher stiffness of the surrounding soil. This behavior was a direct effect of increment in the soil depth (higher confining stress). Short columns at the edges of the track still showed a potential to move away from the loading area. In the case of fully penetrated stone columns, due to the extension of the column's length to the dense body, a sort of fixed end is provided, which prevents the column from spreading. However, it raises the chances of columns bending, particularly among the outer columns that are not encircled by other columns. It should be noted that in all cases, stone columns underwent shear plane failure, which can be interpreted as an overall failure mechanism in the improved ground system.

In general, groups of stone columns introduced in the model showed a combination of all failure modes regardless of being short or fully penetrated. The failure mechanisms mostly depended on the columns' location, corresponding to the load area, rather than train speed. Failure modes of either long or short stone column groups under a wide railway track load are shown in Figure 6.33.

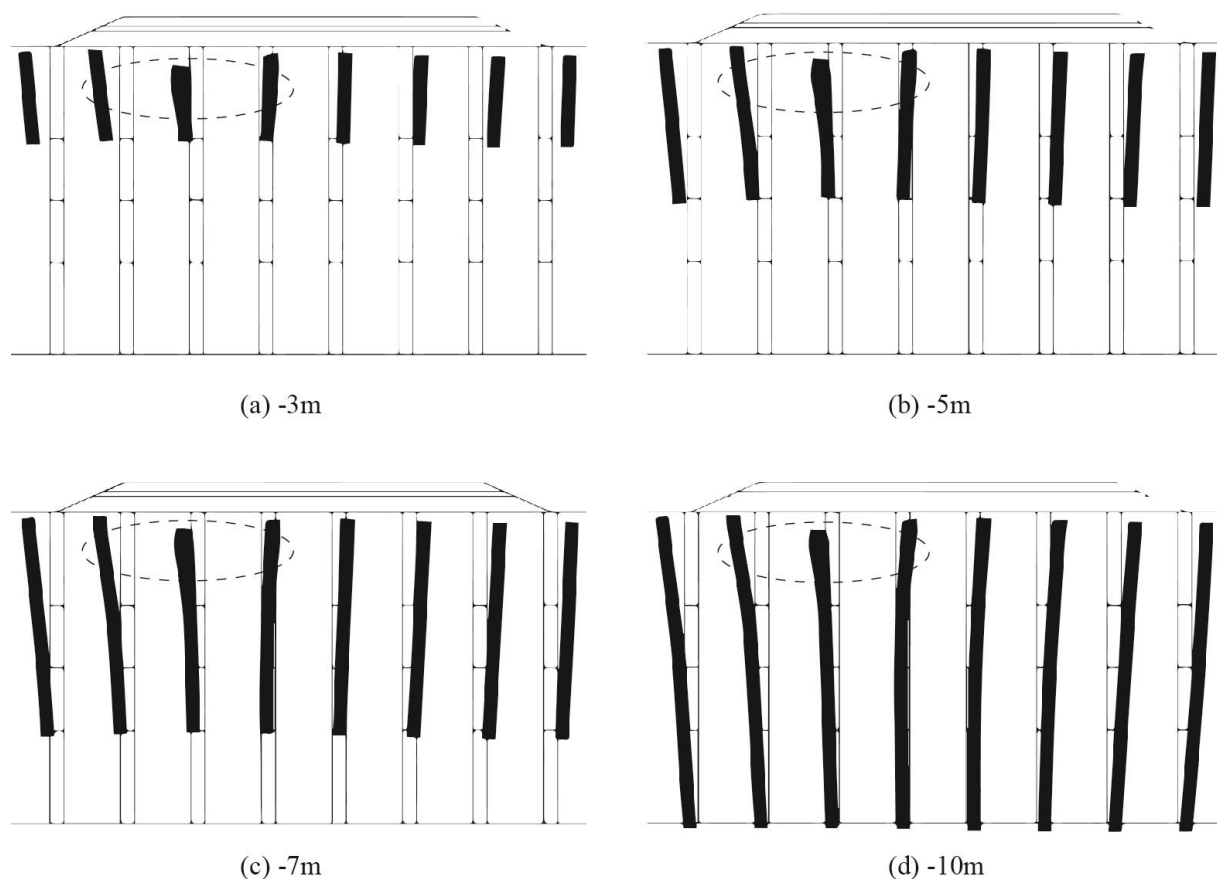


Figure 6.33 Failure mechanism of different lengths of stone columns (3, 5, 7 and 10 m), under passage of a train travelling at 250 km/h. The ellipse shows column failure through bulging or shear plane (extended to the outer columns), where the other stone columns failed due to lateral spreading, or became bent. Scale: 1/50.

7 Summary and Conclusions

The overall aim of this thesis was to study the effect of installing stone columns of different lengths below a railway track, under various train-speed conditions. The finite element (FE) method was utilized to analyze the response of a railway track supported by stone columns, by varying the train speed as well as the stone column length. Partial conclusions have been presented throughout the thesis. The main and final conclusions are outlined in this section.

For the sake of computational cost and practical ease of use, a choice was made to simplify a 3D geotechnical problem to a 2D plane strain model. However, conversion of fully 3D phenomena, namely passage of a train and the discrete arrangement of stone columns to a simple 2D model, called for numerical and analytical preparatory steps.

Concerning the simulation of the train load, a procedure for creating a moving load in a 3D FE model was used. In general this model can be used for all moving load problems on finite discretized domains. However, for a 2D simulation, the Zimmermann model was modified with Eisenmann dynamic amplification factors, which included the effect of dynamic loads in loading conditions. The Cone's theory was used to provide a foundation condition for the loading model. To ensure the accuracy of the simulated train load in the 3D and simplified 2D models, three field measurements were used for validation. The presented 2D model showed good agreement with the field data and had a much shorter computational time, but it displayed limitations when train speed reached the critical or Rayleigh speed thresholds. Nonetheless, the results showed that the proposed 2D train load model was a good alternative to the costlier 3D model.

Regarding stone column modeling, firstly, the unit cell concept in an axisymmetric condition was used to study the main concerns about stone columns, namely settlement and consolidation. An extensive parametric study was conducted on the influential parameters, including area of replacement, friction angle of materials, applied load, and modulus ratio, for different lengths of stone columns. The results showed that regardless of the length of stone columns, implementing them can reduce the settlement and excess pore water pressure; significantly, as the column depth increases a larger reduction can be obtained. A fully penetrated stone column performs better than a shorter column. Nonetheless, changes in those parameters (for a specific length of stone column) had little effect on the column's performance, apart from the area replacement ratio and applied load. The area replacement ratio had the main effect on overall settlement for both short and long stone columns, and its influence was more marked for fully penetrated columns. By contrast, when the applied load was increased, plastic strains developed in the soil and the columns, resulting in higher settlement – regardless of the length of the stone columns. Changes in the internal friction angle had a negligible effect on short stone columns and a minimal effect on fully penetrated columns. The modulus ratio also had a negligible effect on the reduction of settlement.

In sum, increases in the area replacement ratio and column length had a positive influence on the settlement performance of stone columns. The influence of column length was greater for smaller areas

of replacement; if the area of replacement was increased, shorter columns can achieve the benefits of fully penetrated columns.

Another important factor was spacing between the stone columns. To study its effect, the area of replacement was kept constant while the spacing was varied. Numerical analysis showed that changes in the space between stone columns (keeping the area of replacement constant) had little impact on final settlement, for both short and long stone columns. This finding again shows that the area of replacement played the main role in controlling the settlement and this is in accordance with Priebe approach.

As part of converting a 3D problem to a 2D problem, an approach was needed to model discrete cylindrical stone columns in a plane strain condition. To model a group of stone columns in plane strain, the equivalent strip model was used. This simple model was used to study the influence of lateral earth pressure on the behavior of improved ground for various lengths of stone columns under an equal induced settlement. An increase in the coefficient of lateral earth pressure was associated with a slight increase in stresses in the soil, but that increase was negligible in modeling the stone columns. In addition, an optimal arrangement of stone columns with regard to the track axis under a typical train axle was examined by considering the dynamic amplification factor. The results showed there was no effect on vertical displacement. However, aligning the centers of stone columns with the track axis resulted in smaller horizontal displacement, compared with stone columns that were offset from the track axis.

This numerical analysis of a railway track supported by stone columns, under various train speeds, showed that both horizontal and vertical displacement were highly affected by the stone columns; even short columns were effective. However, an increase in train speed reduced the benefit of deeper stone columns in terms of controlling the horizontal displacement. The stone columns had no effect in reducing the peak vertical vibration amplitude at the high frequencies; however, the columns decreased the peak amplitude which resulted from two adjacent passenger cars' bogies. This effect was limited to train speeds lower than 180 km/h. Additionally, both short and long stone columns reduced the horizontal vibration amplitude at a point far from the loaded track.

A numerical simulation was used to evaluate the distributions of stress and strains within the soft soil, before and after improvement by stone columns. In this regard, ground with and without improvement, under various conditions (including train speed and stone column length) was studied. The results showed that an increase in speed had a more pronounced effect on shear stress than on vertical stress, leading to higher principal stress rotation angles. These higher angles are related to higher plastic deformation. In addition, volumetric response was not changed by train speed but volumetric response is strongly affected by introducing the stone columns to the model for the constant speed.

A comparison of stresses and strains calculated by the Mohr-Coulomb and Hardening Soil small-strain constitutive models showed that the simple elastic-perfectly plastic model was a suitable tool for predicting how stresses and strains are distributed in the soil. It showed fair accuracy for stone columns at a depth more than 2 m. However, it could not accurately predict the stress and strain – mainly shear stress and strain – close to the track.

The passage of a train, especially at high speed, develops the stress path in a way that reaches the critical state line (CSL). The results showed that application of stone columns, especially fully penetrated

columns, decreased the stress-path and caused a safe distance between the path and the CSL. Furthermore, deeper columns outperforming shorter ones as train speed increased.

Short stone columns are not embedded in a dense soil layer and do not behave as an end-bearing condition. Nonetheless, they are a good solution for controlling the settlement and displacement of a railway track constructed on weak soil conditions. Generally, soil and short stone columns behave as a unit that tends to move outwards to the shoulder of the track.

A combination of failure mechanisms was observed, with specific failure modes being highly influential. Separation was the predominant failure mode for short columns; bending occurred in end-bearing conditions; and regardless of stone column length, bulging in the middle stone column under the loading area was the main failure mode. Furthermore, low lateral restraint led to a diagonal shear plane. Typically, an overall failure mechanism results in the concentration of deformation along the shear plane, but unlike the short stone columns constructed under a foundation, a negligible punching has observed. Generally, stone column failure depended on their location corresponding to the load area, rather than train speed.

8 Further Research Topics

In this chapter possible topics for further research and general recommendations based on the results of this thesis are discussed.

Train-track interaction

In this work the interaction between the train and track was not considered. The effects of the dynamic loading caused by wheel and rail irregularity and a train's suspension system were ignored. Therefore, coupling a vehicle model and a track model would provide a solution for studying the effect of their interaction on the track's response, and its behavior after improvement.

Water content

It was shown that pore water pressure increased during the passage of a train. The benefit of stone columns in minimizing the increase of pore water pressure was studied. However, in the stress study, the presence of water was not considered and the simulations were done under saturated conditions of the soft soil layer. It is known that soil has in situ water content, which requires consideration of the unsaturated or partially saturated soil condition. Such an analysis could be conducted for deeper studies, particularly in combination with train-track interactions.

Increase the number of train passages

The numerical results in this thesis have shown that the first loading cycle, depending on depth has the greatest influence on the track and on material responses. However, it is essential to study the effects of stone columns in the longer term and under the passage of a higher number of either passenger or freight trains, travelling at different speeds.

Advanced and anisotropy constitutive models

The behavior of the track, especially after improvement, could be studied by considering more advanced material models. In this study, elastic-perfectly plastic and Hardening Soil small-strain models were used, which incorporate the stress-dependent stiffness and can demonstrate small strain nonlinear responses. The next step could be the application of constitutive models that consider the anisotropy of material. For instance, the Ecole Centrale Paris model or the Boyce anisotropic model are particularly suited for sandy material, and hypoplastic model with stiffness anisotropy for clay.

Three-dimensional calculation

A full 3D analysis can help to provide insight into the behavior of a track after improvement with stone columns. Specifically, 3D simulations give an opportunity to study different arrangement patterns in real life and not by equivalent strips. In this way more realistic conditions can be modeled and each pattern can be studied individually. Moreover, rapid development in new calculation methods, namely the boundary element method (BEM) and scaled boundary finite element method (SBFEM) could be good options for faster analysis of bigger models in a shorter time.

Geosynthetic and encasing of stone columns

The influence of geosynthetic reinforcement on railway tracks improved by stone columns can be investigated. Their benefits for the transfer and distribution of vertical load among stone columns can be evaluated. Geosynthetic encasement of stone columns is a typical approach to improve their performance in soft soil, as it provides higher confinement and prevents bulging and rapid shear failure. Therefore, the behavior of encased stone columns under the passage of different train speeds could be the next step after this study.

Bibliography

- ADAM, D., BRANDL, H. & PAULMICHL, I. 2010. Dynamic aspects of rail tracks for high-speed railways. *International Journal of Pavement Engineering*, 11, 281-291.
- ADAM, D. & KOPF, F. 2003. Dynamische Effekte durch bewegte Lasten auf Fahrwegen. *Bauingenieur*, 78, 1-12.
- ALEXIEW, D. & RAITHEL, M. 2015. Geotextile-Encased Columns: Case Studies over Twenty Years. *Ground Improvement Case-Histories: Embankments with Special Reference to Consolidation and Other Physical Methods*, Elsevier BV, Waltham, MA, USA, 451-477.
- ALVES COSTA, P., CALÇADA, R. & SILVA CARDOSO, A. 2012. Track-ground vibrations induced by railway traffic: In-situ measurements and validation of a 2.5D FEM-BEM model. *Soil Dynamics and Earthquake Engineering*, 32, 111-128.
- ALVES COSTA, P., CALÇADA, R., SILVA CARDOSO, A. & BODARE, A. 2010. Influence of soil non-linearity on the dynamic response of high-speed railway tracks. *Soil Dynamics and Earthquake Engineering*, 30, 221-235.
- ARAÚJO, N. M. F. 2011. *High-speed trains on ballasted railway track: dynamic stress field analysis*. Doctoral thesis, Universidade do Minho.
- AREMA, L. 2013. American railway engineering and maintenance-of-way association. *Manual for railway engineering*.
- BACHUS, R. C. & BARKSDALE, R. D. 1989. Design methodology for foundations on stone columns. *Foundation Engineering: Current Principles and Practices*, 1989 Georgia, USA: ASCE, 244-257.
- BALAAM, N. & BOOKER, J. R. 1981. Analysis of rigid rafts supported by granular piles. *International Journal for numerical and analytical methods in geomechanics*, 5, 379-403.
- BANIMAHD, M. & WOODWARD, P. K. 2007. Numerical study of train speed effect on railway track response. 9th International Conference on Railway Engineering, 2007 London: XiTRACK.
- BIAN, X., CHENG, C., JIANG, J., CHEN, R. & CHEN, Y. 2014. Numerical analysis of soil vibrations due to trains moving at critical speed. *Acta Geotechnica*, 1-14.
- BRANDL, H. 2004. Geotechnical aspects for high-speed railways. In: LOIZOS, G. C., ed. *International Seminar on Geotechnics in Pavement and Railway Design and Construction*, 2004 Rotterdam, Netherlands, 117-132.
- BURROW, M., GHATAORA, G. & BOWNESS, D. 2004. Analytical track substructure design. ISSMGE TC3 International Seminar on Geotechnics in Pavement and Railway Design and Construction, 2004, 209-216.
- CASTRO, J. 2017. Modeling Stone Columns. *Materials (Basel)*, 10, 782.
- CONNOLLY, D., GIANNOPOULOS, A. & FORDE, M. C. 2013. Numerical modelling of ground borne vibrations from high speed rail lines on embankments. *Soil Dynamics and Earthquake Engineering*, 46, 13-19.
- CONNOLLY, D. P. 2013. *Ground borne vibrations from high speed trains*. Doctor of Philosophy, The University of Edinburgh.
- CONNOLLY, D. P., KOUROUSSIS, G., GIANNOPOULOS, A., VERLINDEN, O., WOODWARD, P. K. & FORDE, M. C. 2014. Assessment of railway vibrations using an efficient scoping model. *Soil Dynamics and Earthquake Engineering*, 58, 37-47.
- COSTABEL, M. 1987. Principles of boundary element methods. *Computer Physics Reports*, 6, 243-274.
- CUNHA, J. P. F. D. 2013. *Modelling of ballasted railway tracks for high-speed trains*. Doctoral thesis, Universidade do Minho Escola de Engenharia.
- DAHLBERG, T. 2003. *Railway Track Dynamics - a survey*.
- DAHLBERG, T. 2004. Published. *Railway track settlements - a literature review*. Solid Mechanics, IKP, Linköping, Sweden, 42.
- DEGRANDE, G. & SCHILLEMANS, L. 2001. Free field vibrations during the passage of a high speed train: experimental results and numerical predictions. *Journal of Sound and vibration*, 274, 131-144.

- DULEY, A., LE PEN, L., THOMPSON, D., POWRIE, W., WATSON, G., PETER, M. & ANDREW, C. 2015 Published. Critical train speeds and associated track movements—a case study. XVI ECSMGE, 2015 of Conference Edinburg, United Kingdom.
- EKEVID, T. & WIBERG, N.-E. 2002. Wave propagation related to high-speed train: A scaled boundary FE-approach for unbounded domains. *Computer Methods in Applied Mechanics and Engineering*, 191, 3947-3964.
- ESTORFF, O. & PRABUCKI, M. J. 1990. Dynamic response in the time domain by coupled boundary and finite elements. *Computational Mechanics*, 6, 35-46.
- ESVELD, C. 2001. *Modern Railway Track*, Delft, Netherlands, Delft university of Technology.
- FERREIRA, J. N. V. D. S. 2013. *Long Term Behaviour of Railway Transition Under Dynamic Loading - Application to Soft Soil Sites*. Doctor of Philosophy, Universidade Nova De Lisboa.
- FILZ, G. M. & NAVIN, M. P. 2006 Published. Stability of column-supported embankments. Virginia Center for Transportation Innovation and Research, Charlottesville, Virginia TRANSPORTATION, V. D. O., 76.
- FRÝBA, L. 1999. *Vibration of solids and structures under moving loads*, Prague, Czech Republic, Thomas Telford, 206-230.
- GALAVI, V. & BRINGGREVE, R. 2015. Finite element modelling of geotechnical structures subjected to moving loads. *Analytical Methods in Petroleum Upstream Applications*, 235.
- GALVÍN, P. & DOMÍNGUEZ, J. 2009. Experimental and numerical analyses of vibrations induced by high-speed trains on the Córdoba–Málaga line. *Soil Dynamics and Earthquake Engineering*, 29, 641-657.
- GALVÍN, P., ROMERO, A. & DOMÍNGUEZ, J. 2010. Fully three-dimensional analysis of high-speed train–track–soil–structure dynamic interaction. *Journal of Sound and Vibration*, 329, 5147-5163.
- GOODMAN, R. E. 1976. *Methods of geological engineering in discontinuous rocks / Richard E. Goodman*, St. Paul, West Pub. Co.
- GOUGHNOUR, R. & BARKSDALE, R. 1984 Published. Performance of a stone column supported embankment. International Conference on Case Histories in Geotechnical Engineering, 1984 of Conference Missouri, United States: Missouri University of Science and Technology, 735-742.
- GUETIF, Z., BOUASSIDA, M. & DEBATS, J. 2007. Improved soft clay characteristics due to stone column installation. *Computers and Geotechnics*, 34, 104-111.
- HALL, L. 2000. *Simulations and Analyses of Train-induced Ground Vibrations: A Comparative Study of Two-and Three-dimensional Calculations with Actual Measurements*, Stockholm, Royal Institute of Technology, Division of Soil & Rock Mechanics, 196.
- HALL, L. 2002. Simulations and analyses of train-induced ground vibrations in finite element models. *Soil Dynamics and Earthquake Engineering*, 403-413.
- HEELIS, M., COLLOP, A., DAWSON, A., CHAPMAN, D. & KRYLOV, V. V. 1999. Predicting and measuring vertical track displacements on soft subgrades. 2nd Railway Engineering 99 Conference 1999 London: Engineering Technics Press.
- HENDRY, M. T., MARTIN, C. D. & BARBOUR, S. L. 2013. Measurement of cyclic response of railway embankments and underlying soft peat foundations to heavy axle loads. *Canadian Geotechnical Journal*, 50, 467-480.
- ISAAC, D. S. & GIRISH, M. 2009. Suitability of different materials for stone column construction. *EJGE*, 14, 2-12.
- JIANG, H., BIAN, X., CHENG, C., CHEN, Y. & CHEN, R. 2014. Simulating train moving loads in physical model testing of railway infrastructure and its numerical calibration. *Acta Geotechnica*, 1-12.
- KAEWUNRUEN, S. & REMENNIKOV, A. 2008. Dynamic properties of railway track and its components: a state-of-the-art review. *Weiss, BN (ed) New Research on Acoustics*, 197-220.
- KATZENBACH, R. & ITTERSHAGEN, M. 2004. Soil Improvement of Soft Soil under Dynamic and Static Loading-Case History of a Geotechnical Field Experiment under a Railway Line. Fifth International Conference on Case Histories in Geotechnical Engineering, 2004 New York: University of Missouri--Rolla, Paper No. 4.22 (1-5).

- KOUROUSSIS, G., CONNOLLY, D. P., FORDE, M. & VERLINDEN, O. 2013. Train speed calculation using ground vibrations. *Proceedings of the Institution of Mechanical Engineers, Part F: Journal of Rail and Rapid Transit*, 1-18.
- KOUROUSSIS, G., CONNOLLY, D. P. & VERLINDEN, O. 2014. Railway-induced ground vibrations – a review of vehicle effects. *International Journal of Rail Transportation*, 2, 69-110.
- KOUROUSSIS, G., VERLINDEN, O. & CONTI, C. 2009. Ground propagation of vibrations from railway vehicles using a finite/infinite-element model of the soil. *Proceedings of the Institution of Mechanical Engineers, Part F: Journal of Rail and Rapid Transit*, 223, 405-413.
- KOUROUSSIS, G., VERLINDEN, O. & CONTI, C. 2011. Free field vibrations caused by high-speed lines: Measurement and time domain simulation. *Soil Dynamics and Earthquake Engineering*, 31, 692-707.
- KRAMER, S. L. 1996. *Geotechnical Earthquake Engineering*, Prentice Hall.
- KRYLOV, V. V., DAWSON, A. R., HEELIS, M. E. & COLLOP, A. C. 2000. Rail movement and ground waves caused by high-speed trains approaching track-soil critical velocities. *Proceedings of the Institution of Mechanical Engineers, Part F: Journal of Rail and Rapid Transit*, 214, 107-116.
- LEUNG, K. L., BESKOS, D. E. & VARDOULAKIS, I. G. 1990. Vibration isolation using open or filled trenches. *Computational Mechanics*, 7, 137-148.
- LI, D., HYSLIP, J., SUSSMANN, T. & CHRISMER, S. 2002. *Railway geotechnics*, CRC Press.
- LOMBAERT, G., DEGRANDE, G., KOGUT, J. & FRANÇOIS, S. 2006. The experimental validation of a numerical model for the prediction of railway induced vibrations. *Journal of Sound and Vibration*, 297, 512-535.
- LU, M. & MCDOWELL, G. R. 2007. The importance of modelling ballast particle shape in the discrete element method. *Granular Matter*, 9, 69-80.
- LYSMER, J. & KUHLEMEYER, R. L. 1969. Finite Dynamic Model for Infinite Media. *Journal of Engineering Mechanics Division*, 95, 859-878.
- MADSHUS, C. & KAYNIA, A. M. 2000. High-Speed Railway Lines on Soft Ground: Dynamic Behaviour at Critical Train Speed. *Journal of Sound and Vibration*, 231, 689-701.
- MCELVANEY, J., SNAITH, M. & O'FLAHERTY, C. 2002. Analytical design of flexible pavements. *Highways the location design construction and maintenance of pavements. Oxford: Butterworth-Heine-mann*, 395-423.
- MIURA, S., TAKAI, H., UCHIDA, M. & FUKADA, Y. 1998. The mechanism of railway tracks. *Japan Railway & Transport Review*, 3, 38-45.
- MUNDREY, J. 2009. *Railway track engineering*, Tata McGraw-Hill Education.
- NG, K. S. & TAN, S. A. 2014. Nonlinear Behaviour of an Embankment on Floating Stone Columns. *Geomechanics and Geoengineering*, 10, 30-44.
- O'BRIEN, J. & RIZOS, D. C. 2005. A 3D BEM-FEM methodology for simulation of high speed train induced vibrations. *Soil Dynamics and Earthquake Engineering*, 25, 289-301.
- PAOLUCCI, R., MAFFEIS, A., SCANDELLA, L., STUPAZZINI, M. & VANINI, M. 2003. Numerical prediction of low-frequency ground vibrations induced by high-speed trains at Ledsgaard, Sweden. *Soil Dynamics and Earthquake Engineering*, 23, 425-433.
- PICOUX, B. & LE HOUÉDEC, D. 2005. Diagnosis and prediction of vibration from railway trains. *Soil Dynamics and Earthquake Engineering*, 25, 905-921.
- PLAXIS BV 2014. *PLAXIS 2D - Reference*, Netherlands, PLAXIS.
- POOROOSHASB, H. & MEYERHOF, G. 1997. Analysis of behavior of stone columns and lime columns. *Computers and Geotechnics*, 20, 47-70.
- PRIEBE, H. J. 1995. The design of vibro replacement. *Ground engineering*, 28, 31-47.
- RAJU, V., WEGNER, R. & KRISHNA, Y. H. 2004. Published. Ground improvement using vibro replacement in asia 1994 to 2004. 5th International Conference on GROUND IMPROVEMENT TECHNIQUES, 2004 of Conference Kuala Lumpur, Malaysia: Keller, Kuala Lumpur, 1-31.
- SADEGHI, J. & BARATI, P. 2010. Evaluation of conventional methods in Analysis and Design of Railway Track System. *International Journal of Civil Engineering*, 8, 44-56.
- SAYEED, M. A. & SHAHIN, M. A. 2016. Three-dimensional numerical modelling of ballasted railway track foundations for high-speed trains with special reference to critical speed. *Transportation Geotechnics*, 6, 55-65.

- SELIG, E. T. & BOUCHER, D. L. 1990. Abrasion tests for railroad ballast. *ASTM geotechnical testing journal*, 13, 301-311.
- SELIG, E. T. & WATERS, J. M. 1994. *Track geotechnology and substructure management*, Thomas Telford.
- SHAHRAKI, M., SADAGHIANI, M. R. S., WITT, K. J. & MEIER, T. 2014a. 3D Modelling of Train Induced Moving Loads on an Embankment. *Plaxis Bulletin*, 10-16.
- SHAHRAKI, M., SADAGHIANI, M. R. S., WITT, K. J. & MEIER, T. 2014b. Model Quality Investigations of Induced Moving Loads of High-Speed Trains. Numerical Methods in Geotechnical Engineering - Proceedings of the 8th European Conference on Numerical Methods in Geotechnical Engineering, NUMGE 2014, 2014b, 1169-1173.
- SHENG, X., JONES, C. J. C. & THOMPSON, D. J. 2003. A comparison of a theoretical model for quasi-statically and dynamically induced environmental vibration from trains with measurements. *Journal of Sound and Vibration*, 267, 621-635.
- SHENG, X., JONES, C. J. C. & THOMPSON, D. J. 2006. Prediction of ground vibration from trains using the wavenumber finite and boundary element methods. *Journal of Sound and Vibration*, 293, 575-586.
- SHIH, J.-Y., THOMPSON, D. J. & ZERVOS, A. 2016 Published. Modelling of ground-borne vibration when the train speed approaches the critical speed. 12th International Workshop on Railway Noise, IWRN12, 2016 of Conference Terrigal, Australia: Springer, 497-508.
- SKOGLUND, K. A. 2002. *A Study of Some Factors in Mechanistic Railway Track Design*. Doctor of Engineering, Norwegian University of Science and Technology.
- SONG, C. & WOLF, J. P. 2000. The scaled boundary finite-element method—a primer: solution procedures. *Computers & Structures*, 78, 211-225.
- TAN, S. A., TIAHYONO, S. & OO, K. 2008. Simplified Plane-Strain Modeling of Stone-Column Reinforced Ground. *Journal of Geotechnical and Geoenvironmental Engineering*, 134, 185-194.
- TSAI, P. & CHANG, T. 2009. Effects of open trench siding on vibration-screening effectiveness using the two-dimensional boundary element method. *Soil Dynamics and Earthquake Engineering*, 29, 865-873.
- VOGEL, W., LIEBERENZ, K., NEIDHART, T. & WEGENER, D. 2011. Zur dynamischen Stabilität von Eisenbahnstrecken mit Schotteroberbau auf Weichschichten. *Eisenbahntechnische Rundschau (ETR)*, 46-54.
- WEGENER, D. 2012. *Ermittlung bleibender Bodenverformungen infolge dynamischer Belastung mittels numerischer Verfahren*. PhD, Technische Universität Dresden.
- WHITE, W., LEE, I. K. & VALLIAPPAN, S. 1977. Unified boundary for finite dynamic models. *Journal of the Engineering Mechanics Division*, 103, 949-964.
- WITT, S. 2008. *The Influence of Under Sleeper Pads on Railway Track Dynamics*. Linköping University.
- WOLF, J. P. 1994. *Foundation vibration analysis using simple physical models*, Englewood Cliffs, NJ, PTR Prentice Hall.
- WOLF, J. P. & DEEKS, A. J. 2004. *Foundation vibration analysis : a strength-of-materials approach*, Amsterdam ; Boston, Elsevier.
- YANG, Y.-B. & HUNG, H.-H. 2001. A 2.5D finite/infinite element approach for modelling visco-elastic bodies subjected to moving loads. *International Journal for Numerical Methods in Engineering*, 51, 1317-1336.
- YANG, Y. B., HUNG, H. H. & CHANG, D. W. 2003. Train-induced wave propagation in layered soils using finite/infinite element simulation. *Soil Dynamics and Earthquake Engineering*, 23, 263-278.
- ZHAO, D., NEZAMI, E. G., HASHASH, Y. M. A. & GHABOUSSI, J. 2006. Three-dimensional discrete element simulation for granular materials. *Engineering Computations*, 23, 749-770.